Monitoring dynamics of semi-arid forests with multi-sensor time series

vorgelegt von
Master of Science
Philipp Gärtner
geb. in Nordhausen

Von der Fakultät VI - Planen - Bauen - Umwelt der
technischen Universität Berlin
zur Erlangung des akademischen Grades

Doktor der Naturwissenschaften
- Dr. rer. nat. -

genehmigte Dissertation

Abstract

Dryland degradation is a challenging environmental problem in the context of global change and China is among those countries that are most severely affected. The far-west province of Xinjiang Uyghur Autonomous Region experienced ambitious agricultural development and land reclamation projects which caused major environmental degradation, loss of forest cover and the advancement of desertification. Efforts from the Chinese government to restore the degraded floodplain ecosystem are ongoing. This dissertation aimed to enhance the monitoring of forest dynamics in the floodplains of the Tarim river in Southern Xinjiang, by examining the suitability of multi-sensor time series to assess forest disturbance and restoration response. The main focus was on the applicability of very high, high and medium spatial resolution satellite imagery to improve forest disturbance and forest re-growth monitoring.

First, I studied the growth and decline of individual tree crowns with bi-temporal change detection of very high spatial resolution satellite images (Chapter 2). Second, I investigated the dynamics of forest disturbance caused by an insect pest outbreak. It was examined whether forest disturbance maps produced with additional synthetic high resolution images would improve the accuracy of disturbance detection (Chapter 3). Finally, I used a medium spatial resolution Landsat time series to monitor trend shift dynamics of the floodplains forest, shrubland and grassland areas. A special focus lay on the spatial pattern of longitudinal and transverse linkages to known river discharges (Chapter 4).

Results showed predominantly positive growth at all investigated spatial

scales. At local scale, findings confirmed increased *P. euphratica* tree crown growth. The applied OBIA approach proved to be useful in the semi-arid forest setting, producing moderate accuracies. Forest disturbance mapping, with added synthetic scenes, improved significantly when compared to the original data set. The most important factor for the accuracy increase was the timing, rather than the number of images involved in the analysis. Images which were recorded at the end of the insect disturbance period performed best during the disturbance detection. This stage was found particularly important in distinguishing defined defoliation severity classes. Finally, the trend shift analysis showed increased rates of forest, shrub- and grassland growth in times when water deliveries were conducted. The absent of discharge had a substantial interrupting effect on the prevalence of trend shifts. Vegetation showed resilience after a drought year, with above average growth in subsequent years. Longitudinal effects, with more pronounced vegetation reactions, was found in the upper zones and less apparent reactions in the lower sections of the river catchment area. Transverse impacts showed a delayed growth response of ∼six month in areas adjacent to the river channel.

This dissertation demonstrates the value of multi-sensor time series analysis for monitoring forest dynamics. The expressed findings increase knowledge and enhance understanding towards disturbance effects and response dynamics in semi-arid forest ecosystems, and shall help to improve future management decisions.

Zusammenfassung

Die Degradation der Trockengebiete ist ein großes Umweltproblem speziell im Zusammenhang mit dem globalen Klimawandel. China ist eines der Länder das am stärksten betroffen ist. Besonders die westlichste Provinz im Uigurisch Autonomen Gebiet Xinjiang erfuhr eine ehrgeizige Landgewinnung vornehmlich für Landwirtschaft. Diese Entwicklung hat große Umweltzerstörungen wie zum Beispiel den Verlust von Waldflächen und die Wüstenbildung verursacht. Die chinesische Regierung hat diese Entwicklung erkannt und ist um die Sanierung der degradierten Auenökosysteme bemüht. Das Ziel der vorliegenden Dissertation ist das Monitoring der Auwalddynamiken entlang des Tarim Flusses in Süd-Xinjiang zu verbessern. Dabei soll die Zweckmäßigkeit von multisensoralen Zeitreihen bewertet werden. Außerdem soll die Anwendbarkeit verschiedener (sehr hoch, hoch und mittlerer) räumlicher Auflösungen von Satellitenbildern für die Erfassung und Überwachung von Waldschäden sowie die Reaktion auf die Sanierung bewertet werden.

Zuerst wurde das Wachstum bzw. die Reduzierung einzelner Baumkronendurchmesser anhand einer bi-temporalen Veränderungsdetektion mit sehr hoch aufgelösten Satellitenbildern bestimmt (Kapitel 2). Danach wurden die Dynamiken von Waldstörungen, verursacht durch Insektenfraß, untersucht. Dabei wurde geprüft ob sich die Genauigkeit bei der Erfassung von Waldschäden mit zusätzlichen, synthetisch erzeugten, Bildern erhöht (Kapitel 3). Abschließend wurde eine Landsat Zeitreihe mit mittlerer räumlicher Auflösung genutzt um plötzliche Veränderungen im Hinblick auf die Entwicklungsdynamiken von verschiedenen Landbedeckungsklassen (Wald, Busch-

land und Grassland) zu erkennen. Ein besonderer Schwerpunkt lag auf der
Erkennung räumlicher Muster entlang bzw. quer zum Fluß in Verbindung
mit ökologischen Wassergaben (Kapitel 4).

Die Ergebnisse zeigten überwiegend positives Wachstum bei allen unter-
suchten räumlichen Skalen. Auf lokaler Ebene bestätigten sich Erkennt-
nisse vom Zuwachs der *P. euphratica* Baumkronen. Die objektbasierte Bil-
danalyse erwies sich im semi-ariden Milieu als nützlich und hat moderate
Genauigkeiten geliefert. Verglichen mit dem ursprünglichen Datensatz, hat
sich die Erkennung von Waldschäden mit der Nutzung von synthetischen
Szenen deutlich verbessert. Der wichtigste Faktor für die Verbesserung der
Genauigkeiten war der Zeitpunkt der Aufnahme und nicht die Anzahl der
Bilder die in die Analyse einbezogen wurden. Dabei waren Bilder die am
Ende der Fraßperiode erfasst wurden am wichtigsten für die Erkennung der
Waldschäden. Diese Phase war auch bei der Unterscheidung von Schaden-
sklassen wichtig. Die Untersuchung der Entwicklungsdynamiken der Auen-
vegetation hat erhöhtes Wachstum nach ökologischen Wassergaben gezeigt.
Bei fehlenden Wassergaben gab es eine Unterbrechung bei den Trend-
veränderungen. Nach einem Trockenjahr zeigte die Vegetation Resilienz mit
überdurchschnittlichem Wachstum in den Folgejahren. Ausgeprägte Trend-
veränderungen der Vegetation wurden entlang des Flußes, speziell in den
nördlichen Zonen und weniger in südlichen Flussabschnitten, gefunden.
Verzögerte Wachstumseffekte von sechs Monaten gab es in unmittelbarer
Umgebung zum Fluß.

Die vorliegende Arbeit zeigt den Wert der Multi-Sensor-Zeitreihenanalyse
für die Überwachung von Walddynamiken. Die gezeigten Ergebnisse ver-
bessern das Verständnis gegenüber Störeffekten und Reaktionsdynamiken
in semi-ariden Waldökosystemen. Die Ergebnisse tragen dazu bei künftig
verbesserte Managemententscheidungen zu treffen.

Contents

List of Figures

Chapter 4

Chapter A

List of Tables

List of Abbreviations

μ	Population mean
CART	Classification And Regression Tree
CSR	Competitors - Stress Tolerators - Ruderals
DBH	Diameter at Breast Height
DOY	Day Of Year
ESTARFM	Enhanced Spatial Temporal Adaptive Reflectance Fusion Model
ETM+	Enhanced Thematic Mapper Plus
EWCP	Ecological Water Conveyance Project
FDX	Forestry Department of Xinjiang
HCS	Hyperspherical Colour Sharpening
IR-MAD	Iteratively Reweighted Multivariate Alteration Detection
L8	Landsat 8
LEDAPS	Landsat Ecosystem Disturbance Adaptive Processing System
LiDAR	Light Detection And Ranging
LM	Local Maximum
mESTARFM	Modified ESTARM
MODIS	Moderate Resolution Imaging Spectrometer
NDVI	Normalized Difference Vegetation Index
NDVI	Normalized Difference Vegetation Index
NDWI	Normalized Difference Water Index
NIR	Near-Infrared
NRMSE	Normalized Root Mean Square Error

OA	Overall Accuracy
OBIA	Object Based Image Analysis
OLI	Operational Land Imager
PA	Producer Accuracy
QB	QuickBird
r	Pearson Correlation Coefficient
RE	RapidEye
RF	Random Forest
RMSE	Root Mean Square Error
SAVI	Soil-Adjusted Vegetation Index
SINDVI	Seasonally Integrated NDVI
SNR	Signal To Noise Ratio
SRI	Simple Ratio Index
STAARCH	Spatial Temporal Adaptive Algorithm for mapping Reflectance Change
STARFM	Spatial Temporal Adaptive Reflectance Fusion Model
STL	Seasonal-Trend Decomposition using Loess
SVM	Support Vector Machine
TBWRC	Tarim Basin Water Resources Commission
TM	Thematic Mapper
ToA	Top of Atmosphere
UA	User Accuracy
USGS	U.S. Geological Survey
VHSR	Very High Spatial Resolution
WRS	World-wide Reference System
WV2	WorldView-2

Chapter 1
Introduction

1.1 Monitoring forest disturbance and recovery dynamics

Forest dynamics describe the underlying physical and biological forces that form a forest over time and characterize the continuous state of change that alters its composition and structure (Ashton et al., 2012). Forest ecosystems are always influenced by both the current environment and legacies of previous environmental fluctuations and disturbances (Chapin et al., 2011). A disturbance is understood as a relative discrete event in time (Brokaw et al., 1985), that shape forest systems by affecting their composition, structure, and functional processes (Dale et al., 2001). Disturbances include both natural and human induced processes. Natural processes can be biotic such as insect or herbivore agents or abiotic like drought, hurricane or volcanic eruptions. However, human activities have altered the frequency and size of many natural disturbances and have produced new types of disturbances such as large scale logging or open-pit mining (Chapin et al., 2011). In contrast to a one off disturbance event, refers the disturbance regime to the spatial and temporal dynamics of disturbances over a longer time period (Turner, 2010). Naturally occurring disturbances play an important integral part in the lifecycle and succession dynamics of many forest system, and shall be considered as normal property of ecosystems (Chapin et al., 2011).

 After disturbance follow recovery and renewal. Resilience to disturbance shows the capacity of an forest ecosystem to sustain its fundamental function and structure after perturbations (Chapin et al., 2011), and adapt or adjust to stress (Dobbertin, 2005; Kozlowski and Pallardy, 2002). Hence, fostering resilience in forest ecosystems should be the key target of sustainable development of forest resources (Yan et al., 2011).

1.1.1 Importance of dryland forests

Forests, defined by Food et al. (2006) as *"land spanning more than 0.5 hectares with trees higher than 5 meters and a canopy cover of more than 10 percent ... "*, cover 31% of the world's land surface (FAO, 2015). Many areas in arid lands, including semi-arid and dry sub-humid lands, have sparse tree populations such as trees outside of forest, also defined as "other wooded

land", where *"tree canopy is between 5 and 10%"*. Trees outside forests play a major role in arid lands particularly where agroforestry systems are abundant (Lam et al., 2011). Arid land forests and wooded lands count for 6% of the world's forest area (Malagnoux, 2007). The amount is equivalent to approx. 230 million hectare. Semi-arid forests provide key ecosystem services. They play a vital role in rural livelihood activities, regulate local and regional climate (Assessment, 2003), and increase carbon sequestration (Grünzweig et al., 2003). Semi-arid ecosystems dominate the recent positive global CO_2 sink trend (Ahlström et al., 2015) due to an increase in woody vegetation (Andela et al., 2013) especially in the Sahel region (Fensholt et al., 2012) and in Australia (Metcalfe, 2014). Although mainly driven by rainfall, the increase in tree cover might be supported by increasing levels of atmospheric CO_2 concentrations (Brandt et al., 2015), which are expected to lead to a CO_2 fertilization effect (Donohue et al., 2013).

Semi-arid forest ecosystems are regularly exposed to different types of disturbances, high among them are wild fires (Barbero et al., 1990; Williams et al., 2010) and drought (Guardiola-Claramonte et al., 2011; Liang et al., 2003). Even though semi-arid forests are well adapted to these natural disturbance regimes (Perry et al., 2008) superimposed climate change effects may increase their severity and frequency (Dale et al., 2001) with the consequence that affected forests fall below their resistance threshold (Dobbertin, 2005) and a regime shift becomes increasingly likely (Elmqvist et al., 2003).

In order to gain knowledge and improve understanding towards disturbance effects and response dynamics in semi-arid forest ecosystems, forest monitoring is essential. Such knowledge gain requires information on forest status with high spatial, temporal and thematic detail (DeVries et al., 2016). In this regard, remote sensing offers several desirable characteristics including large footprint sizes and regular data collection cycles (Chubey et al., 2006). Especially in isolated arid environments where vegetation cover is usually sparse and scattered is the usage of satellite imaging technology meaningful. In this context, China is a prime example to monitor forest dynamics with satellite imagery time series, especially in remote western China, where semi-arid forest areas are disturbed by recurring drought events and prolonged water deficits.

1.2 Remote sensing based forest monitoring

The first known remote sensing based forest monitoring was recorded in the *Berliner Tageblatt* of September 10, 1887 (Spurr et al., 1960, as cited in Franklin, 2001). The article reported about an attempt of an anonymous German forester who mapped a forest based on photos obtained from a hot-air balloon. The methods and technologies of remote sensing, including airborne and spaceborne sensors, have shown tremendous advancements since then (Franklin, 2001). At present there is a variety of satellite constellations monitoring the earth's surface. Each satellite, or rather sensor, is built with a particular intended target in mind. Be it for atmospherical, gravity & magnetism, snow & ice or land science. When designing the sensor, it has to be decided, what specific characteristics the sensor is supposed to have in terms of its spatial, radiometric, temporal and spectral resolutions. Spatial resolution refers to the size of the ground element represented by an individual pixel (Jones and Vaughan, 2010). The radiometric resolution is the number of distinct grey levels which are measured between pure black and pure white (e.g. 256 for 8-bit) (Gibson et al., 2013). The temporal resolution is the time between successive images and the spectral resolution refers to the dimension and number of specific wavelength intervals in the electromagnetic spectrum to which a sensor is sensitive (Al-Wassai and Kalyankar, 2013). Because of physical limitations in data storage and processor speed (Lefsky and Cohen, 2003) there is no sensor with *high* resolutions in *all* domains. There is a resolution trade—off e.g. a high spatial resolution is associated with a low spectral resolution and vice versa. This would mean a satellite system with a high spectral resolution can only offer a medium or low spatial resolution (Kalkhan, 2011). However the resolution dilemma is the main reason why there are hundreds of different satellite missions[1] and all have their valid justification.

In this dissertation, six optical sensors were used with very high (2), high (1) and medium spatial resolutions (3) (see Figure 1.1). The level of detail in very high spatial resolution sensors, such as WorldView-2, is often appreciated for object detection such as tree crown mapping (e.g. Karlson et al., 2014; Gomes and Maillard, 2013). However, the narrow multispectral bands provide also great potential for robust extraction of forest structural param-

---

[1] Satellite Missions Database

eters (Ozdemir and Karnieli, 2011), improved forest biomass and carbon estimations (Eckert, 2012), and to discriminate forest tree species (Peerbhay et al., 2014).
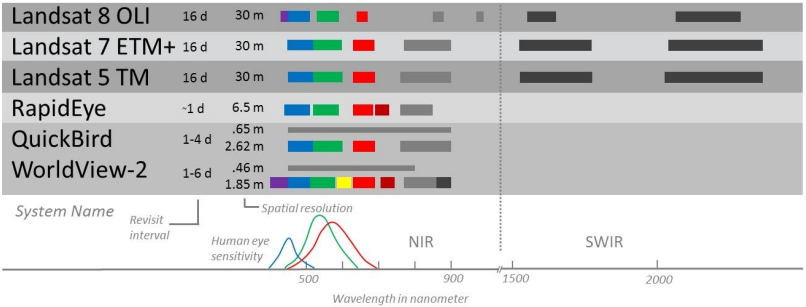
Fig. 1.1: The multispectral satellite systems used in the dissertation.

For the identification of plant nutrition and health status, the red-edge band has been recognized as important (e.g. Banninger, 1990; Curran et al., 1990, 1991). Plant pigments strongly absorb light in the red portion of the electromagnetic spectrum, the reflectance of leaves or needles is therefore low in red bands. On the other hand, mostly as a results of multiple scattering in the mesophyll, the reflectance of vegetation in the near-infrared region of the spectrum is very strong (Sahu, 2007). In a typical spectral response of green vegetation, the red-edge band (see Fig. 1.1, the dark red coloured band located between red and near-infrared) covers the portion of the spectrum where reflectance drastically increases from the red portion towards the near-infrared plateau (Weichelt et al., 2012). The RapidEye system, conceived to serve the agricultural and forestry markets (Weichelt et al., 2012), was the first high resolution, multi-spectral satellite system to include the red-edge band. The sensors additional red-edge information proved already useful for the monitoring of forest disturbance (Eitel et al., 2011; Marx, 2010).

At the level of the medium resolution, could Landsat already provide important insights for forest monitoring. Recent foci were on forest cover trends (Lehmann et al., 2013), forest disturbance and recovery (Kennedy et al.,

2010; Cohen et al., 2010; Frazier et al., 2015), and forest biomass dynamics (Powell et al., 2010; Pflugmacher et al., 2014; Gómez et al., 2014). Another increased research topic was the fusion of Landsat with other coarse sensors, mainly MODIS, to analyse forest phenelogy (Walker et al., 2012), forest cover change (Hansen et al., 2008), improve forest disturbance mapping (Hilker et al., 2009a) and push the time scale towards near real-time monitoring (Xin et al., 2013).

A prominent modern example of near real time forest monitoring gives the recently developed Global Forest Watch (World Resources Institute, 2016) online platform. This application offers worldwide forest loss and gains estimates between 2000-2014, at a spatial resolution of 30 meters (Hansen et al., 2013). The incorporated alert system provides locals with necessary information to better manage and conserve forest landscapes. While, Tropek et al. (2014) raised the issue on the inclusion of tree cover vegetation that is shorter than 5 m (e.g., pineapple, soybeans, or tea plantations) in contrast to the given definition of forest, the application also excludes scattered trees or tree-stands larger then 5 m and above the required minimum canopy density (> 10%). For example, the Tugay forest along the lower reaches of the Tarim river is unfortunately not included in the application, despite frequently occuring tree-stands beyond 5 m (Conradie et al., 2007; Thomas et al., 2016; Westermann et al., 2008; Aishan et al., 2016).

Scale is a real issue in forest research. Forest dynamics involve multiple processes at different levels so we must decide on the best scale to use in order to study certain features or phenomena. This requires often multiscale observation to overcome the resolution dilemma. For example, very high resolution data provide a great level of spatial detail and can be used to identify individual trees and track their growth changes over time. While the level of detail has many positive aspects for fine scale application it might be troublesome and ineffective for regional studies. Consequently, the study of forest dynamics in dryland forest requires multiscale observations where medium-resolution satellite data provide frequent regional overviews and very high and high-resolution satellite data to zoom into specific areas of interest in multi-year intervals in order to validate, more accurately interpret and, if necessary, recalibrate the medium-resolution data (Leprieur et al., 2000; Jones and Vaughan, 2010).

1.3 The Tugay forest along the Tarim river

The Tarim basin is an endorheic basin in northwest China occupying an area of about 1 million km^2 (Chen et al., 2006a). The basin, mostly covered by the Taklamakan desert, is surrounded by the Kunlun, Tian Shan and Pamir mountains (Zerbe and Thevs, 2011). The long distance to the nearest ocean cuts the region off from the effects of the Asian monsoon, hence rainfall is in general rare and low, resulting in a arid climate (Zhang et al., 2005).

The basin got its name from the Tarim river (chinesisch: *Talimu He*) which is fed by melting water and precipitation in the mountains through its three tributaries Aksu, Hotan, and Yarkant (Thevs, 2005). The Tarim river flows along the edge of the Taklamakan desert and reaches after 1,321 km the Tetema end lake (see Figure 1.3). The river is the lifeline for the entire region, providing water for urban life, oasis agriculture, and the natural ecosystems in the floodplains (Rumbaur et al., 2015).

Tugay[2] vegetation is the most dominant vegetation distributed along floodplains of the Tarim river. It is composed from forests, e.g. Tugay forests, dominated by *Populus euphratica*, *Tamarix* bush communities and reeds (Thevs, 2005). The Tugay vegetation provides an important habitat for plant and animal life, and harbors the highest biodiversity in the region (Thevs, 2005). In addition, it constitutes major natural resources (e.g. wood) for local communities and serves as grazing ground for livestock (Säumel et al., 2011). Furthermore, it supplies a wide range of ecosystem services such as landscape preservation, wind protection, and stabilization of moving sand, soil, and riverbanks (Eusemann et al., 2013). These services contribute enormously to prevent further desertification (Wang et al., 2012), especially in the lower reaches of the Tarim river where the Tugay forest acts as *green corridor*, slowing or even preventing the Taklamakan and Kuruk Tagh deserts from merging.

However, significant river regulations and land reclamations have taken place over the last decades due to increasing population pressure and intensified agricultural activities (Liu and Chen, 2006; Zhao et al., 2013). These

---

[2] Tugay vegetation comes from the Uyghur word *Tugay* (synonym with *Tugai*), which refers to vegetation along rivers in arid areas in Central Asia (Thevs, 2005).

Fig. 1.2 Tugay forest in the lower reaches of the Tarim river. Clusters of *Populus euphratica* trees stand close to the river where groundwater levels are low.

regulations have a profound effect on the environment. By way of example, the construction of the Daxihaizi reservoir in 1973, located at the end of the middle reaches of the Tarim river, disrupted the stream flow to the lower reaches for 20 years (Lyle and Gaofeng, 2011). As a result, groundwater levels dropped and salinization increased. Consequently, the natural floodplain vegetation degraded and Tugay forests declined by 70% (Fan, 1996).

The intensification of wind erosion severely threatened the provision of the *green corridor* ecosystem service along the lower reaches of the Tarim river (Halik et al., 2006; Betz et al., 2015). Facing the threat of a serious environmental disaster, the Chinese government declared the conservation of Tugay vegetation along the Tarim river as one key project in their implementation of the UN Convention to Combat Desertification (CCICCD, 1996).

In 2000, the Chinese government implemented the *Integrated Environmental Management of the Tarim Basin* project in order to secure the regions ecological, economical and social sustainability (Lyle and Gaofeng, 2011). An important sub-project is the *Ecological Water Conveyance Project* (EWCP) which includes i) regular water diversions from the Daxihaizi reservoir towards the lower reaches of the river to mimic the natural flood regime, and ii) hydrological engineering measures such as enbankment constructions, the installation of weirs or the shortenings of meanders (Zheng et al., 2004; Zhu et al., 2006; Halik et al., 2006). These measures shall contribute to recharge groundwater tables up to a level where natural floodplain vegetation can revitalize, and create condition under which generative regenerations are possible.

1.4 Problem statement

Numerous studies provided evidence of the effect of recharged groundwater on Tugay vegetations growth and revival at the lower reaches of the Tarim river (e.g. Thomas et al., 2016; Westermann et al., 2008; Aishan et al., 2015; Li et al., 2013b; Ling et al., 2015). While most studies highlight response effects at individual sites under specific conditions, the spatial pattern of Tugay vegetation response rates remain largely unknown. In addition, the consequences of hydrological engineering measures on Tugay vegetation rehabilitation lack also understanding. Hence, monitoring the vegetation dynamics may provide deeper insights into the Tugay growth and decline processes and may further improve forthcoming decision making on rehabilitation measures.

As described above, there is a growing number of research on the effect of the EWCP on groundwater dynamics and riparian vegetation. However, large scale forest disturbances such as recurring insect pest outbreaks are completely overlooked. For example, the annual defoliation of about 80-90% of the *P. euphratica* trees caused by the defoliator moth *A. cinerarius* has not yet been investigated, neither is the additional effect on tree degradation (Conradie et al., 2007). There is a need to better understand the dynamics of forest disturbance and provide information on the temporal and spatial dimension of such defoliation and its severity. The level of analysis is connected to the availability of multi-sensor satellite imagery and the scale of field validation data, and shall ideally range from local (e.g. individual trees) to regional levels (e.g. lower reaches river network).

1.5 Objectives and research questions

The research described in this dissertation aims to enhance the monitoring of forest dynamics in the lower reaches of the Tarim river by examining the suitability of multi-sensor time series to assess forest disturbance and response. The main focus is on the applicability of very high, high and medium spatial resolution satellite imagery to improve forest disturbance and forest regrowth monitoring.

The setting of the lower reaches of the Tarim river provides a rare research opportunity, where external factors are low (e.g. precipitation), river discharge is controlled (via EWCP) and the isolated location reduces human influences to a bare minimum. Here, I conducted my study at two research sites. The first research site is around the Arghan forest monitoring station where the old Tarim river and the Chiwinkol river branch merge (see *Alagan* in Figure 1.3). The local Tugay forest revitalized after the implementation of the EWCP, hence I expressed the following two research questions:

Research Question 1 — **Can we observe individual tree crown changes with very high spatial resolution satellite imagery in semi-arid forests? (Chapter 2)**

I answer this question with a bi-temporal change detection analysis of two very high spatial resolution satellite images. I compare field measured crown changes with OBIA derived crown diameters and assess tree crown growth and decline between the years of 2005 and 2011 at a local scale. Finally, I provide an accuracy assessment for the chosen approach.

Research Question 2 — **Can a multi-sensor data fusion time-series improve forest disturbance detection in semi-arid forests and which factors are most important? (Chapter 3)**

This question is directly linked to the second *problem statement* (see Section 1.4). Annual defoliation causes forest disturbances with complex spatial dynamics. In order to monitor affected areas, decision makers seek but often lack information with high spatial and temporal precision. This study examines whether the analysis of a RapidEye time series would benefit from the availability of synthetically generated images at the spatial resolution of RapidEye and the additional temporal resolution of Landsat 8. I applied a sensor fusion model to downscale Landsat 8 scenes to concurrent RapidEye scenes. I performed a pixel-based regression analyses in order to evaluate the quality of the synthetically created image products. Furthermore, I examined if forest disturbance maps produced with synthetic images improve the accuracy of disturbance detection.

The second research site covers the entire lower reaches of the Tarim river from the Daxihaizi reservoir until the Tetema end lake. Here I focus on the trend shifts of Tugay forest, shrubland and grassland and answer the third and last research question.

> *Research Question 3 —* **What were the rates and spatial patterns of Tugay vegetation trend shifts in the lower reaches of the Tarim river since 2000? (Chapter 4)**
>
> The ecological restoration of degraded riparian Tugay forests in the lower reaches is critical in order to keep the *green corridor* intact and combat desertification in this region. I answer the third research question by means of a medium resolution time series (Landsat) of 14 years. I search the time series for abrupt changes in long term vegetation trends which can be generally described as trend shifts. I analyse similarities and differences between several Tugay vegetation types in their response effects, and examine spatial patterns of longitudinal and transverse linkages to known river discharge.

1.6 Dissertation outline

This dissertation consists of five chapters. This introduction is followed by three core research chapters (Chapters 2-4) that have been described in the previous section. Chapter 5 provides a synthesis of the entire thesis, summarizing the main outcomes of the individual research chapters and provides answers to the research questions asked. Finally the main conclusions are drawn.

The core research chapters (Chapters 2 - 4) are based on a series of three stand-alone papers that have been published in, or submitted to internationally peer reviewed ISI ranked journals:

Chapter 2   **Gärtner, P.**, Förster, M., Kurban, A., & Klein-
schmit, B. (2014). Object based change detec-
tion of Central Asian Tugai vegetation with
very high spatial resolution satellite imagery. *In-
ternational Journal of Applied Earth Observa-
tion and Geoinformation*, vol 31, pages 110-121,
DOI:10.1016/j.jag.2014.03.004

Chapter 3   **Gärtner, P.**, Förster, M., & Kleinschmit, B.
(2016). The benefit of synthetically generated
RapidEye and Landsat 8 data fusion time series
for riparian forest disturbance monitoring. *Remote
Sensing of Environment*, vol 177, pages 237-247,
DOI:10.1016/j.rse.2016.01.028

Chapter 4   **Gärtner, P.**, Förster, M., & Kleinschmit, B.
(2016). Revealing trend shift dynamics after eco-
logical water deliveries using Landsat TM/ETM+
time series in a semi-arid forest ecosystem. *Under
Review: Remote Sensing of Environment*
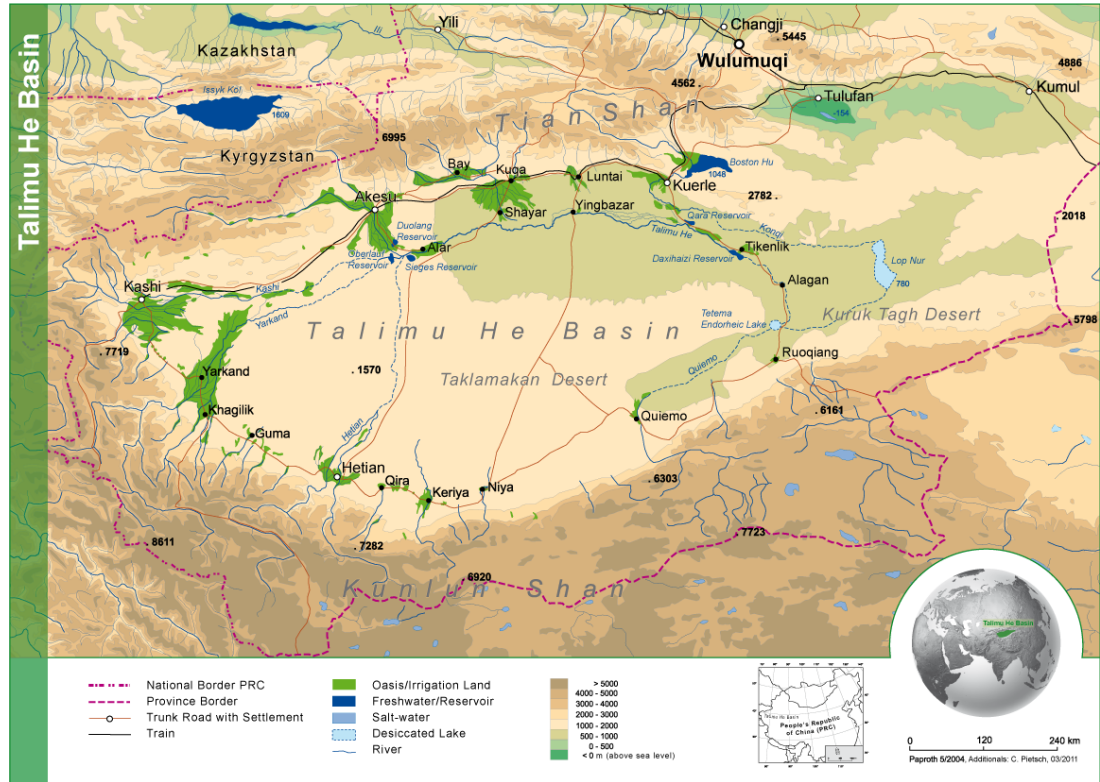
Fig. 1.3: Map illustrating the geographic setting of the Tarim basin including its terrain, oasis settlements and reservoirs (Paproth, 2004).

Chapter 2

Object based change detection of Central Asian Tugai vegetation with very high spatial resolution satellite imagery

With Michael Förster, Alishir Kurban & Birgit Kleinschmit

Abstract

Ecological restoration of degraded riparian Tugai forests in north-western China is a key driver to combat desertification in this region. Recent restoration efforts attempt to recover the forest along with its most dominant tree species, *Populus euphratica*. The present research observed the response of natural vegetation using an object based change detection method on Quick-Bird (2005) and WorldView2 (2011) data. We applied the region growing approach to derived Normalized Difference Vegetation Index (NDVI) values in order to identify single *P. euphratica* trees, delineate tree crown areas and quantify crown diameter changes. Results were compared to 59 reference trees. The findings confirmed a positive tree crown growth and suggest a crown diameter increase of 1.14 meters, on average. On a single tree basis, tree crown diameters of larger crowns were generally underestimated. Small crowns were slightly underestimated in QuickBird and overestimated in Worldview2 images. The results of the automated tree crown delineation show a moderate relation to field reference data with R^2_{2005}: 0.36 and R^2_{2011}: 0.48. The object based image analysis (OBIA) method proved to be applicable in sparse riparian Tugai forests and showed great suitability to evaluate ecological restoration efforts in an endangered ecosystem.

2.1 Introduction

Ecological restoration of degraded riparian Tugai forests in north-western China is a key driver to combat desertification in this region. Past and current restoration efforts attempt to recover the forest along the Tarim river with its most dominant tree species, Euphrates Poplar *(Populus euphratica)*, which provides desirable services to the local ecosystem such as sand fixation, wind break, and riverbank protection (Weisgerber, 1994). The response of the natural vegetation to applied restoration decisions are of particular interest to restoration managers, who seek for accurate long-term monitoring which requires the detection of change and quantification of its rate (Coppin et al., 2004).

Current field-survey methods deliver accurate data for the detection and quantification of forest change but may not be suitable for long-term and large scale monitoring due to low sample coverage and infrequent survey opportunities (Pouliot et al., 2002). Furthermore, in large arid or semi-arid areas, where vegetation cover is usually sparse and scattered, field surveys become time-consuming and cost intensive. In this context, remote sensing offers several desirable characteristics from a forest restoration monitoring perspective including large footprint sizes, and regular data collection cycles (Chubey et al., 2006). Nevertheless, the potential to detect changes in forest ecosystems are intrinsically limited by the satellite images spatial resolution (Coppin et al., 2004). Generally, medium spatial resolution ($\sim$ 30 m) sensors such as Landsat, SPOT, or ASTER have the potential to monitor changes in large forest stands ($>$ 10 ha). Typical approaches detect forest cover change due to clear cuttings (Desclée et al., 2006) or selective harvesting (Kennedy et al., 2007; Sader et al., 2003). The results are reliable and have been, for instance, operationally utilized by the Swedish Forest Agency to verify cutting permits (Olsson et al., 2005).

With the launch of QuickBird2 (QB) (2001), GeoEye-1 (2008), and World-View2 (WV2) (2009), data from three satellites with very high spatial resolution (VHSR) sensors are available. This changed the opportunities for the analysis of forest ecosystems using remote sensing and shifted the scale of interest from forest stands down to the individual tree level (Falkowski et al., 2009).

The spatial resolution in a sub-meter dimension (< 0.8 m) allowed reliable computation of several forest inventory parameters such as canopy closure (Leckie et al., 2005), stem density (Hirata, 2008), and crown size (Ozdemir, 2008). Combining VHSR data with the height information from light detection and ranging (LiDAR) data allowed accurate recognition of tree crowns and the determination of tree height (Leckie et al., 2003a), tree volume (Mora et al., 2013), and, by means of allometric equations, improved estimations of the above ground forest biomass and carbon stocks (Bright et al., 2012). However, its operational implementation in forest ecosystem analysis is still limited due to the high cost for large area surveys.

In VHSR imagery, the target entity (individual tree) is normally composed of several pixels with a high degree of spatial detail. In order to allow meaningful image analysis, groups of homogeneous pixels need to be aggregated into one object, the individual tree object. The aggregation process suggested a change from traditional pixel based image analysis towards an object based image analysis (OBIA) (Blaschke, 2010). With the OBIA approach, each image tree object can be described by its spectral characteristics as well as spatial features such as shape, position, size, and the relationship to neighboring objects (Blaschke et al., 2011) and hence allowed the development of semi-automated algorithms for tree cover information extracted for each tree entity. The core of the developed information extraction algorithms relies on sub processes such as a) tree crown detection and b) tree crown delineation, whereas for some methods, tree crown detection is a required step prior to crown delineation (Ke and Quackenbush, 2011b).

 A range of methods for tree crown detection exist in the literature including local maximum (LM) filtering (Gebreslasie et al., 2011; Wulder et al., 2000, 2004), scale analysis (Pouliot et al., 2005), template matching (Niccolai et al., 2010) and directional local filtering (van Coillie et al., 2012). An emerging approach is the LM filtering which applies a moving window and takes the pixel with the maximum value to represent the treetop (Pouliot et al., 2002). A key matter remains the size of the moving-window which is dependent on the relationship between the tree-crown dimension and spatial resolution of the image (Gougeon and Moore, 1988). A previous study from Gebreslasie et al. (2011) used a panchromatic IKONOS image for the detection of tree location in a plantation forest with mainly flooded

gum (*Eucalyptus grandis*) in KwaZulu-Natal, South Africa. The approach included Gaussian smoothing, and vegetation masking prior two LM filtering approaches with: a) a variable window size selection based on semivariogram techniques and b) a standard fixed window size. In young dense plantation forest the variable window size approach achieved 75% detection accuracy. The accuracy increased (up to 90%) with increasing tree age and decreasing tree density. However, the fixed window size LM filtering approach achieved 67% detection accuracy in young forest stands and up to 88% in the older stands.

Wulder et al. (2004) compared LM filtering for the identification of individual trees on a 1 meter airborne MEIS II and a 1 meter IKONOS image in a plantation forest and a mature stand of Douglas fir (*Pseudotsuga menziesii*) and western red cedar (*Thuja plicata*) in Canada. The LM filtering with variable window size performed poorly on the IKONOS image, resulting in low overall accuracy (61%) and large errors of commission (48%). However, the results from the LM filtering with a 3 x 3 fixed window size on the IKONOS image indicated that individual trees were identified with greater accuracy (85%). A LM filter with a fixed window size is used in the present study.

Tree crown delineation algorithms are based on the underlying assumption that crown tops have higher spectral reflectance than the lower parts of the crown, particularly at the boundaries between crowns (Katoh and Gougeon, 2012). Today, a variety of methods for tree crown delineation exist and can be generally categorized into, valley following (Gougeon and Leckie, 2006; Leckie et al., 2003b), region growing (Bunting and Lucas, 2006; Culvenor, 2002; Pouliot et al., 2002; Tiede et al., 2008) and watershed segmentation (Wang et al., 2004). The region growing method is a threshold-based clustering approach which requires the maxima-derived treetops from the LM filter approach as starting point and a specified threshold value as boundary constraint (Culvenor, 2002). Examples of region growing applications can be found in open mixed species forest with crowns of differing crown shape and size (Bunting and Lucas, 2006) or even aged Mountain Ash forest (*Eucalyptus regnans*) (Culvenor, 2002), both in Australia.

Change detection of tree crown objects with VHSR satellite imagery have been developed recently (Ardila et al., 2012a,b; van der Sande, 2010). Ardila et al. (2012a) introduced a multi-temporal detection strategy based on active

contours to monitor urban tree crowns in a series of very high resolution aerial images in Enschede and Delft, The Netherlands. The identification of abrupt and gradual tree crown changes was computed on a one-to-one object comparison which performed superior to an alternative region growing segmentation approach. Another promising methodology was introduced by Ardila et al. (2012b), where crown changes as well as change uncertainty of trees in an urban environment Enschede and Delft are quantified. Their method iteratively fits a Gaussian function to crown membership in QB and aerial images of two dates and afterwards identified tree crown elliptical objects. For the retrieved tree crown objects crisp changes are identified. Additionally, change uncertainties are computed based on fuzzy membership functions which take spatial characteristics and mixed-pixel effects of tree crown pixel locations into account. Both previous studies were applied in urban environments and used visual interpretation and digitization of the input images as reference data for quantitative performance evaluation.

While there have been studies assessing multi-temporal change detection of urban trees, to our knowledge no studies investigated long-term changes of degraded open Tugai forest based on single tree crowns with VHSR imagery and neither were they validated with field-based crown diameter measurements. Therefore, the objective of this study was to apply the OBIA approach to quantify tree crown changes based on object to object comparison using VHSR imagery (QB and WV2). The study area was a Central Asian Tugai forest in the lower reaches of the Tarim River in northwest China, which experienced recent revitalisation due to ecosystem restoration efforts. Accuracies for tree crown diameter measures are produced and compared to reference data of visual tree delineation and field-based tree crown measurements. Finally, we indicate the suitability of the proposed method with regards to ecosystem restoration evaluation purposes. The following research questions were addressed in this study:

1. How did *Populus euphratica* tree crowns develop during 2005 and 2011 in the lower reaches of the Tarim River?
2. How accurate are OBIA tree crown delineation results in comparison to a) visually interpreted and digitised and b) terrestrial tree crown measurements?
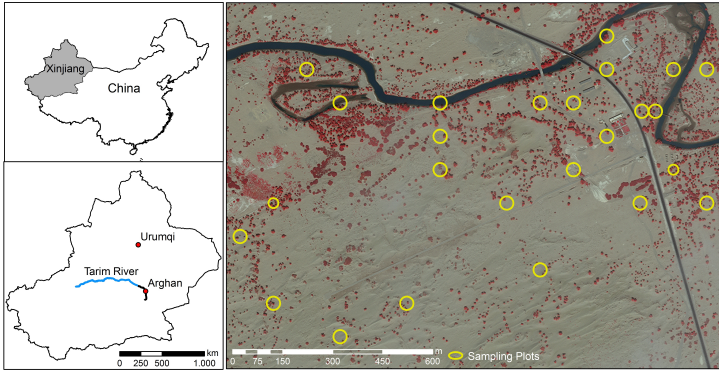
Fig. 2.1: Location of the Xinjiang Uyghur Autonomous Region in China (upper left); Study area at Arghan, along the lower reaches of Tarim River Basin (black line) in Xinjiang Uyghur Autonomous Region (lower left); Location of 25 randomly selected field plots established by Lam et al. (2011) (background image: WV2, date: 29/07/2011, False Colour Composite) (right)

2.2 Methodology

2.2.1 Study area

The study area (Fig. 2.1) is located at the Arghan forest station in the Xinjiang Uyghur Autonomous Region in north-west China where the old Tarim River and the Chiwinkol river branch merge (N $40°8.72'$ E $88°21.26'$). The regional climate shows extreme arid characteristics with precipitation below 50 mm and potential evaporation above 2000 mm. per annum (Chen et al., 2006c). Average monthly temperatures vary from just under $-12°$ C in January, to over $27°$ C in July, while the annual average is at $11.7°$ C. The area is dominated by open sandy areas with dense clusters of *Populus euphratica* along the riverbanks and to sparse isolated trees towards the desert. A forest inventory in 2004/2005 revealed that about 4500 *P. euphratica* trees exist within the study area (Lam et al., 2011).

Common shrub species in the area include *Tamarix ramosissima*, *Tamarix hispida*, *Tamarix leptostachys*, *Elaeagnus angustifolia*, and *Karelina caspica*.

These are all drought-enduring and salt-tolerant species (Zhou et al., 2010), however as phreatophytes their roots need continuous contact to groundwater for their growth and survival ((Thevs et al., 2012)). Although there are some old stumps, no silvicultural management operations have been carried out and the forest can be considered to be in a semi-natural stage. The area represents the characteristic floristic composition and health situation of Tugai floodplain vegetation at the lower reaches of the Tarim river.

2.2.2 Ground Reference Data

The open Tugai vegetation in the research area was mapped in a stratified random sample covering the full range of vegetation diversity and density. For a consistent and comparable long time monitoring, twenty-five permanent sampling plots were established in 2005 (Lam et al., 2011) (Fig. 2.1). The default plot radius was 20 m. In areas with fewer large trees, the plot size was decreased to 15 m. Within the sampling plots, 62 reference trees were randomly selected and their height, diameter at breast height (DBH), and crown diameter were measured. The measurements were conducted in the summer of 2005 and 2011 during the vegetation's maximum development phase. Tree crown diameters were derived by projecting the edges of the crown to the ground and measuring the length of the longest canopy axis (major axis) and the crown axis perpendicular to this axis (minor axis). The average of both values provides the mean crown diameter, a single summary value to evaluate image crown delineations.

2.2.3 Image Acquisition and Preprocessing

Two very high resolution satellite imageries from 2005 and 2011 were used in this work. On 20th of July 2005, the QB satellite acquired an image of the study area in four spectral bands covering blue, green, red, and near-infrared (NIR). The WV2 satellite recorded the same area on 29th of July 2011. Beside the four standard bands (blue, green, red, NIR), the WV2 imagery also contains 4 additional bands (coastal 0.400 - 0.450 μm, yellow 0.585 - 0.625 μm, red-edge 0.705 - 0.745 μm, and additional NIR 0.860 - 1.040 μm). The

data provider resampled the panchromatic ground resolution to 0.6 m (QB) and 0.5 m (WV2) and multispectral resolution to 2.4 m (QB) and 2.0 m (WV2) and radiometrically corrected the image pixels before delivery. Because both sensors are in sun synchronous orbit their nodal crossing time is similar (see Table 2.1). The difference of nine days between the acquisition dates result in a 1.41 min shift in acquisition time and hence in a slightly different sun elevation and azimuth. However, the major dissimilarity between the images is the off nadir view angle. The view angle of the QB scene is 12.5° while the WV2 off nadir angle is about 5.2° larger.

We corrected the images geometrically and calculated top of atmosphere reflectance values using sensor and band specific calibration factors (Krause, 2005; Updike and Comp, 2010). The Hyperspherical Colour Sharpening (HCS) (Padwick et al., 2010) algorithm was applied to fuse the multispectral and panchromatic bands into one multispectral dataset with a final spatial resolution of 0.6 m (QB) and 0.5 m (WV2). For the analysis were normalized difference, ratio-based and soil-line-related vegetation indices calculated and employed. Apart from the original normalized difference vegetation index (NDVI) (Tucker, 1979), its red edge adaptation (NDVI-RE) (Gitelson and Merzlyak, 1994) and its modified form (Mod-NDVI-RE) (Sims and Gamon, 2002) was the Green NDVI (Gitelson et al., 1996) and the normalized difference water index (NDWI) (McFeeters, 1996) created. As ratio-based vegetation index served the Simple Ratio Index (SRI) (Jordan, 1969). The used soil-line vegetation indices were the soil-adjusted vegetation index (SAVI) (Huete, 1988) its modified form (MSAVI) (Qi et al., 1994) and its

Table 2.1: Main acquisition parameters for QB and WV2 images

	Date of acquisition	Acquisition time	Spatial resolution (panchromatic /multispectral)	Sun Elevation angle	Sun Azimuth angle	Off-Nadir view angle	Sensor Azimuth angle
		(*GMT*)	(*m*)	(°)	(°)	(°)	(°)
QB	07/20/2005	05:12:53	0.6 / 2.4	66.9	142.0	12.5	207.7
WV2	07/29/2011	05:14:34	0.5 / 2.0	65.4	144.9	17.7	55.1

optimized form (OSAVI) (Rondeaux et al., 1996).

The NDVI layer was used to create a vegetation mask using a multi-threshold segmentation which splits and classifies image objects based on a automatic NDVI threshold selection. The algorithm uses a combination of histogram-based methods and the homogeneity measurement of multi-resolution segmentation to calculate a threshold dividing the selected set of pixels into two subsets, so that heterogeneity is increased to a maximum (eCognition, 2012).

2.2.4 OBIA approach for Change Detection

The change detection approach we present here was applied to both acquired images and combines six sequential steps to: (A) classify tree, shrub and grassland areas; (B) detect individual tree seed points with local maxima values, (C) delineate seeds into tree crown object, (D) post-process tree crown objects, (E) quantitatively assess the tree detection and crown delineation, and finally (F) calculate detected changes between 2005 and 2011.

A) Vegetation Classification

Tree crown identification is largely affected by the low spectral separability of tree crown pixels with respect to other vegetated surfaces such as shrub and grass cover, which impede the correct identification and delineation of tree crowns (Ardila et al., 2012a). Hence, our first step was to identify shrub and grassland cover and exclude them prior to tree detection (Fig. 2.2). In total 407 training areas were manually selected based on field information and visual image interpretation (tree cover: 170, shrub cover: 175 and grassland cover: 62). The Classification And Regression Tree (CART) classifier was used to build a decision tree model with mean values of the original spectral bands of the QB and WV2 sensor and mean values of vegetation indices, listed in section 2.2.3. The classifier creates a binary tree model with maximal depth using the impurity Gini index (Breiman et al., 1984) and prunes it back to obtain the optimal tree by determining the lowest misclassification errors (Laliberte et al., 2007). We allowed a maximum tree depth of 6

Fig. 2.2 *P. euphratica* tree cover of the study area in false color composite images (QB - 2005 - upper left, WV2 - 2011 - lower left) with image inlets of their corresponding NDVI (dark - low values, bright - high values). Tree photographs (upper row - 2005, lower row - 2011) correspond to green and red vectors.
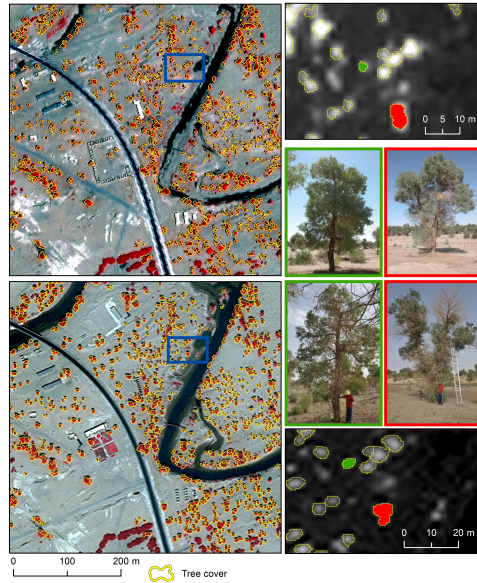
nodes with a minimum number of 5 samples per node, and a 6-fold cross validation. Based upon the produced decision tree model, threshold values for separating the three classes could be afterwards implemented as a rule set in the eCognition (Trimble Geospatial, version 8.8.) software.

B) Tree Crown Detection

Under normal conditions is the crown peak of deciduous trees more likely to be directly illuminated, and has therefore higher spectral reflectance than the crown edge (Culvenor, 2002). To identify probable *P. euphratica* crown peaks we applied a pixel based minimum / maximum filter on the NDVI layer. The filter effectively accentuates crown edges with high values while values drop in areas where the NDVI increases and plunge to zero at NDVI maximum. Next, without using hard coded NDVI thresholds, we assigned filter pixels with the value 0 (highest NDVI value) as crown peak. In comparison to conifers, the *P. euphratica* crown can be morphologically charac-

Fig. 2.3 Example of tree
crowns delineated in the
images of QB-2005 (left
column) and WV2-2011
(right column). The top row
images display the minimum
/ maximum filter band and the
assigned crown peaks (step
B). The middle row images
illustrates the NDVI band and
derived candidate seeds (first
iteration)(step C) whereas the
bottom row images show false
color composites with the
final crown objects.
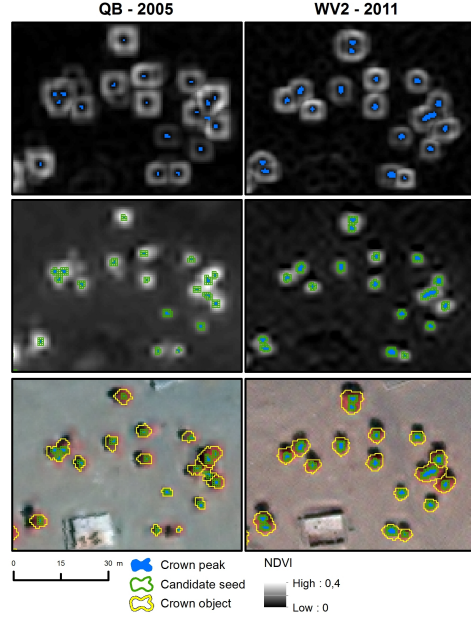
terised as relatively flat. Therefore, we considered pixels in the immediate
vicinity of the declared crown peaks and with a filter value below or equal
to 0.03 to belong to the crown peak (Fig. 2.3 - top row). We restricted the
search domain to the previously created tree cover area and fixed the search
range to 7 x 7 pixels filter window.

C) Tree Crown Delineation

To delineate crown peaks into individual tree cover objects we applied a
threshold based region growing approach implemented in the Conditional
Quad Tree segmentation (eCognition, 2010). The procedure iteratively seg-
ments tree cover objects into quadtree grids consisting of squares (eCogni-
tion, 2012) where the user defined conditions of a) minimum object size (1)
and b) adjacent existence of crown peak objects are met (Fig. 2.3 - middle
row). Next, crown peak objects grew into or merged with neighboring tree
cover objects if the mean NDVI difference was below a predefined threshold

($\leq$ 0.01). With each iteration grew the crown peak larger until the boundary of the tree cover (step A) was reached or a neighbouring crown blocked its growth (Fig. 2.3 - bottom row). Crown peaks adjacent to one another were merged in the first two steps of region growing.

D) Post processing

Tree crown borders were smoothed using a morphology operation which applied a binary mask. Image objects completely containing the mask were added to the tree crown and smaller holes inside the tree crowns were filled.

The appearance of tree crowns in VHSR satellite imagery are affected by the sun illumination angle and the sensor off nadir view angle (Song et al., 2010). As the off nadir viewing increases the size of the projected tree crown in the image, we used a view angle correction factor F in order to have comparable crown delineation results of the QB and WV2 sensors. The angle correction was applied for the statistics and did not alter the crown objects. Factor F was obtained by dividing 1 by the cosine from the sensor off nadir view angle called theta [F = 1 / cos (theta)].

E) Accuracy Assessment

For validation of tree detection and crown delineation we used: a) manually digitized crowns as reference crowns and b) field measured crown diameters as ground truth. The tree detection error was analysed at the individual tree level. We computed the ratio between reference crowns to crown seeds from the local maxima approach (adapted from Leckie et al. (2004) modified by Ke and Quackenbush (2011a)). In our study, error of omission was counted when no seed was identified within the boundary of an existing reference crown (0 seed: 1 reference tree) and error of commission was registered when a seed was within an image object other than a reference tree (1 seed: 0 reference tree). We considered a tree as correctly identified when a single seed was completely within one reference tree boundary (1 seed: 1 reference tree). Two or more seeds in one reference tree illustrated a commission error, this case was registered as 2:1 (or $\geq$ 3: 1 for three or more seeds) correspondence. In the case where a group of trees (e.g. three trees) was erroneously

covered by a single seed, the corresponding ratio would have been 1:3 (1 seed: 3 reference trees).

To compare field measured crown diameter vs. automated crown diameter we performed an analysis of linear regression outliers to determine those field measured crown diameter values that were likely to be a measurement error. These outliers were excluded from the analysis. In order to quantify crown measurement errors, we compared the mean crown diameter from the automatically extracted and manually digitized tree crowns with the averaged field measured crown diameter. The root mean square error (RMSE) and a coefficient of determination R^2 were used to quantify the deviation of tree crown diameters between remote sensing derived crowns (automatically extracted and manually digitized) and field measured crowns.

F) Change Calculation

We selected in each image delineated reference tree crowns and measured the major axis (passing through the tree peak) and the perpendicular minor axis of the tree crowns. The arithmetic mean of both values marked the image based crown diameter. We compared the image derived crown diameter between the 2005 and 2011 and calculated the detected changes.

2.3 Results

From the 4.500 inventoried *P. euphratica* trees were about 3.610 (80,2%) in the QB and around 3.455 (76,7%) in the WV2 imagery successfully recognised. Between 2005 and 2011 disappeared 180 trees and 25 new trees were identified. However, the average tree cover increased from 26,77 m^2 to 31,22 m^2 between 2005 and 2011. The following sections describe the results of the undertaken change analysis focusing solely on the reference trees.

Table 2.2: Descriptive statistics for reference *P. euphratica* trees used in growth evaluation (*N* = 62)

	height (m)				DBH (cm)				tree crown diameter (m)			
	min	max	mean	sd	min	max	mean	sd	min	max	mean	sd
2005	2.1	15.7	6.9	2.6	1.7	107.7	29.5	16.5	2.5	7.2	4.4	1.0
2011	3.2	13.6	7.6	2.3	6.0	111.0	34.2	17.9	2.4	7.7	4.9	1.3

2.3.1 Descriptive analysis of field data

A total of 62 *P. euphratica* reference trees were measured in the field for change detection analysis. Descriptive statistics (Table 2.2) of the tree attributes indicate that on average tree heights increased from 6.9 to 7.6 m and the mean DBH rose from 29.5 to 34.2 cm. Crown diameters ranged from 2.5 to 7.2 m in 2005 and 2.4 to 7.7 m in 2011. The mean crown diameter increased from 4.4 m to 4.9 m over the last 6 years.

2.3.2 Tree Crown Detection

Table 2.3 shows the tree detection results obtained after applying a LM filter to both images. The large number of correctly identified tree crowns (QB: 54; WV2: 53) was achieved because of the absence of disturbing understorey vegetation, of similar spectral behaviour, and primarily isolated trees resulting in low forest complexity. However, by comparing the results of both images it can be concluded that in the QB image were more trees correctly identified than in the WV2 image. The error of omission (0:1) was low in both scenes and occurred only in areas with small tree crowns adjacent to medium trees. The maximum NDVI value of small trees is generally lower compared to medium size trees. If a small and medium sized tree occurs in one filter window instance, the small tree will be ignored and the medium sized tree gets the LM assigned. In neither of the two images was a false positive case identified. Errors of commission (2:1 or 3:1) occurred in 6 trees of the QB image and in 8 trees within the WV2 image.

Table 2.3: Results of tree detection using fixed size LM filter and mean difference to maximum NDVI > 0.03.

	tree seed vs. reference crowns				
	0:1	1:0	1:1	2:1	3:1
QB - 2005	2	0	54	6	0
WV2 - 2011	1	0	53	5	3

2.3.3 Tree Crown Delineation

The conducted linear regression outlier test identified a total of three outliers (4.8% of the whole dataset) that appeared inconsistent with the remainder of the data. Because there was only one outlier in the 2005 data set and two outliers in the 2011 data set, the regression diagnostics identified these observations reliably (for all $p < 0.002$). All outlier were removed and 59 trees remained in the dataset. Data in table 2.4 reveal that diameters from manually digitized crowns correspond better with field measurements than automatically extracted crowns. For both years the RMSE was lower ($RMSE_{2005}$: 0.96 m and $RMSE_{2011}$: 0.69 m) and R^2 higher (R^2_{2005}: 0.49 and R^2_{2011}: 0.75). This is, among other factors, because the diameter range of digitized crowns ($range_{2005}$: 1.62 - 6.15 cm; $range_{2011}$: 2.86 - 7.62 cm) is smaller than

Fig. 2.4 Example of automatically delineated *P. euphratica* tree crowns in false color composite QB (top row) and WV2 (bottom row) images. The overview map shows the location of the close up views within the study area.

Crown object
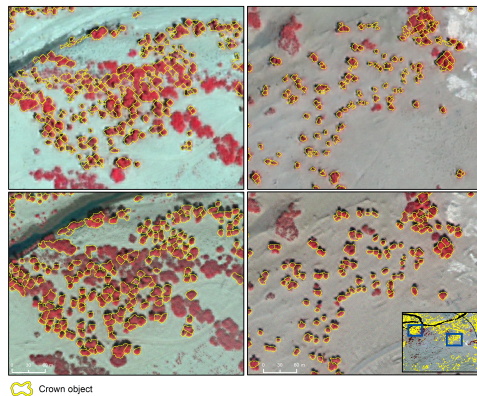
the diameter range of automatically extracted crowns (range$_{2005}$: 0.60 - 7.20 cm; range$_{2011}$: 2.38 - 7.62 cm). The magnitude of error for the automatically extracted crowns has approximately the size of two pan sharpened image pixels (RMSE.QB$_{2005}$: 1.16 m; RMSE.WV2$_{2011}$: 1.03 m).

Comparing diameters of individual crowns by means of their absolute difference, the difference between remote sensing derived (automatically extracted and manually digitized) and field measured crown diameters, indicated a greater crown diameter underestimation in 2005 and an evenly balanced crown diameter estimation in 2011 (Fig. 2.5). Equally for both years, larger crowns tended to be more underestimated by the automated delineation approach. For 2011 there was a minor overestimation of small crowns. In 2005, small crowns were slightly underestimated. However, the automated delineation results were not significantly different from those manually digitized (p.2005: 0.49; p.2011: 0.11).

2.3.4 Change Detection

Table 2.5 summarizes the detected changes of *P. euphratica* crown diameters between 2005 and 2011. An overall crown diameter rise was detected in all methods. The field measured results indicated a crown diameter growth of 0.61 m on average. Considering the field measured data as reference, the automatic delineation method overestimated crown diameters by 0.53 m while the diameters of manually digitized crowns were overestimated by 0.4 m, on average. The main reason for overrating is the crown diameter underestima-

Table 2.4: Mean crown diameter measurement error obtained from automated delineations and manually digitization compared with ground truth field data (*N* 59, outliers removed).

Error measure	2005		2011	
	Automated	Digitized	Automated	Digitized
RMSE (m)	1.16	0.96	1.03	0.69
R^2	0.36	0.49	0.48	0.75

Fig. 2.5 The relation between
absolute differences in crown
diameter measured from au-
tomatically delineated and
manually digitized crown di-
ameters to ground-measured
crown diameters (top: 2005;
bottom: 2011). Third degree
polynomial line graph sum-
marizes the relationships;
(digitized - solid black, auto-
mated – dashed black)
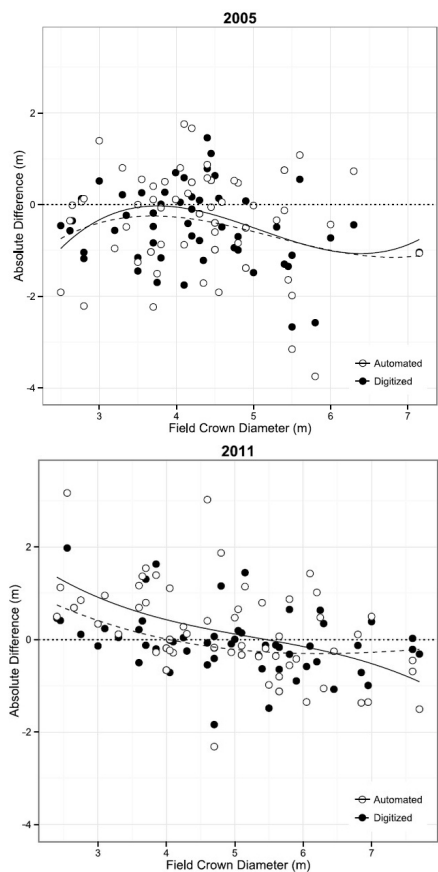
tion in 2005 from the QB scene. The automated region growing approach
underestimated crowns by 0.35 m and the digitizing method underestimated
crowns by 0.47 m, on average (Fig. 2.6). On a single tree level were negative
crown diameter changes of up to 2.3 m and positive crown diameter changes
of up to 4 m observed.

A scatter diagram and a crown diameter change distribution were used to de-
termine the relationship between crown diameter measurements from 2005

Fig. 2.6 Example of 4 study plots (black) with automatically (yellow) and manually (blue) delineated *P. euphratica* tree crowns in false color composite QB (left column) and WV2 (right column) images.
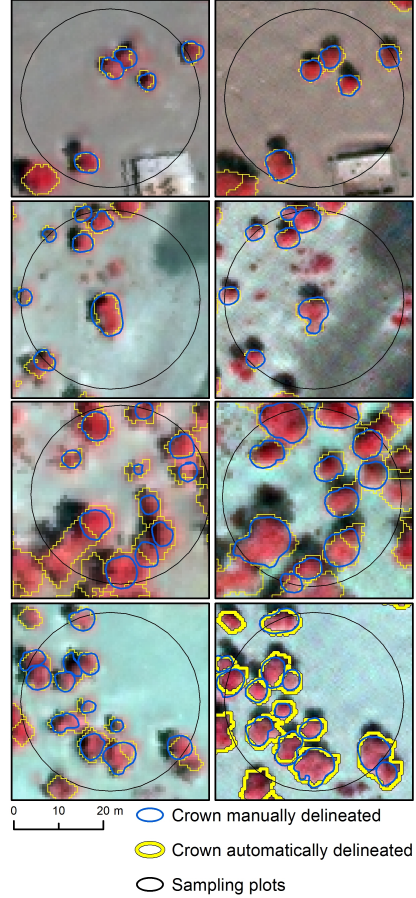
and 2011 (Fig. 2.7). All points left from the 1:1 black reference line indicate a crown diameter increase; points on the other side indicate a decrease. The results in figure 2.7 indicate that projected points cluster closely around their mean for field collected crown diameter (SD_{change}: 0.85) and manually digitized crown diameter (SD_{change}: 0.89) while projected points of the automatic delineation (SD_{change}: 1.28) are further away from their mean. Points

Table 2.5: Summary change statistics for *P. euphratica* crown diameters between 2005 and 2011 (*N* 59).

Method	crown diameter ($\bar{x}$)		change crown diameter ($\bar{x}$)	95% Confidence Interval for change ($\bar{x}$)	
	2005	2011	Total (Annual)	Lower	Upper
Field (m)	4.29	4.90	0.61 (.10)	0.39	0.83 ($\pm$ .22)
Digitized (m)	3.82	4.83	1.01 (.17)	0.78	1.24 ($\pm$ .23)
Automated (m)	3.94	5.08	1.14 (.19)	0.81	1.47 ($\pm$ .33)

beyond the 95% confidence interval may be subject to errors, and those errors contribute to the uncertainty of the measurements.

2.4 Discussion

In this study, we applied an object based change detection method to a semi-arid open *P. euphratica* Tugai forest, aiming to quantify the rate of tree crown changes over a period of six years. The implemented OBIA approach produced meaningful image objects that resemble *P. euphratica* tree crowns (Fig. 2.4). Our results demonstrate that derived tree crown diameter estimates from VHSR imagery agree reasonably well with field reference data, with an average RMSE of 1.16 m (2005) and 1.03 m (2011) and can therefore support field based tree crown monitoring efforts. Essential characteristics of the applied method and the obtained results are discussed below.

2.4.1 Field reference data

Various factors may influence the accuracy of tree diameter estimation in this study. One of the most probable source of error are the in-situ measured reference data for accuracy validation. These data are not 'ground truth', as it is often erroneously referred to (Foody, 2010), but may contain uncertainty (Richter et al., 2011). Our field data were collected in 2005 and 2011 by two

Fig. 2.7 Scatterplots of crown diameters in 2005 (x axis) and 2011 (y axis) illustrate the change detected for each method. A 1:1 reference line is drawn as black solid line. Semi-transparent 'shadow' points show the distribution of change scores with thin grey lines leading from each raw measurement point to its shadow projection on the change distribution. The range of the change distribution is drawn as a blue line beneath the shadow points. Averages for 2005 and 2011 crown diameters are plotted as thin dashed vertical and horizontal lines. Rug plots are presented for the distributions of 2005 (at the top of graphic) and 2011 (on the right side). The 95% confidence interval for the change results is shown as a green dashed band. field measured (top); manually digitized (middle); automatically delineated (bottom).
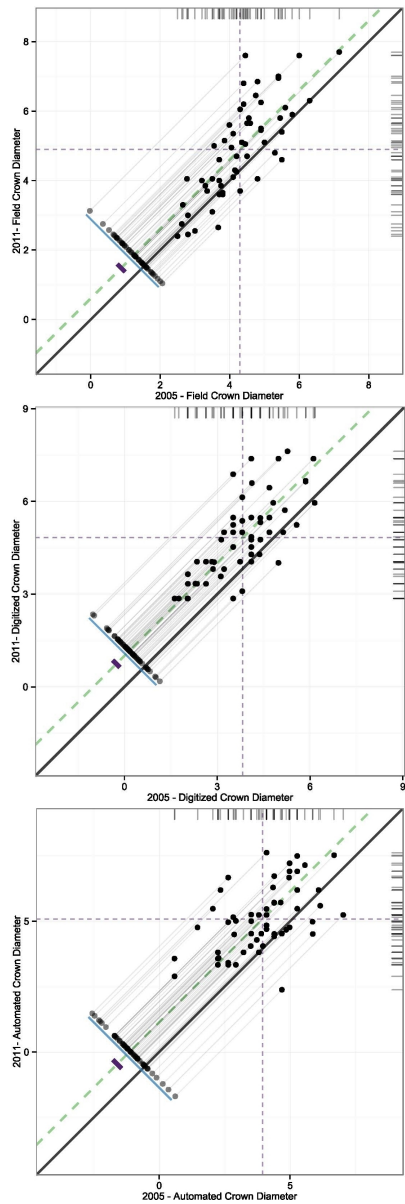
different groups of people, using the same measurement process. Assuming both groups measured carefully and precisely, differing interpretation of the same object may result in subjectivity and bias. How accurate can a vague or rather fuzzy crown border be measured when difficulties arise in defining the 'exact' crown boundary in the field? Lam et al. (2011) observed for the studied *P. euphratica* stand, that the general crown shape varies from relatively dense hemispherical shapes for young and healthy trees to wide open jagged, serrated shapes for older trees. Several old trees lost the top portion of the crown, and some of them formed patches of secondary crowns from dormant buds. When seen from space, these disperse crown forms are not observed as round and may be underrepresented by only two crown diameter measurements. We therefore propose to increase the field crown diameter measurements to four diameter measurements, 45 degree apart from each other as it is carried out during stand area determinations (Röhle, 1986).

2.4.2 Tree Crown Detection and Delineation

The heterogeneous crown form of *P. euphratica* was frequently accompanied by a high within-crown spectral variability. The canopy reflectance plunged in parts of dead primary crowns, lacking photosynthetic material while reflectance rose in parts with foliated secondary crowns. This caused crowns to differ from the typical ellipsoidal crown shapes of other deciduous tree species. The spectral responses to the irregular branch pattern were multiple reflectance peaks, especially in sub-meter resolution imagery (Pouliot et al., 2002). In fact, in 10% of the analysed trees (QB scene, 2005) we obtained at least two reflectance peaks per tree (13% in WV2 scene, 2011). The rising number of multiple reflectance peaks was expected due to the increase of within crown variability with higher spatial and spectral resolution (from 0.6 m to 0.5 m). To illustrate the issue, figure 2.8 presents a three-dimensional view of NDVI values for two trees, one with an irregular crown structure (right) and one medium sized tree with a homogeneous tree crown (left). In normal procedure a tree with three reflectance peaks (crown peaks highlighted in red, Fig. 2.8) would have caused an error of commission (3:1 error). In our case the detection of multiple reflectance peaks in an irregular shaped crown should not be considered as commission error because those peaks exist. However, difficulties arise when to validate detected re-

flectance peaks in the field. Extracting individual vertical structure of tree crowns from LiDAR would improve the analysis since reliable tree height and treetop data are detectable (Chen et al., 2006a). We did not find literature information concerning the distance between LiDAR measured treetop data and crown peaks from sunlit reflectance maxima.

The high accuracy of the individual tree detection that we obtained are consistent with those of Whiteside and Ahmadb (2008), who achieved a local maxima seed detection in Eucalypt dominant savannah with a user accuracy of 84.3% and a producers accuracy of 96.3% within a QB image. In Zhou et al. (2012) field validated detection rate exceeded 82% in Eucalyptus plantation with WV2. In our study, 1:1 detection success ranged from 85.5% in WV2 to 87.1% in QB. The essential difference between above mentioned surveys was because of the existence of undergrowth, shrubs and annual grasses and the homogeneous tree spacing due to plantation outlines.
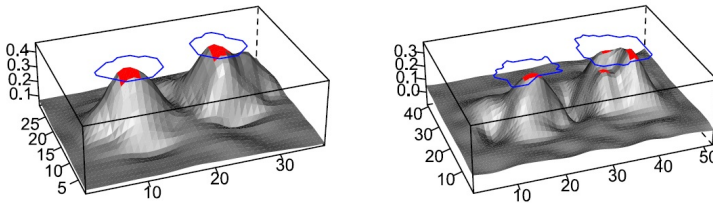
Fig. 2.8: Tree crown detection results for two trees. Tree peaks (red), manually delineated crown (blue) (QB − 2005 (left), WV2 − 2011 (right); Axis labels: x and y − in pixel, z: NDVI values)

The crown diameter from the manually digitized tree crowns agreed better with the field reference data than the results from automated delineation approach. However, the OBIA approach achieved RMSE in both sensor types below two image pixels (Table 2.4). These accuracy levels are similar with studies which compared their results to field-measured crown areas rather than manually digitized reference trees (Pouliot et al., 2002, 2005; Song et al., 2010). One source of error is related to the mixed pixel effect which occurs in the vicinity of the crown boundary and influences the crown bound-

ary delineation result. Mixed pixels tend to smooth reflectance variability and cause tree crown overestimation if included and underestimation if excluded (Rocchini et al., 2013). In our results, the measurements of the crown diameter touch the crown boundary in two sides of the crown axis, therefore appears the mixed pixel effect twice. For the bi-temporal tree crown change detection we selected two peak green summer images because of their adequate quality as well as the phenological stability (Coppin et al., 2004). The quality of the QB image was slightly reduced after the HCS image fusion process due to small NIR artefacts, observed close to tree crown edges.

We also found that the region growing algorithm works better at isolated or scattered trees than in dense or closed forest areas. A uncertainty factor for the crown delineation method is the fact that the method dependence on the presence of crowns peaks. A tree crown peak is almost certainly found at isolated trees, but in dense or closed stocks are situations were a dominant tree covers its neighbour and its peak will remains undetected. The consequence is that the region growing method segments over the dominated tree and the resulting tree crown appears rather big and unshapely.

2.4.3 Change of Vegetation Cover

The long term ecological restoration of degraded riparian Tugai forests along the lower reaches of the Tarim river has beneficial influence on the *P. euphratica* population. Our findings confirmed a positive tree crown growth and suggest a crown diameter increase of 1.14 m, on average. The detected expansion of above ground green biomass corresponds to natural succession and suggests improved groundwater conditions after Ecological Water Diversion from 2000 until 2011 (Zhandong et al., 2009). The results of the automatic tree crown delineation show a moderate relation to the reference data (with R^2_{2005}: 0.36 and R^2_{2011}: 0.48) but can be considered useful due to a similar magnitude of the error like the manually digitized results. The OBIA method proved to be applicable in arid environments with scattered trees such as the sparse riparian Tugai forests and showed great suitability to evaluate ecological restoration efforts in a remote ecosystem.

2.5 Conclusion and Outlook

We used two very high resolution satellite images to quantify recent tree crown diameter changes in a degraded riparian Tugai forest in north-western China. Our results suggest a positive tree crown growth with an average crown diameter increase of 1.14 m. On a single tree basis, small crowns were slightly underestimated in QB and overestimated in WV2. Tree crown diameters of larger crowns were generally underestimated. The results of the automated tree crown delineation show a moderate relation to 59 reference trees measured in the field (R^2_{2005}: 0.36 and R^2_{2011}: 0.48). The automated OBIA method proved to be applicable in scenes of both evaluated sensors for sparse riparian Tugai forest, especially in feature extraction of individual tree crowns and produced useful results.

2.6 Acknowledgements

Chapter 3

The benefit of synthetically generated RapidEye and Landsat 8 data fusion time series for riparian forest disturbance monitoring

With Michael Förster & Birgit Kleinschmit

Abstract

Insect defoliation causes forest disturbances with complex spatial dynamics. In order to monitor affected areas, decision makers seek but often lack information with high spatial and temporal precision. Within the context of a riparian Tugai forest disturbed by the insect *Apocheima cinerarius*, this study examines whether the analysis of a RapidEye time series would benefit from the availability of synthetically generated images at the spatial resolution of RapidEye and the additional temporal resolution of Landsat 8. We applied the Enhanced Spatial and Temporal Adaptive Reflectance Fusion Model (ESTARFM) to downscale Landsat 8 Normalized Difference Vegetation Index (NDVI) scenes to concurrent RapidEye NDVI scenes. We a) performed a pixel-based regression analyses in order to evaluate the quality of the synthetically created NDVI products and b) examined if forest disturbance maps produced with synthetic images improve the accuracy of disturbance detection. The results show that the ESTARFM predictions have a sufficiently good accuracy, with a correlation coefficient between $0.878 < r < 0.919$ ($p < 0.001$) and an average root mean square error $0.015 < RMSE < 0.024$. The overall accuracy of forest disturbance detection with added synthetic images increased from 42.8% to 61.1 & 65.7% compared to the original data set. Forest recovery detection accuracy improved from 59.5% to 80.9%. The main source of error in the disturbance analysis occurs during the temporal interweaving between foliation and defoliation in spring.

3.1 Introduction

Forest disturbances — caused by drought, fire, storms, fungi and insect pests — lead not only to economic losses but also have numerous environmental impacts (Coppin and Bauer, 1996). Remote sensing has long been seen as a useful tool for large scale monitoring of their effects and serves as an early warning system (Banskota et al., 2014). For insect pests the patterns of insect attack, defoliation, and forest recovery are complex and not always fully understood (Hall et al., 2006). In a variety of cases, the spatial and temporal patterns of these disturbance effects start with a slow intensity dispersion, followed by rapid defoliation and regeneration (De Beurs and Townsend, 2008; Kennedy et al., 2010). Therefore, fine scale monitoring and operational planning rely on high temporal and spatial resolution imagery for the assumed time period of the attack. Although the Landsat suite of sensors are suitable to track some forest diseases in terms of temporal coverage, the 30 m spatial resolution limits its applicability for fragmented forests (Arnett et al., 2015).

RapidEye, with a ground sampling distance of 6.5 m is commonly used for grassland mapping (Franke et al., 2012; Schuster et al., 2015), has proven to be valuable for land cover change detection (Behling et al., 2014) and mapping of biophysical forest parameters (Tillack et al., 2014; Wallner et al., 2015).

The RapidEye satellite constellation has been delivering high temporal resolution imagery (Stoll et al., 2012), allowing for greater spatial detail for patterns and objects in comparison to Landsat (Arnett et al., 2015), and provides greater potential for fine scale mapping of local forest disturbances. RapidEye has already been used mono-temporally (Adamczyk and Osberger, 2014; Adelabu et al., 2014; Ortiz et al., 2013) and bi-temporally (Marx, 2010) to detect insect pest outbreaks and forest fire hazards (Arnett et al., 2015). Major storm events were mapped with inter-annual images (Osberger et al., 2013) and intra annual images (Elatawneh et al., 2014) in Central European forests. However, storm events are often one-off events leading to rapid destruction of forest areas, and can be easily identified due to abrupt and significant changes in spectral characteristics. In contrast, subtle changes in forest conditions such as foliage discoloration and gradual

defoliation due to insect pest outbreak are more difficult to detect (Goodwin et al., 2008).

A major challenge for the successful use of satellite imagery for mapping insect pest outbreaks is the timing of image acquisition (Hall et al., 2006) in relation to the life cycle of the defoliator and the phenology of the host. While some remote sensing studies rely on change detection between mid-summer imagery from a non-defoliation year to the defoliation year (De Beurs and Townsend, 2008; Townsend et al., 2004), others analyse pre- and post-outbreak images of the same year in order to detect spectral response differences resulting from insect defoliation (Dennison et al., 2009; Thomas et al., 2007).

Currently, it is practically unreasonable to monitor regional insect outbreaks solely with the commercially operating RapidEye sensor, due to the high costs of obtaining large numbers of high resolution images. To reduce monitoring expenses, the fusion of RapidEye data with sensors operating under a free and open data policy would be a cost-saving alternative. Recently developed data fusion models combine high temporal and low spatial resolution imagery, such as MODerate resolution Imaging Spectrometer (MODIS) , with low temporal and high spatial resolution imagery, like Landsat TM/ETM +, in order to generate a synthetic Landsat-like image at MODIS temporal resolutions (Hilker et al., 2009a; Schmidt et al., 2012).

Widely used data fusion models include: (a) the Spatial and Temporal Adaptive Reflectance Fusion Model (STARFM) (Gao et al., 2006); (b) the Enhanced version of STARFM (ESTARFM) (Zhu et al., 2010); (c) the Modified version of ESTARFM (mESTARFM) (Fu et al., 2013); (d) the Spatial Temporal Adaptive Algorithm for mapping Reflectance Change (STAARCH) (Hilker et al., 2009a); and (e) a semi-physical fusion approach using a Bi-directional Reflectance Distribution Function (Roy et al., 2008).

The fusion models listed here have been successfully applied with Landsat/MODIS configurations in a variety of land cover types ranging from low to high biomass, including the Australian savannah (Schmidt et al., 2012), complex Mediterranean pseudo-steppe landscape in southern Portugal (Senf et al., 2015), dryland forest in Arizona, USA (Walker et al., 2014, 2012) and in mixed broadleaf and coniferous forest in central British Columbia (Hilker

et al., 2009b) and western Alberta, Canada (Coops et al., 2012).

These data fusion methods are mainly based on spatially integrating reflectance observations (Hilker et al., 2009a), and despite not being explicitly designed for mapping abrupt changes such as forest disturbance events, they have been successfully applied (Gaulton et al., 2011; Hilker et al., 2009a; Schmidt et al., 2015). The research from Hilker et al. (2009a), Hilker et al. (2009b), who applied the STAARCH model in dense coniferous forest in west-central Alberta, has shown that forest disturbance-based changes could be identified with improved spatial and temporal accuracies (93% and 88% respectively). Schmidt et al. (2015) applied the STARFM model over a savannah region in central southeast Queensland (Australia) and generated a time series for a period of 12 years with a time-interval of 8 days. They reported high correlations between the synthetic and the observed NDVI values in homogeneous forest and grassland areas. Their high temporal NDVI time series were able to detect primary clearing events with 94% accuracy within 40 days of a clearing event. Tewes et al. (2015) used a RapidEye/MODIS configuration with ESTARFM to monitor vegetation dynamics in a semi-arid rangeland in South Africa and concluded that synthetic image accuracies, while good during phases with little vegetation dynamics, deteriorated during times of quick vegetation growth.

While there have been numerous studies on forest disturbance mapping with a blend of medium (e.g. Landsat) and coarse (e.g. MODIS) resolution sensors, we are not aware of any analysis using a fusion of high (RapidEye) and medium (Landsat 8) resolution sensors in this context.

We therefore examined in this study, whether the analysis of an insect-defoliated riparian Tugai forest would benefit from synthetically generated images at the spatial resolution of RapidEye and the temporal resolution of Landsat 8. The forest disturbance detection accuracies are produced and compared to reference data from visual estimates of foliage classes. Finally, we indicate the suitability of the combined sensor fusion product with regards to forest disturbance monitoring purposes. The following research questions were addressed in this study: (a) Do land cover differences in a semi-arid riparian forest lead to varying degrees of accuracy in the resulting ESTARFM imagery? (b) Can a synthetically derived product be used to detect forest disturbance caused by *Apocheima cinerarius* with increased

accuracy in comparison to the original data set? and (c) Does the temporal resolution of the RapidEye and synthetic Landsat 8 images generated with ESTARFM influence the forest disturbance detection accuracy?

3.2 Materials and methods

3.2.1 Study area

The research was carried out at the Arghan forest station in the Xinjiang Uyghur Autonomous Region (see Fig. 3.1) in north-west China (N 40°8.72′ E 88°21.26′). The climate in this region shows extreme arid characteristics with mean annual rainfall below 50 mm/year and potential evaporation above 2000 mm/year (Chen et al., 2006c). Average monthly air temperatures vary from just under -12 °C in January, to over 27 °C in July, while the annual mean air temperature is about 11.7 °C. Typical vegetation of this floodplain area include open sandy patches with dense clusters of Euphrates Poplar (*Populus euphratica*) along the riverbanks, and sparse isolated trees towards the desert. The average tree age is 60 years (Westermann et al., 2008) and the general tree vitality can be described as degraded (Aishan et al., 2015). The stem density is 24 plants / ha and mean tree height is 7 m and the mean crown diameter is mbox4.9 m (Gärtner et al., 2014). Besides *P. euphratica* , the floodplain forest contains common shrub species such as *Tamarix ramosissima*, *Tamarix hispida*, *Elaeagnus angustifolia*, *Alhagi sparsifolia Shap.* and *Karelina caspica Less.*. These are all drought-enduring and salt-tolerant species (Zhou et al., 2010); however, as phreatophytes their roots need continuous contact with groundwater for their growth and survival (Rumbaur et al., 2015; Thevs et al., 2012). The depth to the groundwater table ranges from 5.5 to >8 m.

Although individual trees have been cut in the area, no silvicultural management operations have been carried out and the forest can be considered to be in a semi-natural stage. The area represents the characteristic floristic composition and health situation of Tugai floodplain vegetation at the lower reaches of the Tarim River.

Five phenological periods are observed for *P. euphratica*. The first phenological phase is the flowering, which lasts from the end of March until the beginning of April. In early April, leaves begin to unfold rapidly and reach full expansion about three weeks later. By that time the caterpillars of *A. cinerarius* hatch from the eggs and proceed to feed on 80 – 90% of the poplar leaves (see Section 3.2.2). Shortly afterwards, the second foliation phase begins, which lasts from mid-May to early June. Leaf senescence (decrease of leaf chlorophyll content) begins in late September and leaves are shed by the end of October or early November (Abdurahman et al., 2013).

3.2.2 Infestation dynamics of A. cinerarius

A. cinerarius (Erschoff, 1874) (Lepidoptera: Geometridae: Ennominae), a cyclic defoliator pest, is a widely distributed moth in northern China and Central Asia (Liu et al., 2014). *A. cinerarius* hibernates as pupae in the soil

Fig. 3.1 Location of the Xinjiang Uyghur Autonomous Region in China (inset); the study area is located at the Arghan forest station and covers approximately 21 km^2 (N 40°8.72′ E 88°21.26′) (Pietsch, 2013).

layer 20 – 50 cm beneath the surface, close to *P. euphratica* tree trunks. Soil temperatures rise to 0 °C in spring (late February or March) and triggers the moths emergence from the cocoon. After mating, the wingless females lay fertilized eggs in openings and under loose scales of tree bark. Once developed, the caterpillars hatch and feed on the buds and leaves of poplars (the caterpillar can defoliate deciduous trees in a few days) (see Fig. 3.2). From late April to mid-May, the caterpillars enter the soil and pupate, beginning the life cycle anew (Beljaev and Ponomarenko, 2005). During the period from 2005 to 2007, between 0.88 and 1.42 million ha in China were infested with poplar defoliators (Ji et al., 2011).
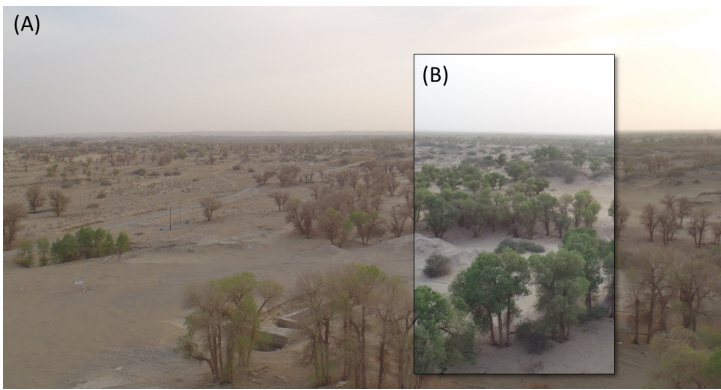
Fig. 3.2: Patches of *P. euphratica* tree clusters defoliated by *A cinerarius* (A). The majority of trees recover from the insect attack and refoliate until the end of May (B). Photo courtesy Tobias Wommelsdorf: A) April 25, 2013, B) May 20, 2013.

3.2.3 Data acquisition

To provide evidence of insect defoliation caused by *A. cinerarius*, images were acquired in the narrow time window between the middle and end of April when changes resulting from defoliation were most observable. Even within this time window the acquisition date of the scenes are crucial. As

shown in Fig. 3.3, acquisition dates for RapidEye (triangles) could miss the leaf foliation peak starting of the defoliation and therefore provide less information about the disturbance (dotted black arrow). In this schematic case, an additional scene at the peak of the first foliation can provide a better estimate of the defoliation (solid black arrows). In order to map the subsequent forest recovery, images acquired within the large time window from mid-May until mid-September would be sufficient (see phenological seasons in Fig. 3.3). The primary high resolution dataset for this project was a Black-
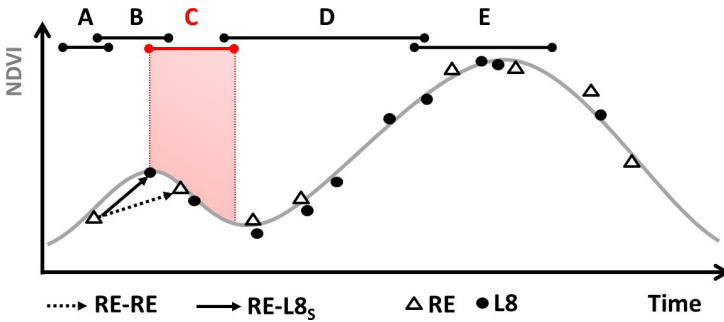
Fig. 3.3: Schematic representation of insect infestation and the altered NDVI curve over time. Dots indicate L8, Triangles indicate RE data. Derived disturbance measures are shown (black and dotted line). Phenological Seasons: A — Flowering, B — First Foliation, C — Defoliation due to Apocheima cinerarius , D — Second Foliation, E — Leaf growth under crown closure.

Bridge RapidEye (RE) satellite image time series, consisting of eight images captured during the 2013 growing season (see Table 3.1). The imagery was delivered as a level 3A product, with radiometric, sensor, and geometric corrections done by the data provider. The spatial resolution of the imagery is 5 m and it has a bit depth of mbox16-bit unsigned integers.

All RapidEye data were geometrically corrected to a previously georeferenced WV2 scene with a ground resolution of 0.5 m, resulting in a final accuracy error of less than half a pixel. Clouds and cloud shadows were masked out manually. We converted digital numbers to Top of Atmosphere (ToA) reflectance values using sensor- and band-specific calibration factors (RapidEye, 2011). Relative radiometric normalization was then performed

Table 3.1: RapidEye (RE) and Landsat 8 (L8) time series from 2013, sorted by the day of year (DOY); vertical bars: two base images pairs (black) and two model cross-check image pairs (grey).

RapidEye (DOI)	ESTARFM Input	Landsat 8 (DOI)	Path/Row	Label
March 29 (88)				RE_{88}
		April 15 (105)	142/32	$L8_{S.105}$
April 20 (110)				RE_{110}
		April 24 (114)	141/32	$L8_{S.114}$
May 16 (136)	base image (t^1)			RE_{136}
	base image (t^1)	May 17 (137)	142/32	$L8_{137}$
May 31 (151)				RE_{151}
		June 2 (153)	142/32	$L8_{S.153}$
		June 11 (162)	141/32	$L8_{S.162}$
		June 27 (178)	141/32	$L8_{S.178}$
		July 4 (185)	142/32	$L8_{S.185}$
July 14 (195)				RE_{195}
		July 20 (201)	142/32	$L8_{S.201}$
	base image (t^2)	July 29 (210)	141/32	$L8_{210}$
July 31 (212)	base image (t^2)			RE_{212}
Aug. 27 (239)				RE_{239}
		Aug. 30 (242)	141/32	$L8_{S.242}$

on the ToA reflectance values using the Iteratively Reweighted Multivariate Alteration Detection (IR-MAD) algorithm (Canty and Nielsen, 2008). The automatic procedure is based on the invariance property of MAD transformation and performs an orthogonal linear regression (Canty and Nielsen, 2008) of the target image pixels on to the reference image pixels. The reference image was a cloud and haze free RapidEye image from July 31st. The normalization of all images was followed by the calculation of the Normalized Difference Vegetation Index (NDVI) (Tucker, 1979). We followed the 'index first then blend' approach rather than the 'blend first then index approach' (Tian et al., 2013) assuming that a linear mixture model is applicable to an index (NDVI) as it is for reflectance bands. That is, the mixed NDVI for each Landsat pixel is the sum of the NDVI weighted by the land cover surface proportions (Jarihani et al., 2014). The assumption could introduce some error in the linear mixture model (Kerdiles and Grondona, 1995) but the procedure reduces the computationally expensive processing by half due

to blending a single index rather than multiple bands (red and NIR) and more importantly increases accuracy due to less error propagation (Jarihani et al., 2014).

An additional medium resolution dataset was acquired consisting of ten Landsat 8 satellite images captured between April 15 and September 10 in 2013 (see Table 3.1). Landsat 8 data are recorded in 185 km swaths and segmented into 185 km x 180 km scenes defined in the second World-wide Reference System (WRS-2) of path (ground track parallel) and row (latitude parallel) coordinates (Roy et al., 2014). The study area is located in the overlapping area between two adjacent paths (141/142) on the same row (32). From the overall ten images acquired, five originate from path 141 and five from path 142.

The imagery was acquired as standard level-one terrain-corrected (L1T) products, which have had systematic radiometric and geometric corrections. As with the preceding RE processing steps, we manually masked out clouds and their shadows, converted digital numbers to ToA reflectance values and normalized all L8 images to a L8 reference image from July 29 according to the IR-MAD technique. The normalization procedure was followed by the NDVI calculation. The pixel size at this point in the processing chain is 30 m. Figure A.2 shows the spectral response curves for both sensors using the red and NIR bands, highlighting the differences for the latter.

As shown schematically in Fig. 3, the scenes RE_{88}, $L8_{S.105}$, RE_{110} and $L8_{S.114}$ were used for the forest disturbance analysis, because these images are in the small window of first leaf foliation and defoliation. All other scenes not utilized for the ESTARFM approach (see Table 3.1) were used to derive the value on the recovery within the second leaf foliation.

3.2.4 Data processing using ESTARFM

The ESTARFM algorithm generates a synthetic image from two base pairs of RapidEye and Landsat 8 images acquired on the same or similar days (t^1 and t^2) and one additional Landsat 8 image from the prediction date (t^3). We selected the RapidEye image from May 16 (DOY 136) and the Landsat 8

image from May 17 (DOY 137) as the first base pair (t^1), and the RapidEye image from July 31 (DOY 212) and the Landsat 8 image from July 29 (DOY 210) as the second base pair (t^2).

We selected the image base pairs according to their time of acquisition in regards to the variability of the vegetation's state. Base pair t^1 represents the time when the potential defoliation occurred and little vegetation is present, while t^2 characterizes the peak vegetation in the middle of the growing season. In total, eight synthetic images were generated with the ESTARFM algorithm. The synthetic images are named: $L8_{S.xx}$ where "S" stands for "synthetic" and xx will be replaced by the DOY.

Prior to the ESTARFM implementation we resampled all L8 images to the spatial resolution of the RE scenes (5 m) using the bilinear resampling method, and co-registered (image to image) all L8 images to the RE base image pairs. We ran the ESTARFM algorithm with the standard settings in regards to the search window size and the number of classes.

3.2.5 Assessment of ESTARFM synthetic RapidEye images

At first we quantitatively assessed the two base pair images t^1 and t^2 (Tbl. 1 image pairs t^1: RE_{136} / $L8_{137}$ and t^2: $L8_{210}$ / RE_{212}) which form the basis of the blending application. We used the linear regression model ($Y = \beta_0 + \beta_1 \cdot x$) do describe the model fit.

Thereafter, we selected two original RapidEye scenes (RE_{151}, RE_{239}) together with their corresponding generated synthetic images ($L8_{S.153}$ and $L8_{S.242}$) in order to cross-check the quality of the ESTARFM predictions (image pair label: cross-check$_1$ & cross-check$_2$). The time lag between the image pairs does not exceed 3 days (see Table 3.1).For both cross-check image pairs was the prediction accuracy assessed spatially by plotting the residuals of the observed vs. predicted RapidEye NDVI linear regression model.

This was followed by a per pixel comparison between the observed vs. predicted NDVI values for a selected set of correlation-based measures, such

as the Pearson correlation coefficient (r), the slope and intercept values. The used error indices were the root mean square error (RMSE) and its normalized version (NRMSE). The cross-check was performed for five different land use / land cover classes. We therefore classified the image with a knowledge-based classification ruleset in eCognition, which differentiated the following land cover classes with very good mapping accuracies (overall accuracy 91.2%): asphalt, cotton field, desert sand, river water and Tugai forest (see Fig. 3.4).

3.2.6 Creation of a time series for forest disturbance analysis

Once the $L8_S$ images were created, the image stack was arranged for the analysis of forest disturbance. The disturbance analysis was based on the relative NDVI difference calculation in which co-registered images from two dates are subtracted pixel by pixel. The difference calculation is shown in Eq. (1) where:

$$D_{ij} = \frac{\left(NDVI_{ij\ T2} - NDVI_{ij\ T1}\right)}{NDVI_{ij\ T1}} * 100 \qquad (3.1)$$

D_{ij} is the disturbance (defoliation) image expressed in percent. $NDVI_{ij\ T2}$ and $NDVI_{ij\ T1}$ are the NDVI values of pixel (i,j) for imagery captured during the first foliation phase $(T1)$, and the imagery captured between defoliation and the next succeeding recovery phase (also known as second foliation) $(T2)$. As shown in Fig. 3.3 (dotted and solid arrows) D_{ij} was created a) with RE imagery only ($NDVI_{RE.88}$; $NDVI_{RE.110}$) and b) with RE and $L8_S$ ($NDVI_{RE88}$; $NDVI_{L8.S.105}$ and $NDVI_{RE.110}$; $NDVI_{L8.S.114}$) in order to evaluate whether the accuracy has increased with the use of synthetic data at the peak of the first foliation.

Furthermore, we calculated the percent recovery rate (R_{ij}) in order to analyse which trees recovered from the preceding defoliation and which deteriorated. The recovery calculation is shown in Eq. (2) where:

$$R_{\text{ij}} = \frac{\left(\sum_{i=1}^{n} NDVI_{\text{ij T3}} - NDVI_{\text{ij T2}}\right)}{NDVI_{\text{ij T2}}} * 100 \qquad (3.2)$$

R_{ij} is the recovery image expressed in percent. As in Eq. (1), the $NDVI_{ij\,T2}$ is the NDVI value of pixel (i,j) for imagery that was captured after defoliation but before the next succeeding recovery phase (*T2*). $NDVI_{ij\,T3}$ belongs to imagery captured during the second foliation and the summer period (where leaf growth is under full crown closure) (*T3*), while variable *n* hold the number of imagery used. R_{ij} was first created with RE imagery only ($NDVI_{RE.110}$; from $NDVI_{RE.136}$ til $NDVI_{RE.253}$) and repeated with RE and L8$_S$ jointly ($NDVI_{L8.S.114}$ and all images between $NDVI_{RE.136}$ - $NDVI_{RE.253}$).

In the last step, we grouped the NDVI percentage differences (D_{ij} and R_{ij}) into one out of four disturbance severity classes (see Table 3.2) based on Buxton and Maclauchlan (2014) and Schomaker et al. (2007).

The accuracy of the disturbance severity classes derived above was assessed spatially with ground reference information. We evaluated field notes, fire tower photos and 131 individual tree photos on 13 established field plots (see Fig. 3.4 and Table S.3 in the online supplementary data). Defoliation severities were assessed for each tree individually, based on the visual estimation of defoliation rates (10% classes) during the peak defoliation and the second foliation phase. In the next step, WV2 and Google Earth imagery was used to search and mark the visually assessed trees in RapidEye as validation pixels. These pixels were used to calculate confusion matrices for each disturbance class and derive user (UA), producer (PA) and overall accuracies (OA) values.
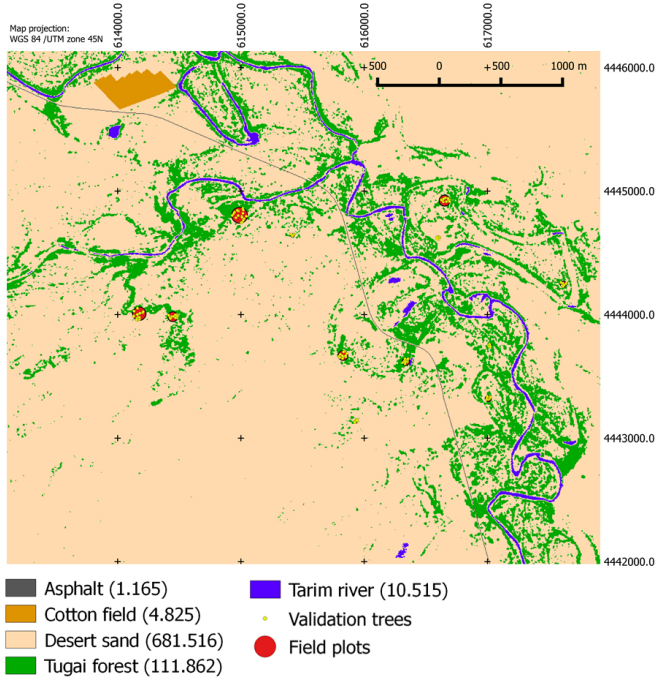
Fig. 3.4: Detailed map of land cover classes found in the study area, where about 13.81% of the total land cover is classified as Tugai forest. Established field plots are shown in red overlaid by selected validation trees (yellow). The number of pixels per land cover class is shown in the legend.

3.3 Results

### 3.3.1 Accuracy of ESTARFM simulation

The Pearson correlation coefficient was determined to assess the strength and direction of the relationship between RE_{NDVI} and $L8_{NDVI}$ values for the two selected base pair images (see Fig. 3.5). There was a strong positive correlation between RE_{NDVI} and $L8_{NDVI}$ values for t^1 : r = .68 and t^2 : r = .795. The linear regression equation for t^1 was: RE_{NDVI} = - .06 + 1.042 $\times$ ($L8_{NDVI}$);

Table 3.2: Grouping schema based on defoliation severities.

| Class number	Class label	Definition	Percent defoliation & recovery [% D_{ij}; R_{ij}]
D_0	No defoliation	vital tree without signs of defoliation	< 0
D_1	Light defoliation	some branch tip and upper crown defoliation, tree is still in good condition	> 0 - 30
D_2	Moderate defoliation	thin foliage, top third of tree is severely defoliated	> 30 - 50
D_3	Severe defoliation	bare branch tips and completely defoliated tops, most trees sustaining > 50% total defoliation, tendency to deterioration	> 50

and for t^2 it was: $RE_{NDVI} = -.061 + 0.893 \times (L8_{NDVI})$. All regression models were statistically significant $p < 0.001$. Figure A.1 shows regression models for four additional image pairs in spring [DOY 105 vs. 110], in early summer [DOY 151 vs. 151; 201 vs. 195] and late summer [DOY 239 vs. 242]. In general the correlation values were strong ($.68 < r < .795$). Intercept values were always negative but close to 0 ($-.097 < \beta_0 < -.038$). Slope values were between $.704 < \beta_1 < 1.632$.

With the base pair images t^1 and t^2 and the required L8 image (t^3) for the prediction dates, the ESTARFM blending algorithm produced in total eight synthetic images ($L8_S$), covering the whole study site. Fig. 3.6 shows the comparison between the cross-check image pairs, consisting of original RE and $L8_S$ at similar dates, with the linear regression residuals shown spatially. The residual values in the two images are positive in areas of the Tugai forest (cross-check$_1$: $\mu = .009$; cross-check$_2$: $\mu = .002$), indicating a slight NDVI overestimation. The cotton field in the north-western corner of the study area
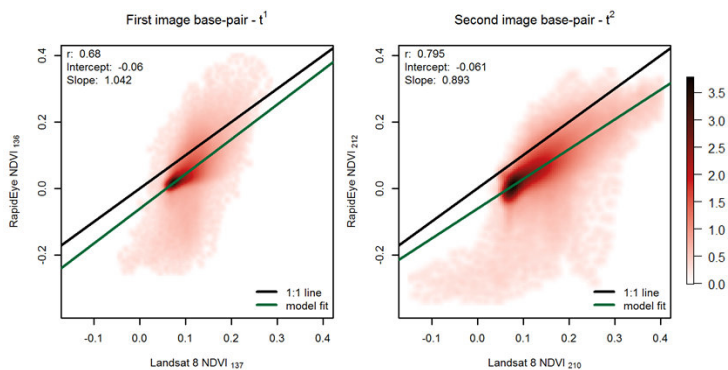
Fig. 3.5: Per pixel comparison between the two base pair images of Landsat 8 (x-axis) and RapidEye (y-axis). Correlation was highest between the second image base pair (right image) from August 27/30 and weaker for the first image base pair (left image) recorded on May 31 and June 2.

has negative residuals in May (cross-check$_1$: μ = -.004), which shows NDVI underestimation when the field is bare and vegetation coverage is very low. During the transition when bare soil is replaced by the green cotton plants,
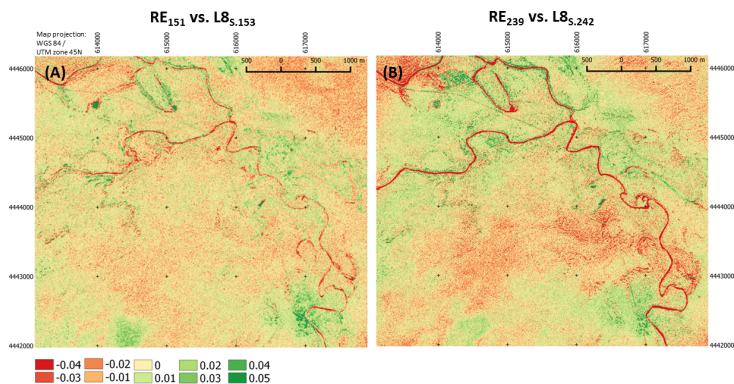
Fig. 3.6: Spatial distribution of the linear regression residuals of the two cross-check image pairs RE$_{151}$ vs. L8$_{S.153}$ (A — cross-check$_1$) and RE$_{239}$ vs. L8$_{S.242}$ (B — cross-check$_2$).

the residuals are positive and NDVI values are overestimated (cross-check$_2$: μ = .01). The relatively homogeneous area of the desert sand has a rather speckled appearance with very low negative residuals and a low spatial variance (cross-check$_1$: μ = -.001; cross-check$_2$: μ = .001).

Table 3 shows the goodness-of-fit measures for five land cover classes (percent area distribution: asphalt 0.14%, cotton field 0.60%, desert sand 84.15%, Tugai forest 13.81% and Tarim river 1.3%) for two cross-check image pairs to evaluate the performance of the ESTARFM blending algorithm. The Pearson correlation coefficient, r, is for both cross-check image pairs very strong (cross-check$_1$: r = .919; cross-check$_2$: r = .878). The highest correlation values were observed for the Tugai forest class in early summer (cross-check$_1$: r = .844) between the leaf growth phase and the crown closure and during peak summer (cross-check$_2$: r = .756). The desert sand has relatively stable correlation numbers (cross-check$_1$: r = .788; cross-check$_2$: r = .726) and a homogeneously low NDVI throughout the year. The level of statistical significance (p-value) of the correlation coefficient is for all land use classes < .0001, which means that there is a statistically significant relationship between the observed vs. predicted image values: RE vs. L8$_S$ NDVI values.

 The regression equation for Tugai forest was: cross-check$_1$: RE = .031 + 0.729 L8$_S$, cross-check$_2$: RE = .02 + 0.664 L8$_S$. In general, all land use classes had a small intercept; however, the intercept for the entire image increases slightly from β_0 = 0.005 (cross-check$_1$) in late spring to β_0 = 0.006 (cross-check$_2$) in summer. The slopes of the linear regression lines range from β_1 = 0.896 in late spring to β_1 = 0.767 in summer. This indicates an overestimation of NDVI values in areas of low vegetation cover. In areas with denser vegetation, the values conform better to the RE values, and less differences between the observed and predicted image values occur. See Fig. 3.7 for the respective Tugai forest class scatterplots.

Table 3.3: Selected error indices and correlation measures, partitioned into five land use / land cover classes, for the two model validation image pairs.

Sensor type & image pair	Land cover class	r	Intercept (β_0)	Slope (β_1)	RMSE	NRMSE
cross-check$_1$ RE$_{151}$ vs. L8$_{S.153}$	Asphalt	0.736	0.014	0.797	0.026	92.9
	Cotton field	0.409	0.007	0.422	0.011	107.4
	Desert sand	0.788	0.008	0.722	0.012	68.9
	Tugai forest	0.844	0.031	0.729	0.021	62.6
	Tarim river	0.487	-0.041	0.280	0.055	160.7
	Total	**0.919**	**0.005**	**0.896**	**0.015**	**41.0**
cross-check$_2$ RE$_{239}$ vs. L8$_{S.242}$	Asphalt	0.456	-0.003	0.332	0.029	136.6
	Cotton field	0.742	0.053	0.651	0.071	137.5
	Desert sand	0.726	0.008	0.681	0.017	76.8
	Tugai forest	0.756	0.020	0.664	0.035	90.5
	Tarim river	0.342	-0.077	0.316	0.089	148.8
	Total	**0.878**	**0.006**	**0.767**	**0.024**	**55.2**

Perfect Fit: r: -1/1; intercept: 0; slope: 1; RMSE: 0.

3.3.2 Forest disturbance & recovery analysis

From the 131 reference trees were 46% severely defoliated and 34% either with light or moderate defoliation. 20% were not affected by *A. cinerarius*.
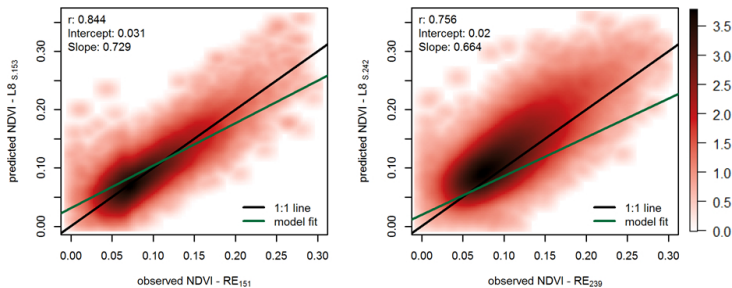
Fig. 3.7: Forest class scatter plots of observed and ESTARFM predicted NDVI values from the two cross-check image pairs (black line = 1:1 base line, green line = linear regression model).

Fig. 3.8 Forest disturbance and forest recovery accuracies for RE and L8$_S$ images compared to only RE. Images dates are labelled with the corresponding DOY.
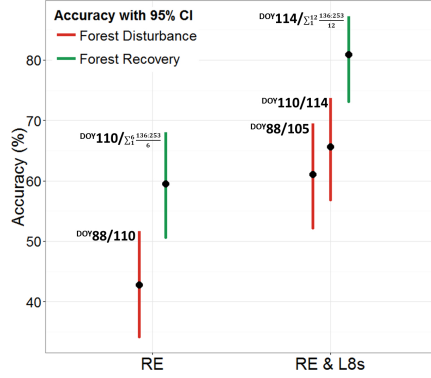
The overall mapping accuracy results show that the added L8$_S$ images, generated using ESTARFM, had a significant positive impact on all analysed stages (see Fig. 3.8). Forest disturbance accuracies increased from 42.8% using RE (D$_{RE.88/110}$) to 61.1 & 65.7% (D$_{RE.88/L8.S.105}$ & D$_{RE.110/L8.S.114}$) with additional L8$_S$ imagery, while forest recovery accuracies improved from 59.5% to 80.9%. Images which were taken at the end of the insect disturbance period performed best during the disturbance detection (D$_{RE.110/L8.S.114}$).

Considering the individual disturbance classes, we conclude that PA's for trees with no or light defoliation (class C_0 & C_1) were consistently high. Trees with moderate or severe defoliation (classes C_2 and C_3) were not sufficiently recognized using only RE during spring defoliation (see Table 3.4). When L8$_S$ was added to the analysis, PA's for vital trees (C_0) remained high while PA's increased for moderate defoliated trees (C_2: 52.4% and 61.9%) and severely defoliated trees (C_3: 54.9% and 64.8%), respectively. PA's for the recovery phase improved for refoliated trees (C_0) from 64.8% with only RE to 100% with additional L8$_S$. In-situ reference data didn't include trees with class C_3 in the recovery (refoliation) phase.

Overall, it can be noted that the process of defoliation and recovery is highly dynamic in time and space within the given time window (see Fig. S4). The disturbance analysis with RE underestimated the insect infestation significantly (see Fig. A.3) and mainly confused heavily defoliated trees (> 50%)

Table 3.4: Map accuracies for forest disturbance and recovery detection with RE and added L8$_S$ imagery.

Imagery	Period	Accuracy [%]							
		C_0		C_1		C_2		C_3	
		UA	PA	UA	PA	UA	PA	UA	PA
RE	$D_{RE.88/110}$	20.2	100.0	70.8	77.3	75.0	14.3	100.0	26.8
	$R_{RE.110/136:253}$	90.7*	64.8*	29.4	41.7	0	0	0	
RE & L8$_S$	$D_{RE.88/L8.S.105}$	70.8	100	44.9	59.1	47.8	52.4	70.9	54.9
	$D_{RE.110/L8.S.114}$	43.8	82.4	54.2	59.1	48.1	61.9	95.8	64.8
	$R_{RE.110/RE\_L8.S.136:253}$	80.8*	100*	100	4.2		0		

* Recovery

with trees of class C_0 (< 0% defoliation) (see Table A.2). According to the disturbance map with the highest accuracy during the insect defoliation period ($D_{RE.110/L8.S.114}$ with 65.7%), we would mistakenly conclude that approximately 58% of the area was not affected by *A. cinerarius* (see Figure A.4). According to these results, 11% of the area was either moderately or severely defoliated (see Table A.1). Generally, the combined information of RE & L8$_S$ shows a higher variability and more distinct spatial pattern of the disturbance (see Figure A.4). In comparison with the in-situ reference data, we can conclude that we underestimated the insect infestation.

3.4 Discussion

3.4.1 Accuracy of ESTARFM simulation

The pixel-based comparison between the observed RE and L8$_S$ NDVI values for the two cross-check image pairs revealed differing but satisfactory correlations for the five land use / land cover classes. Correlation coefficients between observed and predicted images were higher when the prediction

date was closer to the observation date (cross-check$_1$ = 3 days, cross-check$_2$ = 4 days) because temporal variability is lower.

Correlation values for the Tugai forest class were high in both cross-check image pairs. The results suggest that ESTARFM is able to predict reflectance values for patches of tree clusters and sparse isolated trees sufficiently. Our results are comparable to accuracies reported by other studies mapping forest areas with Landsat/MODIS ($0.728 < r^2 < 0.888$)(Walker et al., 2012); $0.50 < r^2 < 0.84$ (Hilker et al., 2009b). The Likewise, fairly constant correlation values for the asphalt and desert sand classes were achieved. Both classes have no phenological changes and can be characterized as spatially and temporally stable. However, the elongated shape of the asphalt road resulted in more mixed (heterogeneous) low resolution pixels; therefore, the ESTARFM achieved lower correlation values compared to the homogenous desert sand.

It was also apparent that pixels covering the Tarim River had the lowest correlation results for every validation image, except for cotton in spring (cross-check$_1$). One reason might be the temporal variation of the surface water levels due to current water conveyance practices (Rumbaur et al., 2015). Changing surface water levels influence local soil moisture dynamics and vary the spectral contrast and spatial variation in the endmember fractions of coarse-resolution pixels (Landsat 8). One possible modification of the fusion model would be to adapt the fixed search window size during the ESTARFM process according to the current heterogeneity or complexity level of the land surface being processed. The search window size could be dynamically adapted depending on the amount of neighboring pixels with the same land cover type as the central pixel in process.

3.4.2 Forest disturbance & recovery analysis

The key finding of our analysis is that forest disturbance caused by *A. cinerarius* can be detected more accurately with the aid of synthetically derived images compared to the original data set. Forest disturbance mapping based solely on RapidEye ($D_{RE.88/110}$) underestimated the actual defoliation.

We reason that the defoliation underestimation between RE_{88} and RE_{110} is caused by a number of factors. The main reason can be attributed to the sensor off-nadir view angles, which are considerably higher for both scenes (RE_{88} $-16.25°$ and RE_{110} $13.77°$) compared to the average off-nadir view angle ($6.89°$) of the remaining RE scenes. The high view angles affect the canopy reflectance geometry and decrease the NDVI values as viewing angle increases (Skidmore, 2003). As a consequence, in $D_{RE.88/110}$ was the defoliation considerably underestimated.

Another reason is due to the low sun elevation during the overflight, especially for the image scene RE_{88} ($53.41°$; $65.11°$ of the remaining RE scenes). L8 and RE are sun synchronous sensors and pass the study area at effectively the same local time, with changing sun elevation and azimuth angles during the year. A declining sun elevation angle causes variation in the illumination condition under which imagery is obtained. A low sun elevation reduces the solar radiation intensity, weakening the recorded signal and consequently lowering the signal to noise ratio (SNR). A lower SNR reduces the reflectance and thus the NDVI.

A less obvious but quite important factor is the broad spectral bandwidth of the RE sensor, especially for the NIR band (see Figure A.2). The broad range of wavelengths in the NIR band produces a stronger signal but decreases the spectral resolution, and is therefore less sensitive to reflectance variability.

The accuracy of forest disturbance detection was strongly reliant on the temporal resolution of the imagery. During the reported insect outbreak, which lasted in our case study three to four weeks, there were three images recorded (one RE image and two Landsat 8 images). The most accurate map was generated based on the images from RapidEye [DOY 110] and Landsat 8 Synthetic [DOY 114]. During this period, temporally interweaved and spatially unevenly distributed processes such as bud break, leaf unfolding and growth occur. Efficient discrimination between trees foliating and trees being defoliated remains a challenging task (see Fig. 3.9).

Nevertheless, the suitable timing of the images (here 5 days) allowed for the reliable detection of foliation differences and hence insect infestation. Due to the rare circumstance that our study area is located in an overlapped
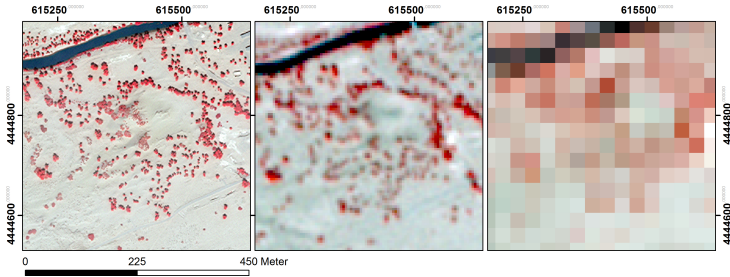
Fig. 3.9: Worldview2 (left; bands 7-5-3), RapidEye (middle; bands 5-3-2) and Landsat 8 (right; bands 5-4-3) image chips showing a typical spatial distribution for the Tugai forest along a floodplain area with patches of dense Euphrates Poplar (*P. euphratica*) clusters along the riverbanks and sparse isolated trees towards the desert. The spatial resolution of Landsat 8 (30 m) does not support distinction between single trees and tree clusters nor their defoliation state.

area of two Landsat paths we had a higher image frequency to work with. Areas with less Landsat observations could incorporate data from Sentinel-2A which offers similar spectral/spatial coverage as Landsat 8. With the launch of Sentinel-2B (planned for mid-2016) the two platforms will provide a 5-day global land coverage. Although our work is based on RapidEye and Landsat, the ESTARFM approach would be also applicable to Sentinel-2 data.

Our analysis generated high goodness-of-fit values with plausible forest disturbance & recovery occurrences. However, several shortcoming need to be discussed. First, we did not account specifically for the scaling effect between the two used sensors and its possible impact of non-linearity on the relationship between fractional ground cover and NDVI. Because ESTARFM uses a sophisticated identification of pixel similarity within neighbourhoods (Zhu et al., 2010) to define locally influenced linear relationships between RE and L8, which results in non-linear spatial functions between both sensors at the entire image scale (Emelyanova et al., 2013). Second, we used relative radiometric normalized ToA reflectance values instead of surface reflectance values. Our main reason for doing so was the absence of atmospheric property records at the time of image acquisition, which are required to perform a sound atmospheric correction. The introduced uncertainty may

have influenced the disturbance & recovery detection accuracy. Finally, we cannot fully discriminate between the effects of a) the image quality (e.g. off-nadir angles of RE), b) the scaling effect between RE and Landsat, and c) the influence of an additional synthetic Landsat 8 scene with a more suitable acquisition date for the forest disturbance detection. Despite the mentioned uncertainty, it is not feasible to repeat the disturbance analysis including solely original Landsat scenes due to the insufficient spatial resolution for the detection of sparse forest vegetation. Hence, we cannot judge about or compare the data quality of the sensor types. It is still very obvious that the disturbance maps including Landsat show a more distinct disturbance pattern, which reflects the outbreak and dispersion of the calamity much better than RapidEye alone (see maps in Figure A.4).

The results of this study are comparable to the results obtained in previous forest disturbance mapping studies relying solely on RapidEye images (Adelabu et al., 2014; Marx, 2010). For example, Adelabu et al. (2014) differentiated three defoliation classes using RapidEye-generated NDVI layers (un-defoliated, partly defoliated and refoliated trees after severe defoliation) and reported an overall classification accuracy of 61% (random forest, RF) and 51% (support vector machine, SVM). In this study, we achieved similar results with RapidEye (42.8 / 59.5%). However, Adelabu et al. (2014) increased their classification accuracies (84% RF, 93% SVM) when the Red-Edge NDVI was used instead of NDVI. We increased our accuracy by fusing and using better-suited data pairs (DOY [110/114]; see . Fig. 3.8).

It is also worth noting that, due to the random sampling design followed in this study, we had no validation samples which covered the severely defoliated trees in the recovery phase. Thus, we suggest that studies in similar ecosystems consider following the double sampling approach for stratification, especially for the monitoring of sparse tree populations (Lam et al., 2011).

3.5 Conclusions & outlook

This case study focused on determining whether the addition of synthetic images derived from a RapidEye / Landsat 8 configuration would increase

the accuracy of forest disturbance detection compared to the original data set. Furthermore, we analysed which pre- and post-infestation image pairs were the most important for differentiating defoliation severity.

Our results suggest: (a) *A. cinerarius* infestation severity can be classified with RapidEye at a moderate accuracy. However, accuracy increased by $\sim 23\%$, reaching $\sim 66\%$ when ESTARFM generated synthetic images were added. (b) Defoliation severity accuracies decreased with increasing disturbance levels. (c) Images taken at the end of the first foliation and at the peak of the caterpillars feeding were superior to images acquired at an earlier stage; this stage was found to be particularly important for differentiating between the light, moderate and severe defoliation classes. Although it is evident that the L8$_S$ images retain a high spatial level of detail, further research should focus on a scale comparison between 30 m and 5 m resolution.

We recommend that the timing of data acquisition should consider host tree phenology and the peak manifestation of insect damage, especially for image tasking requests. It is the timing, rather than the number of images, which has the most influence on accuracy in this context. The use of commercial data products (e.g. RapidEye) in particular requires conscientious acquisition planning, in order to reduce the high cost of data purchase. The presented work shows the first data fusion application between RapidEye and Landsat 8 and presents a useful alternative to the regular Landsat / MODIS configuration.

3.6 Acknowledgments

Chapter 4
Revealing trend shift dynamics after ecological water deliveries using Landsat TM/ETM+ time series in a semi-arid forest ecosystem

With Michael Förster & Birgit Kleinschmit

Abstract

The ecological restoration of degraded riparian Tugay forests in north-western China is critical for combating desertification in this region. Local stakeholders and restoration managers are particularly interested in understanding the response of these forests to recent restoration efforts and increasing knowledge regarding their resilience.

Satellite derived time series make it possible to detect abrupt changes in long term vegetation trends. These trend shifts may give decision makers some hindsight regarding the effect of change. In this research, we applied the Breaks for Additive Seasonal and Trend (BFAST) algorithm to a 14 year Landsat TM/ETM+ time series. We a) analyzed the occurrence of trend shifts, b) researched similarities and differences between vegetation types in their response effects, and c) examined longitudinal/transverse linkages to known river discharges.

Our results show increased vegetation growth during water delivery periods. In turn, the absent of discharge had a substantial effect on the prevalence of trend shifts. Vegetation showed resilience after a drought year, with above average growth in subsequent years. The reaction of the vegetation was more pronounced in the upper and middle zones, and less apparent in the lower section of the river catchment area. This longitudinal effect can be explained by the fact that at least five out of the twelve water deliveries did not reach the lower section. Transverse impacts showed a delayed growth response of approximately six month in areas adjacent to the river channel. The time lag increased by around one month for every 500 m from the river towards the desert.

4.1 Introduction

Dryland degradation is one of the most pressing environmental issues of the 21st century (Ravi et al., 2010), and is driven by various factors including changes in climatic conditions and increasing human activities (UNCED, 1992). A frequent cause for degradation processes is intensive agricultural cultivation at the upper reaches of a river, which causes severe water scarcity in the lower reaches. Ecosystems which face chronic disturbances shift into a less desirable state and lose the capacity for renewal and reorganization, causing the resilience of the ecosystems to fade (Elmqvist et al., 2003). Together with grazing pressure (Säumel et al., 2011), this can result in a complete loss of vegetation cover (Zeleke and Hurni, 2001) and subsequently in desertification.

Since the early 1960s, large areas in central Asia and western China have experienced the consequences of cropland mismanagement combined with precipitation deficits (Piao et al., 2010; Yaning et al., 2009; Zhang et al., 2010). The floodplains along the large endorheic rivers, such as the Amu-Darya, the Syr-Darya or the Tarim, are representative examples (Novikova et al., 1998; Kotlyakov, 1991; Xu et al., 2004) of large-scale water withdrawals for crop irrigation and soil degradation due to pervasive salinity problems in irrigated land (Dregne, 2002).

These repercussions have also affected the natural riparian Tugay forests. These forests are threatened by flow regime changes linked to river regulation (Nilsson and Berggren, 2000) and increasing human demands for water (Richter et al., 1997). The continuously falling groundwater table and decreasing soil moisture levels prevent tree and shrub roots from connecting to the necessary water resources. The consequence is large-scale Tugay forest disturbance with alarming rates of forest degradation. The situation causes concern due to the particular importance of the local riparian forests, which serve as a green belt between the adjoining deserts. Therefore, understanding the response of riparian Tugay forests to these stressors and further generalizing knowledge regarding their resilience is of particular interest for local residents, forest and restoration managers.

Within local plant communities each individual species develops its own

specific survival strategy. The two local key species *Populus euphratica* and *Tamarix ramosissima* for example, try to keep roots in permanent contact with the groundwater and therefore maintain a high level of transpiration (Gries et al., 2003; Thomas et al., 2006; Thevs, 2007). Prolonged droughts and severe groundwater shifts force *P. euphratica* to repress transpiration and avoid desiccation by growth inhibition. This survival strategy is demonstrated through the dieback phenomenon, where the top of the tree crown shows damage (Liu et al., 2011) as a consequence of height suppression and leaf abandonment (Monda et al., 2008; Westermann et al., 2008). *P. euphratica* responds to rising groundwater levels with the establishment of a secondary crown (Aishan et al., 2015), vigorous shoot growth (Liphschitz and Waisel, 1970) and increasing leaf area (Wang et al., 2007). *T. ramosissima*, a subdominant species in this riparian ecosystem, exhibits different adaptive traits in response to hydrological fluctuations. It shows the ability to increase root elongation when groundwater declines below the initial rooting depth (Li et al., 2013a), leaving less carbon available for above-ground growth (Gries et al., 2003). These plant specific morphological adaptations are synchronized with river flow patterns and provide benefits when disturbances, e.g. reduced water availability, occur (Li et al., 2013a). As a consequence, there are fluctuations in the above-ground net primary productivity, which have been accurately measured by means of litter mass (Niu et al., 2015), diameter (Westermann et al., 2008; Li et al., 2006; Qisen et al., 2010; Yu et al., 2012) or basal area (Gries et al., 2003), and volume increments (Ni et al., 2001; Gries et al., 2005). However, these field methods may not be suitable for long term and large scale forest monitoring due to low sample coverage and infrequent survey opportunities. Remote sensing methods are therefore particularly suited for monitoring the growth of floodplain forest ecosystems in response to changes in water availability, especially for areas in western China with large regions prone to desertification and limited access to many remote areas (Yang et al., 2005). For this purpose, the Landsat satellites have proven to be of unmatched value, providing a free (Woodcock et al., 2008) window into the past (Wulder et al., 2012). Landsat data are well suited for capturing pre- and post-disturbance features (Assal et al., 2016). The information is frequently collected (16 day revisit cycle) in spectral bands spanning the visible and infrared wavelengths, and has a pixel size (30 m) which is capable of resolving most disturbance types (e.g., natural and anthropogenic) occurring in forest systems (Townshend and Justice, 1988; Wulder et al., 2008; Schroeder et al., 2011). Further-

more, the opening of the Landsat data archive has encouraged the use of long-term time series, as well as the development of change detection algorithms applicable to forest ecosystems (e.g. Vegetation Change Tracker (VCT) (Huang et al., 2010), (Landsat-based detection of Trends in Disturbance and Recovery (LandTrendr) (Kennedy et al., 2010), Continuous Change Detection and Classification (CCDC) (Zhu and Woodcock, 2014)), Breaks For Additive Season and Trend (BFAST) (Verbesselt et al., 2010a,b) and BFAST-Monitor (Verbesselt et al., 2012). BFAST-Monitor has been successfully used to track post-disturbance dynamics in tropical forests with Landsat time series (DeVries et al., 2015a,b; Dutrieux et al., 2015). However, the need of a historically stable forest profile limits the applicability to areas where such monitoring period is steady over time. Due to historically unstable temporal profiles for our study area, we chose BFAST over the BFAST-Monitor approach.

Vegetation species react with different strategies to shortages in resources such as nutrients and water, as well as to disturbances such as fires or infestations. While some species tend to die quickly but re-establish soon after (ruderal strategy), others endure limitations (stress tolerant strategy) (Grime, 1977). Although the above named methods are applied frequently to disturbances for different vegetation types, there is limited knowledge on how to relate the different trends and breaks to ecological effects.

Many studies have been published showing a predominantly positive vegetation response in the lower reaches of the Tarim river, using field measurements (Tao et al., 2008; Xu et al., 2007; Chen et al., 2008; Ling et al., 2015), and also including remote sensing data (Kong et al., 2009; Sun et al., 2011; Liu et al., 2014; Gärtner et al., 2014). These publications vary by sensors used, the related spatial scale and the applied methods. In this study, they shall only be used as a basis for a general statement regarding the ecosystem's current state. While there have been numerous studies on forest disturbance mapping with BFAST using medium (e.g. MODIS) (Wen and Saintilan, 2015; Watts and Laffan, 2014; Darmawan and Sofan, 2014) or coarse (e.g. AVHRR) (Schucknecht et al., 2013) resolution sensors, the authors know of only one other study by (DeVries et al., 2016) who applied the BFAST algorithm on high resolution data, such as Landsat. The overall aim of this study was to assess the usefulness of the BFAST algorithm in conjunction with a 16 day Landsat Normalized Difference Vegetation In-

dex (NDVI) (Tucker, 1979) time series, for mapping long term trends and abrupt changes between 2000-2013 for different species of riparian Tugay vegetation in a semi-arid region in western China. An important focus of the presented research was to gain knowledge and increase understanding of the effects of an ongoing ecological restoration program (e.g. river regulations via hydrological engineering and additional river discharge), on the responses of different Tugay vegetation types and on observed vegetation trend shifts. In particular, we addressed three main research questions:

1. Can Tugay vegetation trend shifts be observed in a Landsat time series between 2000 and 2013 and if so, are there different longitudinal (along the river) or transverse (across the river) linkages in the landscape mosaic?
2. Which similarities and differences do the analyzed Tugay vegetation types show in their response effects?
3. Is there a response in vegetation to river discharges and if yes, how strong is the relation between the amount of discharge and the response?

4.2 Material and methods

4.2.1 Study area

The Tarim river is the longest inland river in China with a length of about 1,321 km (Chen et al., 2006a). Our study focused on the last 321 km, which is the most degraded section as a consequence of water mismanagement beginning in the late seventies. This section marks the river's lower reaches between the Daxihaizi   reservoir in Yuli county and the Tetema end lake in Ruoqiang county (chinese: Taitema, Uyghur: Titama) (see Fig. 4.1). The river course is divided into two streams from the Daxihaizi reservoir onward; the western branch is called old Tarim river while the eastern branch is called Chiwinkol river. The two branches are roughly parallel and merge near Arghan forest station (N 40°8.72′ E 88°21.26′).

The region is characterized by an extreme arid climate with mean annual precipitation < 50 mm and potential evaporation > 2,000 mm per year (Chen et al., 2015). The region is dominated by open sandy areas with dense clus-

ters of young *Populus euphratica* along the riverbanks, and sparse isolated
withered trees towards the desert. The most common shrub species in the
area belong to the *Tamarix* genus (*Tamarix ramosissima*, *Tamarix hispida*
and *Tamarix leptostachys*). Predominant herbs and grasses are *Karelina
caspica*, *Alhagi sparsifolia* and *Phragmites australis*. All species of Tugay
vegetation are drought-enduring and salt-tolerant (Zhou et al., 2010); how-
ever, as phreatophytes their roots need continuous contact to groundwater
for their growth and survival (Thevs et al., 2012). The groundwater regime
is regulated by Tarim river discharge which drives the region's ecology, in-
cluding vegetation responses to soil water availability. No major silvicultural
management operations have been carried out and the forest can be consid-
ered to be in a semi-natural state.

In recent years, construction measures have been carried out to protect river
banks and control the course of the river bed. Numerous retaining weirs con-
trol the inflow and outflow in strategic river stretches while breakthroughs
shorten meanders and increase the speed of stream flow (Zhu et al., 2006).

4.2.2 Datasets

4.2.2.1 Satellite data

We obtained all available images recorded by the Thematic Mapper (TM)
sensor on board Landsat 5 and Enhanced Thematic Mapper Plus (ETM+)
sensor on board the Landsat 7 satellite, covering the two adjacent paths
141/142 on row 32 (see Figure 4.1). Because there were no image acqui-
sitions on our study area for 1999, we restricted our time series to all data
after and including 2000 until 2013. The Landsat images were downloaded
from the USGS Earth Explorer portal, provided as a surface reflectance data
product generated from the Landsat Ecosystem Disturbance Adaptive Pro-
cessing System (LEDAPS) (Masek et al., 2006). We excluded unwanted dis-
turbances such as clouds, cloud shadows and snow using the supplied Fmask
layers (Zhu and Woodcock, 2012). Data gaps, due to Scan Line Corrector
failures in ETM+ scenes, were filled for scenes recorded after May 31, 2003
(Scaramuzza et al., 2004). From a visual assessment, we did not find any re-
markable geolocation errors in the Landsat image stack. On average we had
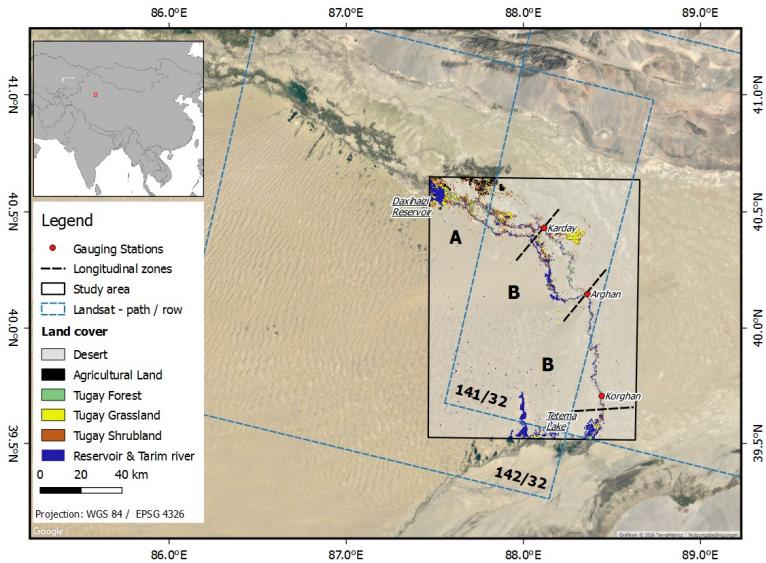
Fig. 4.1: Location of the study area at the lower reaches of the Tarim river Basin between the Daxihaizi reservoir and the Tetema end lake in Xinjiang Uyghur Autonomous Region in Peoples Republic of China. Longitudinal zones correspond to areas influenced by the same discharge event: from Daxihaizi reservoir until Karday gauging station (zone A), from Karday until the Arghan gauging station (zone B) and from Arghan gauging station until the Tetema end lake (zone C).

275 Landsat TM/ETM+ images available (see figure A.5). We computed the NDVI from the pre-processed surface reflectance layers. This vegetation index is sensitive to chlorophyll and sufficiently stable to permit meaningful comparisons of seasonal and inter-annual changes in vegetation growth and activity (Huete et al., 2002).

4.2.2.2 Hydrological data

Discharge data were provided by the Tarim Basin Water Resources Commission. Discharge water volumes were collected at four gauging stations. The Karday station is located on the Chiwinkol river while Arghan, Korghan

Table 4.1: Ecological water deliveries to the lower reaches of the Tarim river. Discharges with an asterisk (*) were interrupted, the duration is specified for the actual days with discharge. Data are provided by Tarim Basin Water Resources Commission.

Delivery	Start date (dd.mm.yy)	End date (dd.mm.yy)	Duration (days)	Discharge volume ($x\ 10^7\ m^3$)	Section reached
1st	14.05.2000	13.07.2000	61	9.9	Karday
2nd	03.11.2000	14.02.2001	104	22.7	Arghan
3rd *	01.04.2001	17.11.2001	97 & 67	18.4 & 19.8	Arghan
4th	20.07.2002	10.11.2002	114	29.3	Tetema
5th *	03.03.2003	07.11.2003	131 & 56	25 & 9	Tetema
6th *	22.04.2004	15.09.2004	64 & 46	10.2 & 23	Tetema
7th *	18.04.2005	02.11.2005	32 & 65	5.2 & 23	Tetema
8th	25.09.2006	30.11.2006	66	23.3	Korghan
9th	15.10.2007	21.11.2007	38	5.0	Karday
10th	12.05.2009	20.06.2009	39	6.0	Karday
11th	25.06.2010	11.11.2010	139	36.4	Tetema
12th *	07.01.2011	23.11.2011	19 & 151	2.8 & 13.6	Tetema

and Tetema are on the main Tarim river (see Figure 4.1). Between May 2000 and November 2011 there were twelve water diversions with a total volume of about 28 x 10^8 m^3 (Aishan et al., 2015). Because of the quick infiltration into the dry river bed, no more then seven water deliveries reached the Tetema end lake (accounting for ≈ 68 % of the total water volume) (Abaydulla et al., 2012). In 2008 the upstream inflow into the Daxihaizi reservoir decreased dramatically, with the consequence that no water could be delivered to the lower reaches during this year (Sun et al., 2011). Details of the delivery timing, duration, volume and gauging stations reached are provided in table 4.1.

4.2.2.3 Land cover data

In order to restrict the time series analysis to Tugay vegetation areas only, we developed a land cover map by means of a Random Forest classifier (Breiman, 2001). The land cover classification was performed in Google[TM] Earth Engine, a geospatial data analysis platform designed for parallel processing using Google's computing infrastructure (Padarian et al., 2015). The

input parameters used for the Random Forest classifier include the number of decision trees to create per class (300), the number of variables per split ($\sqrt{45}$), minimum size of a terminal node (1), out-of-bag mode (true) and the fraction of input to bag per tree (0.5). The classification was based on a Landsat 8 image stack consisting of five nearly cloud free (<1 %) images from April 24, 2013; April 11, 2014; May 29, 2014; September 18, 2014; and September 5, 2015. Forty-five predictor variables were drawn from the spectral data of the first seven bands (band 1 - band 7) plus an additionally created NDVI (Rouse Jr et al., 1974) and SAVI (Huete, 1988) layer for each image. Reference data were obtained for 502 samples from Digital Globe via Google Earth, covering all six land cover classes (see Table A.3). Reference data were split randomly into training (60%) and validation (40%) sets prior to the classification. To assess the accuracy of the classification, we used a confusion matrix (Stehman, 1997).

4.2.3 Change type analysis

4.2.3.1 NDVI time series preparation

To perform a breakpoint and trend detection analysis with the BFAST algorithm, it was necessary to transform the non-equidistant Landsat TM/ETM+ NDVI data into an equidistant time series format. The following steps assume a NDVI value y_i recorded at non-equidistant dates x_i.

First step we created a synthetic daily regular time series object, including each measured NDVI value (y_i) at the recorded time (x_i). Second, we replaced missing values between measured NDVI records with the robust periodic seasonal trend decomposition using Loess (STL) (Cleveland et al., 1990). The STL starts after the point number k of the time series, and is processing until the point number N-k, where N is the number of observed points of the time series. Finally, we aggregated the daily NDVI time series to a mean 16-day time interval product with a frequency of 23 observations per year.

#### 4.2.3.2 Breakpoint detection

The magnitude and timing of abrupt changes (breakpoints) in the 16-day
Landsat time series were detected using the BFAST algorithm, as imple-
mented in the *bfast* package version 1.5.8 (Verbesselt et al., 2010a,b) in R,
version 3.2.0 (R Core Team, 2015). BFAST is able to decompose time series
into trend, seasonal, and remainder components, as well as detect and char-
acterize abrupt changes within the trend and seasonal components. BFAST
allows trend changes to be recognized within the time series (assuming that
non-linearity can be approximated) by fitting a piecewise linear model (Ho-
rion et al., 2016).

In our research, BFAST was run using the *dummy* seasonal model, which
was implemented in Verbesselt et al. (2010b) to fit the seasonal component
and find trend changes (rather than temporal shifts) in land surface phenol-
ogy (Watts and Laffan, 2014). The BFAST algorithm has an important con-
trol parameter (*h-parameter*) which determines the potential number of de-
tectable breaks within the time series. The parameter defines the minimum
period to fit a piecewise linear segment in the trend model (Verbesselt et al.,
2010a). Ideally, *h* is small enough to detect significant change but still large
enough to get reasonable estimates from the linear regression model in each
segment. We fixed the *h*-parameter at $^1/_6$, allowing the minimal segment size
between detected breaks to be $2^1/_4$ years (equivalent to $\sim$52 observations).
The maximum number of breaks was set to five while the critical signifi-
cance level (α) for the detection of breakpoints was set to 0.05.

4.2.3.3 Trend shift derivation

For each pixel, the BFAST method returned: (a) intercepts and slopes of
trend segments, (b) magnitude and timing of breakpoints and (c) the confi-
dence intervals of the breakpoint timing. Features of (a) and (b) were com-
bined and further analyzed in order to characterize the timing and frequency
of changes. According to the main trend and break characteristics we divided
each time series into one out of six trend shift classes, which are labeled as
follows: *Monotonic Increase*, *Monotonic Decrease*, *Interrupted Trend Type
1 (Interrupted TT1)*, *Interrupted Trend Type 2 (Interrupted TT2)*, *Reversed*

Trend Type 1 (*Reversed TT1*) and *Reversed Trend Type 2* (*Reversed TT2*) (see Fig. 4.2).
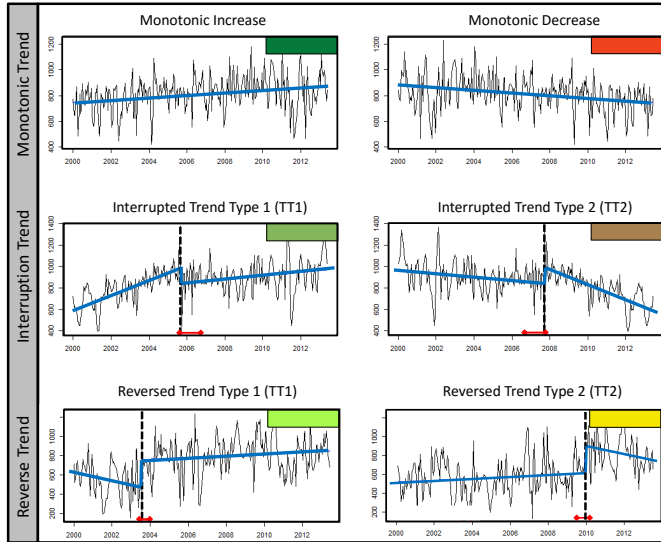
Fig. 4.2: The classification scheme used here has been adapted from de Jong et al. (2013) and Horion et al. (2016). **Top**: Time series with a significant (p < 0.05) *Monotonic Increase* (left) or *Monotonic Decrease* (right) without breakpoints. **Middle**: Time series with a trend interrupted by a breakpoint. Trend segments have the same direction. Positive trends before and after the breakpoint are labelled as *Type1*, while negative trends before and after the break are classified as *Type 2*. **Bottom:** Time series with a *Reversed Trend* marked by a breakpoint. Trend segments have opposite directions. Decreasing trend followed by an increasing trend is labelled as *Type 1*, while a positive trend followed by a negative trend is logged as *Type 2*.

4.2.4 Analysis of the BFAST algorithm

BFAST's ability to recognize disturbance and recovery events was evaluated by comparing the timing of trend shifts with the timing of known river

discharges. River discharge is the main driving force of the Tugay vegetation life-cycle. The rise of the groundwater level is highly dependent on the plant's distance to the river channel. The same applies to the reaction of the vegetation on the improved groundwater situation. The response of the vegetation might be delayed by several months. A sudden positive change in the NDVI time series is regarded as vegetation response to river discharge, triggered by the plant's groundwater access. In terms of the six established trend shift classes, we associated the positive response with *Interrupted & Reversed TT1*. In periods with permanently absent water discharges, we expected a decreasing NDVI trend and thus *Interrupted & Reversed TT2*. The exact timing of water transfers was unknown for each pixel location. Therefore, we related the start dates of each river discharge with the time of the trend shift events, within a transverse corridor of 1.5 km to the river. For each vegetation and trend shift type we produced a response curve (smoothed generalized additive model - GAM) showing the temporal delay in relation to the river distance.

4.3 Results

4.3.1 Land cover classification

There was a total of about 1.25 million ha land classified, 93.74% of which is desert land. The forest area covers about the same area as grassland (12,400 ha, or 1%), while shrubland covers around 24,600 ha, or 2%. Agriculture and water surfaces share around 2%.

Our land cover classification meets the criteria of Anderson (1976), who suggests a minimum level of interpretation accuracy of at least 85% and about equal interpretation accuracies among classes. We achieved an overall accuracy of 86.13% (kappa accuracy: 82.11%), and none of the classes had a producer or user accuracy below 77%. The results of the land cover classification are displayed in a map in figure A.6. The confusion matrix for the validation of the Random Forest classification is listed in table A.4, and includes also training accuracies (see Table A.5).

Table 4.2: Proportions of statistically significant changes of vegetated areas.

| Land cover	Total area *ha*	sign. change *ha (%)*
Shubland	24,590	23,174 (94.2)
Forest	12,494	11,963 (95.7)
Grassland	12,434	9,144 (74.0)
Sum	**49,518**	**44,281 (89.4)**

4.3.2 Tugay vegetation dynamics

Approximately 89.4% of the total natural vegetated area (49,518 ha) experienced significant (p < 0.05) vegetation productivity changes between 2000 and 2013 (see table 4.2). Around 10.6% (5,237 ha) of the vegetated area remained in a stable steady-state condition. The most frequently revealed break rate in our study was for a single breakpoint (see Table 4.3). The number of breakpoints decreased nearly linearly with each rank position. However, we found in 12% ($\approx$ 2,800 ha) of shrubland no evidence of abrupt NDVI changes. Thus, among the three vegetation classes, shrubland had the largest area without obvious alterations in the above ground biomass since 2000. Grassland had the largest share of its area with three breakpoints (21.2%, with shrubland and forest $\approx$ 13%). Within the whole study area, only 0.6 ha had five breakpoints detected. We observed on average (incl. area with no breaks) 1.55 breakpoints per pixel (shrubland $\bar{x}$ = 1.47; forest $\bar{x}$ = 1.57; grassland $\bar{x}$ = 1.74).

In figure 4.3 (a complete map is provided in figure A.7) we can observe a general trend of fewer breakpoints in areas further away from the main river channel. Vegetated domains in the immediate vicinity of flooding areas and meandering river sections show more breaks. However, areas with little or no discharge near river side arms show less dynamic vegetation responses as well. Locations with four or more breaks were found mainly on submerged sites, stocked mostly with *Phragmites australis*.

Table 4.3: Area ratio for the number of breakpoints in the main land cover classes. Weighted percentage ratio (%) was analyzed for each land cover class individually. Average breakpoint number per pixel is 1.55.

Nbr of breaks	Shrubland		Forest		Grassland		Total	
	Area (ha)	% of class	Area (ha)	% of class	Area (ha)	% of class	Area (ha)	% of class
None	2,791.3	12.0	950.9	7.9	578.5	6.3	4,320.7	9.8
One	9,910.0	42.8	5,027.2	42.0	3,510.6	38.4	18,447.8	41.7
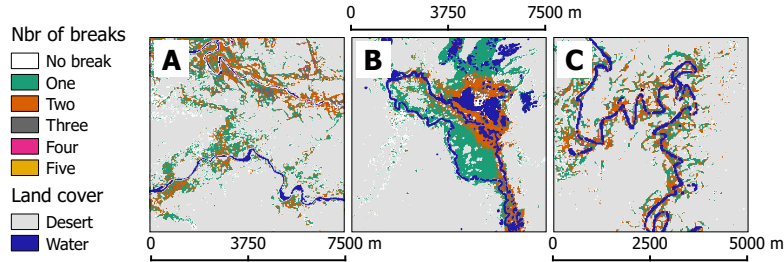
Fig. 4.3: Nr. of breaks. Inlet location is shown in figure 4.4.

4.3.3 Trend shift succession

After transforming each trend and break succession into a corresponding trend shift class (see Fig. 4.2), we note from the relative frequency percentages in table 4.4 that single (one trend shift) positive trends prevail. The *Interrupted TT1* was the most dominant for all vegetation land cover classes. In fact, an increasing trend with a setback was detected in more than $1/3$ of the forest, shrubland and grassland area. *Monotonic Increase* without an abrupt

interrupting event was observed in approximately 10.9% of the shrubland area. Single decreasing trends, either monotonic or interrupted, were found in less than 2% of the vegetated area. However, *Monotonic Trends* were predominantly observed near cut-off meanders or dry side arms further towards the desert (see figure 4.4). The median slope of the monotonic trend is 0.012 NDVI units, or 26% (shrubland 0.0115; forest 0.0163 and grassland 0.0097 NDVI units).

We observed succession dynamics with two consecutive trend shifts in about 14,685 ha, or $^1/_3$ of the study area. Combining the trend shift successions into sequences revealed eight possible combinations (the middle section in Table 4.4 shows seven sequences with area percentage ≥ 1). The possible combination of sequences was limited, since the second trend segment of the first trend shift must have the same direction as the first trend segment of the following trend shift. In the supplementary material figure A.9 lists the eight possible sequence combinations and their distribution over time.

Two successive *Interrupted TT1* occurrences were the most prevalent in shrubland (11.8%) and forest (15.6%) areas. We regard this as a continuing positive NDVI trend, which was interrupted by two significant setbacks more than two and a half years apart. It is important to note that more than 16.1% of the grassland area experienced a sequence of two *Reversed Trends*, starting with type 2 followed by type 1. This indicates a positive trend at the beginning of the study period, followed by a disturbance event and an associated reversed trend (now negative). This was followed by a second break, where the trend switched again into a positive direction at the end of the study period. All species in the grassland class (mainly *A. sparsifolia*, *K. caspica* and *Phragmites*) are perennial and herbaceous, with their aboveground components dying back in winter. Discharge events with a short duration and/or low volume may not be sufficient to stimulate physiological responses. Thus, grassland species do not grow new entire shoots each season, resulting in a temporally negative trend. However, the sequence has a positive final trend segment, indicating a grassland recovery in the most recent years.

Approximately 6,356 ha had a sequence of three trend shifts in the NDVI time series. The most significant, with respect to its area, was the sequence *Reversed TT2 - Interrupted TT2 - Reversed TT1* (in total 2,285 ha). This se-

Table 4.4: Area (ha) and relative frequency (%) of up to three trend shift sequences are shown. Relative frequencies were derived from the total number of times each trend shift was observed divided by the total area of the land cover class in which observations were made. The trend shift color schema match class labels in fig. 4.2. Trend shifts with < 1% are not shown.

Trend Shift	Shrubland (ha)	(%)	Forest (ha)	(%)	Grassland (ha)	(%)
Monotonic Trends						
●	2531	**10.9**	871	7.3	498	5.4
●	260	1.1	80	.7	80	.9
Interruption Trends						
●	7990	**34.5**	4044	**33.8**	3145	**34.4**
●	463	2.0	187	1.6	88	1.0
Reverse Trends						
●	468	2.0	256	2.1	95	1.0
●	988	4.3	540	4.5	183	2.0
Succession of Two Trend Shifts						
● → ●	214	.9	71	.6	88	1.0
● → ●	350	1.5	162	1.4	331	3.6
● → ●	2745	**11.8**	1863	**15.6**	431	4.7
● → ●	237	1.0	102	.9	59	.6
● → ●	765	3.3	424	3.5	262	2.9
● → ●	1800	7.8	931	7.8	1470	**16.1**
● → ●	1199	5.2	727	6.1	256	2.8
Succession of Three Trend Shifts						
● → ● → ●	192	.8	81	.7	128	1.4
● → ● → ●	239	1.0	117	1.0	77	.8
● → ● → ●	236	1.0	133	1.1	117	1.3
● → ● → ●	386	1.7	338	2.8	163	1.8
● → ● → ●	809	3.5	461	3.9	1015	**11.1**

quence was similar to the one in the previous section, with the difference that the negative period was prolonged and another *Interrupted TT2* was inserted in the middle. Grassland was the most affected by this effect (11.1%).
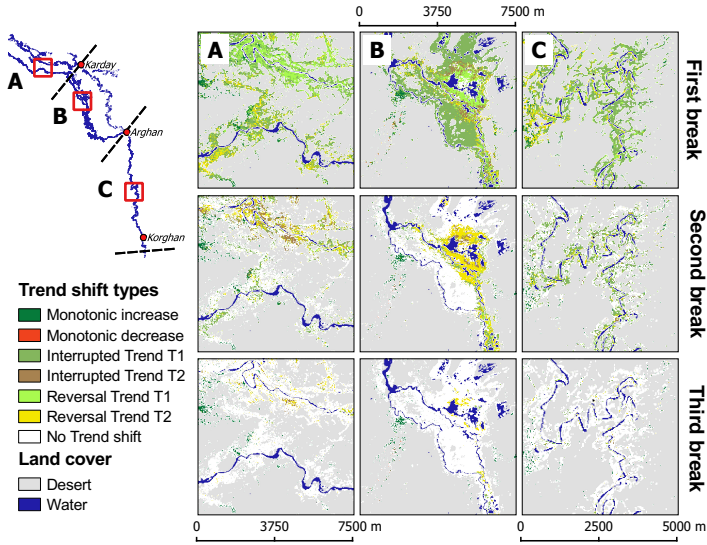
Fig. 4.4: Trend shift frequency in three close up zones.

4.3.4 Trend shift timing and longitudinal linkages

Figure 4.5 presents the temporal occurrence of single trend shifts. The prevalence is normalized by zone areas along longitudinal river sections (zone A-C) and land cover classes (% area weighted). Shrubland has the largest share of natural vegetation with a single trend shift. Shrubland areas decrease sharply from zone A (5,700 ha or 58%) towards downstream areas (685 ha or 7%). In shrubland the *Interrupted TT1* predominated, especially at the end of the time series. About 80% (*aw*) of the measured type 1 class was recorded after summer 2009 within zone A (90% in zone B). We observed the *Interrupted TT1* in the southern tip of zone C in approx. 70 ha of the shrubland after 2011, due to the shortening of a meander and associated river course amendments (N 39°37.004′ E 88°26.588′).

In forest and grassland areas, the *Interrupted TT1* class also occurred with higher frequency at the end of the time series. The most frequent occurrence
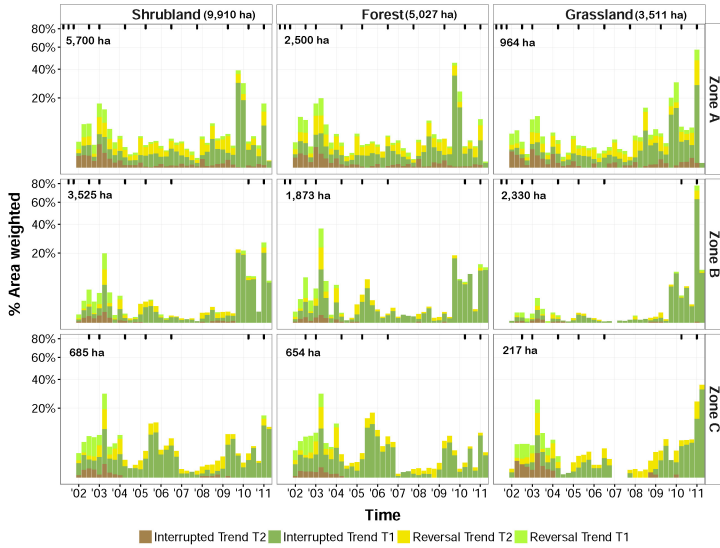
Fig. 4.5: Area weighted percentages (%) of single trend shift occurrences. Numbers are normalized by land cover class and river sections. Each facet grid sums to a total of 100%. Temporal occurrence was aggregated from the 16 day interval to a quarter of a year (3 months). Black rug points represent the water deliveries with volumes ≥ 1 M m^3.

of type 1 appeared in grassland in winter 2011 with $> 60\%$ (zone B). An example time series with the *Interrupted TT1* in summer 2010 is shown in figure 4.7 (top). *Reversed TT2*, the second most common class, appeared regularly in small quantities. *Interrupted TT2* occurred in zone A on a regular basis, in zone B & C only between spring of 2002 and spring 2004 and again very rarely between 2008 and 2009. In zone C, grassland had more area weighted percentages of *Interrupted TT2* than forest or shrubland.

Figure 4.6 presents the temporal occurrence of twofold trend shifts. About 5,500 ha of trend shift occurrences were found in winter of 2009 and spring of 2010 (and and additional 2,964 ha in spring 2011). In summer 2003, 2,319 ha of the study area had a trend shift. Notably, trend shift occurrences in zone B included approximately 60% of shrubland, 55% of forest and up to 45% in grassland. This sequence of a double *Interrupted TT1* occurred in the com-
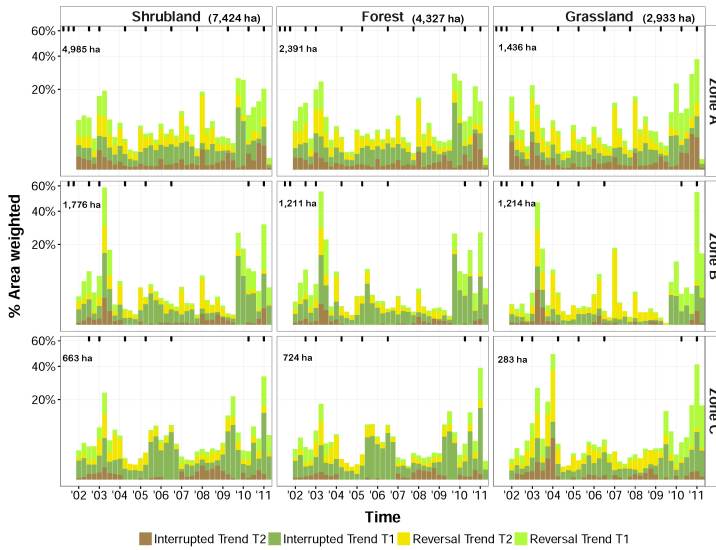
Fig. 4.6: Area weighted percentages (%) of twofold trend shift occurrences. Numbers are normalized by land cover class and river sections. Each facet grid sums to a total of 100%. Temporal occurrences were aggregated from the 16 day interval to a quarter of a year (3 months). Black rug points represent the water deliveries with volumes $\geq$ 1 M m^3.

bination 2006 and 2010 in all land use classes, with 912 ha (see figure 4.7 - middle). This sequence *Reversed TT2 - Interrupted TT2 - Reversed TT1* appeared in the combination 2004 - 2007 - 2011 in all land use classes most frequently, with 538 ha (see Figure 4.7 - bottom row).

4.3.5 Occurrence of trend shifts relative to known water deliveries

The evaluation of the BFAST algorithm was based on the comparison of the induced water discharge events versus the timing of recognized trend shifts. Because river discharge is not a specific event with immediate impacts such as fire or insect infestation, there is an expected temporal delay of vegetation
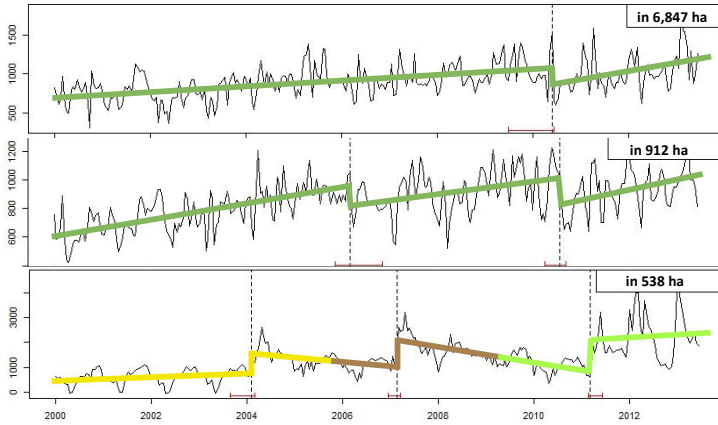
Fig. 4.7: BFAST results for the most prevalent trend shift classes in the study area. The colour coding for the trend shifts sequences is according to figure 4.2. Y axis represents NDVI while x axis represents time in the 16day Landsat time series.

response to the water delivery (Hao and Li, 2014).

The tenth (2009) water delivery had the strongest effect on the vegetation, most likely due to the complete absence of water in 2008 (Table 4.5). Approximately 28% of all detected trends shifts occurred with or after the tenth water delivery. In at least four consecutive months (6 to 9 months time lag), the vegetation corresponded with more than 5% of all trend shifts. In the drought year 2008, considerably less trend shifts were recognized. Shrubland (mainly *Tamarix*) had the biggest drought resistance with 2.1% positive (*Interrupted TT1*) trend shifts. Forest (mainly *Populus*) and grassland followed thereafter with 1.8% and 1.5%.

Water deliveries and recognized trend shifts exhibited the strongest relationship with a time delay between three and six months. In this period, more than half (in total 61%) of all identifie d trend shifts occurred. In years when water deliveries were interrupted, the vegetation response almost stopped. However, BFAST was also unable to detect a declining response in vegetation vitality. With the continuation of the water delivery delayed trend shifts

Table 4.5: Percentages (%) of all recognized trend shifts listed according to the determinant water delivery and the observed lag time (per month). Values are rounded to integers. Underlined values highlight the continuation of interrupted vegetation response due to interrupted water deliveries.

Delivery	Time Lag (*month*)												**Sum**
	0	1	2	3	4	5	6	7	8	9	10	11	
				·········· *percentages* ··········									
4th	1	1	1	1	1	1	2	1					9
5th *	1	2	2	6	2	2	1	1				_1_	18
6th *		1	1							_1_	_2_	_1_	6
7th *		1	1	1	1	1	2	1			_2_	_1_	11
8th		1	1	2	2	3	1	1					11
9th			1	4	3	1	1	1	1	1	1		13
10th				1	1	9	7	6	7	1			32
Sum	**2**	**6**	**6**	**11**	**11**	**11**	**16**	**12**	**7**	**9**	**6**	**3**	

were once again detected. This phenomenon can be observed between the fifth and seventh water transfer (underlined values in Table 4.5).

The Tarim Basin Water Resources Commission registered discharge data for 2000/2001 as well as 2011; however, at these times no breaks were detected. It is very likely that trend shifts would have been identified for these watering events if a) the Landsat time series would have started earlier and lasted longer or b) if the water deliveries would have been further away from the starting and end point of the time series. As Watts and Laffan (2014) pointed out, while the *h* parameter controls the minimum segment length between potential breaks, it also determines a minimum distance from the start and the end of the time series where breaks cannot be detected. The *h* parameter applied here was too large to allow a break recognition before the summer of 2001 and after the summer of 2011.

In addition to the general delay of vegetation response to water deliveries, table 4.5 shows a steady increase in delay times. While the response starts immediately for the first water deliveries (4th and 5th water delivery), vegetation responses of later water deliveries are strongest at month 3 to 7. This could be interpreted as a saturation effect of the vegetation, which had al-

ready responded before.

River discharge is the main driving force of the Tugay vegetation life-cycle. Water conveyance influences the groundwater depth, which decreases with increasing distance from the river (Chen et al., 2010; Hao et al., 2010). The transverse distance effect is visible in figure 4.8, especially for shrubland and forest areas. Using the example of a positive response, such as the *Interrupted TT1*, we observed an increasing time lag (1 - 1.5 months) with increasing proximity to the river (up to one kilometer). The type *Reversal TT1* shows almost no transverse effect in forest and shrubland, and a less-pronounced effect in grassland. This decreasing sporadic occurrence of grassland with increasing distance from the river causes the confidence interval to drift apart, allowing no firm statement regarding its transverse effect.
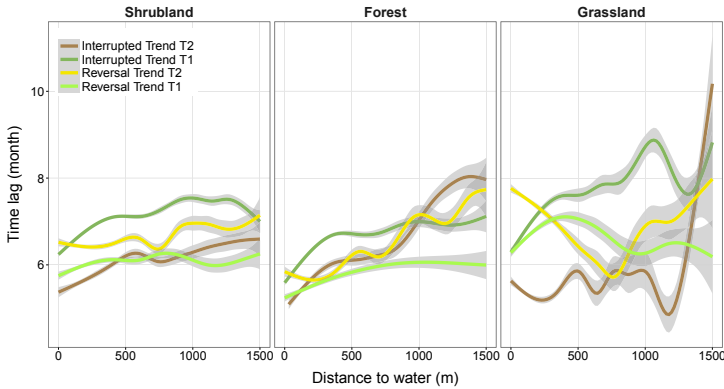
Fig. 4.8: Trend shift response curve depicting the temporal delay (y-axis) in relation to the river distance (x-axis). Response curve is based on a smoothed generalized additive model. The grayed out confidence interval had a level of 95%.

4.4 Discussion

The overall results of this study reveal trend shift dynamics after twelve years of water deliveries in a semi-arid forest ecosystem. A fourteen year Landsat TM/ETM+ time series enabled a breakpoint detection tool, such as BFAST, to detect major ecological developments for different species and reveal varying spatial pattern and trend shifts.

Our results show increased vegetation growth in times when water deliveries were conducted. In turn, the impact of absent discharge had a substantial effect on the prevalence of trend shifts. Vegetation showed resilience after a drought year (2009) with above average growth in subsequent years. The reaction of the vegetation was more pronounced in the upper and middle zones and less apparent in the lower section. This longitudinal effect can be explained by the fact that at least five out of the twelve water deliveries did not reach the lower section. Transverse impacts showed a delayed growth response ($\sim$ six month) in areas adjacent to the river channel. The time lag increased by around one month for every 500 m from the river towards the desert.

Previous change analysis studies in the area used NDVI differencing (Kong et al., 2009) and seasonally integrated NDVI (SINDVI) (Sun et al., 2011) alterations as evidence for the detected vegetation changes. Kong et al. (2009) determined an average NDVI increase by 30% to have occurred, based on bi-temporal Landsat TM images from 1999 and 2004. Sun et al. (2011) found a mean SINDVI value increase of more than 25% between 2001 and 2007 with MODIS data. Our results are in accordance with the above listed studies. For monotonic trends without breakpoints, an average NDVI increase of 26% was registered. However, our usage of all available TM/ETM+ images decreased the uncertainty in respect to reflectance variability and different acquisition characteristics.

4.4.1 Response effects of vegetation types

As expected for a highly degraded and fast changing environment, a high percentage of significant changes could be detected in all differentiated vegetation classes. However, grassland seemed to undergo more significant changes (see Table 4.3) than shrubland and forest, where around $^1/_4$ of the area experienced a series of three or four rapid responses. This can be explained by the different strategies of the vegetation types according to the competitors — stress tolerators — ruderals (CSR) scheme of Grime (1977). Although all species in this region have to be stress tolerant, there is a tendency for the grassland types, as perennial plants, to be more ruderal. Therefore, more area is quickly vegetated and then abandoned when water scarcity increases, which explains the overall high percentages of change for grassland. Shrubland and forest are clearly more stress tolerant, with a small tendency of the dominant tree species *P. euphratica* to out-compete the shrubs (*Tamarix*) with increasing water availability. This can be seen in the slightly higher numbers of the forest class for two or three breaks (see Table 4.3) of a positive trend shift (see Table 4.4) compared to shrubland. However, Hüseyinova et al. (2013) emphasize that species may change strategies within CSR space due to habitat characteristics, nutrient availability, light conditions, and intensity of disturbance factors.
In times of drought, shrubland's *Tamarix* had a greater tolerance than *P. euphratica*. In 2008, when the water transfer was absent, *Tamarix* generally had more positive trend shifts than *P. euphratica*. This suggests that *Tamarix* has a higher water use efficiency which is in accordance with Cao et al. (2011) and Xu and Li (2006).

Although heavily disturbed by other external factors, such as the cyclic defoliator *Apocheima cinerarius* (see Gärtner et al., 2016), the positive trends in biomass development for forest are still increasing, especially in the lower reaches of the Tarim. This indicates that a stable water delivery over more than one decade has had a positive cumulative effect.

Most of the established river regulations induced delayed effects on plant growth. The closure of river tributaries adversely affected hinterland grass- and shrubland vegetation. Sidearm abandonment (for example near N 40°25.327′E 88°7.951′ or N 40°29.298′ E 87°53.050′) reduced the hy-

drologic connectivity and hence the water supply between the main stream and the floodplain. We found substantially reduced growth in the immediate vicinity for two to four years after regulations were implemented.

Positive effects were prevalent near artificial river straightening and additional river-bank stabilization. These interventions counteracted any renewed meandering. Higher flow rates increased flooding frequencies especially below the straightened sections. Shrubland (*Tamarix*) in these locations benefited from the regulation, and generally showed more and consistently positive trend shifts. In contrast, the shrubland alongside the drained meander reacted significantly less often with mixed trend shift directions. At least eight retaining in-channel weirs were located along the Tarim lower reaches. No significantly increased occurrences of vegetation shifts occurred either upstream or downstream of the weirs.

4.4.2 Longitudinal and transverse trend shift effects

Longitudinal and transverse effects notably weakened the impact of the water discharge on the vegetation. All trend shifts occurred most frequently in zone A and decreased linearly towards zone C for shrubland and forest. Grassland had equally high percentages of trend shift occurrences in zone A & B ($\sim 45\%$). We found two plausible driving forces for this effect. The most obvious force is the longitudinally decreasing groundwater table (Chen et al., 2010; Xu et al., 2007; Chen et al., 2004). The longitudinally declining groundwater table causes not only reduced vegetation coverage (see Figures 4.5, 4.6), density (Chen et al., 2008) and richness (Chen et al., 2006a), but also affects the vegetation's vulnerability.

The second factor was determined to be the age structure for *P. euphratica*. Due to mostly unfavorable soil conditions, generative reproduction occurs only infrequently (Tao et al., 2008; Zhao et al., 2006) and, only in the vicinity of the river channel. The seedlings germinate and grow a deep tap root in the shelter of the shrubs, and soon over-top them. Root suckers never develop a tap root but utilize the horizontally stretching root of their parent trees (Wiehle et al., 2009). Without substantial river course changes, the forest rejuvenates only along the river (Thevs et al., 2008). The remaining

forest grows to maturity, individual trees die and no young saplings grow up to replace them. Hence, the age distribution of *P. euphratica* gallery forest increases transversely (Westermann et al., 2008). Over time, the age-related tree productivity changes and the adaptability declines towards drought events. We argue therefore that the *P. euphratica* age structure is a factor for fewer responses in the southern zone C due to its reduced vitality.

4.4.3 Occurrence of delayed trend shifts relative to known water deliveries

Our third research question was related to the intensity of the relationship between river discharge and lag in the vegetation response. We showed evidence that recorded water deliveries had a strong positive impact on the vegetation development. Evidence for this can be seen in the average increase of the NDVI between 2000 and 2013. However, when looking at the trend shifts for the detected breaks (see Table 4.5) the cumulative positive effect of the water deliveries becomes apparent. Often, the positive interrupted or reversed trends (such as *Interrupted TT1* or *Reversed TT1*) which account for most changes for all vegetation types can be explained by the absence of the upstream water delivery (as was the case in 2008 - see Table 4.1). These trends appear more frequently after such a drought period, as can be seen for the year 2009 (see Fig. 4.5 and Fig. 4.6). Liu et al. (2014) performed a post-classification change detection in the area and recorded an above average positive vegetation change in 2009 as well.

Trend shifts exhibited the strongest relationship to water deliveries with a time delay between three and six months (60%). Around 37% occurred between seven and eleven months. This seems quick compared to time lagged tree ring responses of 1-2 years for *P. euphratica* (Deng et al., 2015; Yu et al., 2012). Wang et al. (2007) noted in case of *P. euphratica*, that plant performances improved quickly with the water releases. This response was measured in increased eco-physiological parameters such as the number of leaves per current year shoot, the shoot-length and the leaf-blade size. Because the NDVI signal correlates strongly with above-ground net primary productivity (Pettorelli et al., 2005), the TM/ETM+ sensor recorded the biomass changes as they occurred.

An adequate vegetation response was not detected after every water delivery. The sixth water transfer in 2004, for example, had a volume of more than 3×10^8 m^3 meters, which was diverted during two periods in spring and late summer. The vegetation response after the delivery remained by approx. 4%, which is far below the expected reaction when compared to other water deliveries. One possible reason for this phenomena is the fact that the NDVI increased the year before (2003) more significantly than in 2004. BFAST placed the breakpoint in 2003 where it recognized a NDVI burst (16% of all breaks). However, due to the *h* factor, the next possible break at the same location is a minimum of 2.25 years after 2003, and therefore the 2004 water delivery may have missed out on proper vegetation responses. The same issue was reported by Watts and Laffan (2014) in their analysis of the semi-arid Paroo region (Australia) as well.

The size of the *h* parameter concurrently determines the period at the end of the time series in which no breaks can be detected. Further research should consider alternative algorithms such as BFAST-Monitor (Verbesselt et al., 2012) which was specifically built to overcome this limitation and allow break detection at the end of time series.

4.4.4 Landsat time series and BFAST settings

Compared to conventional ground-based surveys, satellite image time series analysis offers an effective tool for assessing the state of vegetation at a broad spatial scale (Kong et al., 2009). Landsat provided a sufficiently long and dense time series for our study area. Our analysis generated a plausible relation to known water deliveries. However, several shortcoming need to be discussed. First, we excluded flooded areas in the analysis by a simple threshold assumption. A pixel was excluded from the analysis if it was covered with water for longer than 32 days. With this decision, we excluded areas from the analysis which were affected by prolonged floods. We wanted to ensure that breakpoints occur only due to rapidly increased or reduced biomass growth and not because of floods and their associated negative NDVI values.

Second, we did not account specifically for possible land cover changes within the study period and their possible impact on the trend shift analysis. Wu and Cai (2004) observed only relatively slow and small land cover conversions in the lower reaches, while major land cover changes were found by Zhao et al. (2013), mainly in the upper or middle reaches of the Tarim River.

Finally, we tried to accommodate the ecosystem's versatility by setting the BFAST h parameter to $^1/_6$, enabling each pixel in the time series to potentially break at most five times. Early testing with similar h parameter settings produced equivalent breakpoint quantities with slightly shifted time stamps (< 2 month). This phenomenon was also observed by de Jong et al. (2011); Watts and Laffan (2013, 2014) using similarly small h parameters.

4.5 Conclusions

We revealed trend shift dynamics in vegetation responses to ecological water discharges using a fourteen year Landsat TM/ETM+ time series in a semi-arid forest ecosystem in western China. We applied the BFAST trend and breakpoint detection tool to identify major ecological break points for the three main land use classes, namely shrubland, grassland and forest.

Our results show increased vegetation growth at times when water deliveries were conducted. In turn, the impact of absent discharge had a substantial effect on the prevalence of trend shifts. Vegetation showed resilience after a drought year with above average growth in subsequent years. The reaction of the vegetation was more pronounced in the upper and middle zones and less apparent in the lower section of the river. This longitudinal effect can be explained by the fact that at least five out of the twelve water deliveries did not reach the lower section. Transverse impacts showed a delayed growth response of approximately six month in areas adjacent to the river channel. The time lag increased by around one month for every 500 m from the river towards the desert.

We demonstrated that trend shifts in vegetation index trajectories give useful insights to forest dynamics. We recommend the use of satellite image based

time series analysis in order gain further knowledge in forest disturbance and recovery dynamics, retrospectively judge past decisions and allow for better future decisions among the new generation of restoration managers.

4.6 Acknowledgments

Chapter 5
Synthesis

5.1 Summary

The importance of forests, trees outside forests and shrubs in semi-arid zones cannot be underestimated. They are essential constituents of fragile ecosystems, made more so by periodic droughts and increasing overexploitation of meagre resources (Malagnoux, 2007). However, forests, trees and shrubs play a significant role for human livelihoods in semi-arid zones because they maintain suitable conditions for agriculture, prevent soil erosion, offer watershed protection, provide habitats for animals, store carbon, and mitigate climate change (Bonan, 2008; Hartanto et al., 2003; Postel and Thompson, 2005). It is therefore very important to map and monitor for any forest change that may take place whether due to natural causes or human intervention (Jones and Vaughan, 2010). In order to mitigate the negative impacts of deforestation and disturbance of forest, tree and shrub formations, we have to enhance our understanding of the whereabouts of forest change and the causality behind the underlying processes and drivers.

In this regard, remote sensing is the most important tool for detecting and labeling of forest changes and predestined for long term forest monitoring. However, the detection of forest change is strongly associated with the level of detail desired and the manner in which images of a scene change, as a function of their spatial resolution (Woodcock and Strahler, 1987). Here, spatial resolution is used analogous to the scale of observations. Besides the issues related to spatial scales within the domain of remote sensing, major challenges remain, especially in regards to mismatches of scales when remotely sensed observations are combined with sample based field observations.

This dissertation enhances the monitoring of forest dynamics in semi-arid zones and examines the suitability of multi-sensor time series to assess forest disturbance and regrowth in the lower reaches of the Tarim river in western China. The main focus was on the applicability of very high, high and medium spatial resolution satellite imagery to improve forest disturbance and forest regrowth monitoring.

This dissertation contains three core research chapters (Chapter 2−4), each addressing one research question (see section 1.5). In the following section,

each research question is discussed and answered. Thereafter, my main conclusions are drawn and future research niches are identified.

Research question I (Chapter 2)

Can we observe individual tree crown changes with very high spatial resolution satellite imagery in semi-arid forests?

Numerous methods have been developed and tested, especially in urban areas, to observe with very high spatial resolution satellite images individual tree crown changes (Ardila et al., 2012a,b; van der Sande, 2010). However, studies of tree crown changes in semi-arid Central Asia or western China are absent. Possible reasons are a) difficulties in providing historical field measured tree crown validation data, and b) the relatively high purchase price for very high spatial resolution imagery make large or frequent acquisitions unlikely. A typical archived (previously acquired) scene will cost at least $20 km^{-1} with a minimum purchase of 25 km^2 [1].

In chapter 2, I described a region growing approach in order to identify individual *P. euphratica* trees, delineate their tree crown areas and quantify tree crown diameter changes between QB (2005) and WV2 (2011) data. Results were compared to 59 field measured reference trees.

We successfully observed individual tree crown changes with VHSR satellite imagery. The applied OBIA approach proved to be applicable in QB and WV2 scenes of a semi-arid riparian forest producing moderate results. The findings confirmed a positive tree crown growth and suggest a crown diameter increase of 1.14 m, on average. Crown diameters from manually digitized crowns corresponded better with field measurements than automatically extracted crowns (Table 2.4).

These findings underline the importance of field validation data. The exclusive use of manually digitized data for validation would have significantly overestimated the actual tree crown growth. The results additionally

---

[1] Digital Globe Imagery FAQ

showed that higher spatial resolution images provided more accurate results for tree crown change detection. Error measures for WV2 results (0.5 m pan-sharpened) were lower than for QB (0.6 m pan-sharpened).

The availability of satellite imagery with VHSR and acceptable quality, in terms of view angles, cloud cover and phenological condition, drive the feasibility of change detection studies. Because of an ongoing gap (from 2006 onwards) in VHSR observations for my study site, I had to accommodate direct tasking of WV2 image collection in order to close the gap and conduct the study. Given the new data availability, the presented analysis is essentially confined to a bi-temporal change detection with a six-year time interval, which is eventually adequate to reliably detect canopy change (Coppin and Bauer, 1995).

Research question II (Chapter 3)

Can a multi-sensor data fusion time-series improve forest disturbance detection in semi-arid forests and which factors are most important?

Forest disturbance caused by insect infestation has numerous environmental impacts, including the elevated risk to reduced resistance towards other stressors (e.g. drought, fungi). The riparian Tugay forest along the lower reaches of the Tarim river experiences an annual disturbance by the defoliator moth *Apocheima cinerarius* which feeds on 80-90% of the *P. euphratica* leaves (see section 3.2.2). Depending on the infestation severity and the level of degradation the majority of trees refoliate and thus recover to their pre-disturbance state.

In chapter 3, I examined whether a series of fused RapidEye and Landsat 8 data can be used to detect forest disturbance and recovery with increased accuracy in comparison to the original RapidEye time series. To start with, the applied ESTARFM generated synthetic images at the spatial resolution of RapidEye and the additional temporal resolution of Landsat 8 (Table 3.1). Thereafter, defoliation and refoliation were mapped pixelwise based on relative NDVI difference calculations (Equation 3.1), at first only with Rapid-Eye, after that using all observations within the time series. The accuracy

of the disturbance severity classes was assessed against ground reference information in form of field notes and 131 individual tree photos, highlighting again the importance of in-situ data.

The study showed forest disturbance mapping, based solely on RapidEye, underestimated the actual defoliation. Insect infestation severities were classified only at a moderate accuracy (Section 3.4.2). However, I identified the considerably higher off-nadir view angles and low sun elevations as main factor for the lower performances.

Overall mapping accuracies showed that the added data fusion images had a significant positive impact on all analysed stages. Forest disturbance detection, with added synthetic scenes, improved by ∼23% when compared to the original data set (Figure 3.8). The most important factor for the accuracy increase is the timing, rather than the number of images involved in the analysis. Images which were recorded at the end of the insect disturbance period, at the peak of the caterpillars feeding, performed best during the disturbance detection. This stage was found particularly important for differentiating between light, moderate and severe defoliation classes. Knowing that observation timing is the key factor for forest disturbance monitoring is a valuable asset, especially for image tasking requests. In order to lower the costs of potential multiple tasking requests demands extra detailed image acquisition planning, especially for commercial data products like RapidEye. Considerations should balance the cost against the need for timeliness, the width of the collection window and the level of required image quality (e.g. cloud cover or tilt angle constraints).

Fine scale forest disturbance mapping in semi-arid riparian Tugay forests demands high, or very high (see Chapter 2), spatial resolution imagery. The sole use of Landsat 8 *Operational Land Imager* (OLI) sensor, with its 30 m medium spatial resolution, does not provide the spatial detail for distinct patterns and object discrimination (Arnett et al., 2015). But, the sensor is very useful for data fusion applications due to two essential properties; a) the low spatial fusion ratio of 1:6 (5 m RapidEye to 30 m Landsat) and b) because of its high temporal resolution. The Landsat 8 satellite images the entire Earth every 16 days in an 8-day offset from Landsat 7. The data collected are available for download, free of charge, within 24 hours of reception. ESTARFM also functions with Landsat 7, and gives therefore high flexibility towards a

possible *near real time* forest disturbance mapping as new observations of either of the two sensors become available.

Overall, the presented work showed the first data fusion application between RapidEye and Landsat 8 and exhibited therefore a useful alternative to the regular Landsat/MODIS configuration.

Research question III (Chapter 4)

What were the rates and spatial patterns of Tugay vegetation trend shifts in the lower reaches of the Tarim river since 2000?

Since the early 1960's experienced the lower reaches of the Tarim river the consequences of cropland mismanagement in combination with precipitation deficits. The natural riparian Tugay forest degraded due to flow regime changes linked to river regulations, dam constructions and increasing human demands for water.

In the year 2000 established the Chinese government a EWCP with regular controlled floodings to mimic the natural flood regime. The official aim was, to recharge groundwater tables up to a level where the floodplain ecosystem can revitalize and the Tugay forest ecosystem can be restored. The ecological restoration of the degraded forest is critical for combating desertification in this region. Locals and restoration managers are particularly interested in understanding the response of these forest to recent restoration efforts and increasing knowledge regarding their resilience.

In chapter 4, I used a 14 year Landsat TM/ETM+ NDVI time series to apply the BFAST algorithm. The BFAST algorithm is capable to detect and characterize abrupt changes within the trend component of the time series, also known as *trend shifts* (see Figure 4.2). I mapped the distribution of forest, shrub- and grassland classes and assessed the rates and spatial patterns of trend shifts since 2000.

Along the lower reaches of the Tarim river, between the Daxihaizi reservoir and the Tetema end lake are 12,000 ha stocked with Tugay forest, an-

other 12,400 ha are covered with Tugay grassland while 24,600 ha is Tugay shrubland. The results of the trend shift analysis clearly showed significant increased rates of forest, shrub- and grassland growth in times when water deliveries were conducted (Figures 4.5 & 4.6). Positive interrupted trends were most dominant (∼34%) in all listed vegetation land cover classes. The absent of discharge had a substantial interrupting effect on the prevalence of trend shifts. However, vegetation showed resilience after a drought year (2009), with above average growth in subsequent years. This was particularly noted in 16% of the grassland area, which recovered after a disturbing drought event.

Regarding the spatial patterns, I found more pronounced vegetation reactions in the upper and middle zones and less apparent reactions in the lower sections of the river catchment area. This longitudinal effect can be explained by the fact that at least five out of the twelve water deliveries did not reach the lower section of the Tarim river (Table 4.1). Transverse impacts showed a delayed growth response of ∼six month in areas adjacent to the river channel. The time lag increased by around one month for every 500 m from the river towards the desert.

Most of the established river regulations induced delayed effects on plant growth. The closure of river tributaries adversely affected hinterland grass- and shrubland vegetation. Sidearm abandonment reduced the hydrologic connectivity and hence the water supply between the main stream and the floodplain. I found substantially reduced growth in the immediate vicinity for two to four years after regulations were implemented. Positive effects were prevalent near artificial river straightening and additional river-bank stabilization.

The overall results of this chapter reveal positive trend shift dynamics with the implementation of the EWCP in a semi-arid forest ecosystem. A fourteen year Landsat TM/ETM+ time series enabled a breakpoint detection tool, such as BFAST, to detect major ecological developments for different species and revealed varying rates and spatial pattern of trend shifts.

Restoration managers can use my presented findings in order to evaluate whether water deliveries and river regulations have had their desired effect. Furthermore, the results can help to identify suitable new areas for further

restoration efforts. The carried out restoration measures made already great contributions to revitalize the Tugay forest along the lower reaches of the Tarim and thus slowing or even preventing further merging of the neighboring Taklamakan and Kuruk Tagh deserts.

5.2 Main conclusions and outlook

The objective of this dissertation was to analyse the usefulness of multi-sensor time series for assessing forest dynamics, based on a case study of the riparian Tugay forest ecosystem along the lower reaches of the Tarim river in western China. The main aim was to contribute towards an enhanced semi-arid forest monitoring through the implementation of a set of image analysis methods under the use of multiple optical sensors. This section highlights the main conclusions from the presented dissertation and lists overlooked or under-studied topics for additional future investigations.

5.2.1 Multi-temporal remote sensing for forest monitoring

The earth is constantly recorded by satellites, which assist to monitor the state and change of forest habitats especially over large areas. However, most scientists are involded in short to medium-term research projects where they can use the entire depth of satellite data archives, but often lack long-term field-recorded validation data. The absence of historical field recordings limits applicable analytical methods because of lacking validation options. However, Vanclay (1995) and Allen et al. (2003) noted, *long-term* field studies are especially important for validation and to detect subtle trends, so *old* plots and data should not be neglected but treasured. I was in the fortunate position to use existing forest plot data from Conradie et al. (2007), recorded in 2005. Recognising the advantage of past measurements, I repeated measurements in 2011 on the exact same trees. This led to the work in chapter 2, where I conducted, a field-validated, bi-temporal tree crown change detection analysis with VHSR imagery. The results proofed tree crown growth, indicating improved ground water situations due to the established EWCP.

The optical sensors used in this dissertation had a theoretical revisit interval of ∼1 (RapidEye) to 16 (Landsat 8) days. In practice, is the number of usable images limited because of cloud cover (Wilson and Jetz, 2016) or other factors (e.g. high off-nadir view angle). In chapter 3, I used the ESTARFM sensor fusion model to increase the frequency of synthetic high resolution spatial data (5 m). The resulting short temporal scale improved the forest disturbance detection. The dynamics in the forest were quick. Between the individual image recordings had some trees their leaves already unfold, others started to be defoliated by *A. cinerarius*. Despite the improved temporal scale of the available images, the scale was still too large to identify the mixed phases of foliation and defoliation confidently. Therefore was the temporal and spatial interweaving between foliation and defoliation in spring 2013 as main source of error identified. In this instance, would daily sensor recordings have been more suitable to improve the omnipresent temporal scaling issues. Because rapid image acquisitions are highly uneconomical, a feasible alternative would be VHSR image recordings with unmanned aerial vehicles.

Multi-temporal remote sensing is capable to monitor forest structures and processes efficiently. The study in chapter 2 assessed crown growth of tagged trees with a large temporal scale (6 years) while chapter 3 investigated short term forest disturbance which happened in a matter of weeks. The results show for most *P. euphratica* trees a positive long-term crown growth, although affected by annually recurring insect infestations. Both analysis are important in order to better understand the dynamics in the Tugay forest.

5.2.2 Sensor fusion for forest monitoring

The long-awaited new era of open-access satellite data has finally arrived (Wulder and Coops, 2014). The starting signal was given by the USGS with the opening and free accessing of the Landsat archives in 2008 (Woodcock et al., 2008). Since then, there is a steady increasing number of enhanced fusion algorithms (Section 3.1) which take advantage of these archives by

blending multi-source remotely sensed data. A prominent combination is the fusion of Landsat and MODIS data to predict daily surface reflectance at Landsat spatial resolution and MODIS temporal frequency (Zhu et al., 2010). However, I presented in chapter 4 the first ESTARFM based fusion application between RapidEye and Landsat 8. The main conclusion thereof is:

Data fusion between RapidEye and Landsat 8 significantly enhances forest disturbance and recovery analysis. Forest disturbance detection increased by $\sim 23\%$, reaching $\sim 66\%$ when ESTARFM generated synthetic images were added. In this dissertation, I showed that the most important factor for the accuracy increase is the timing, rather than the number of images involved in the analysis. Landsat 8 images recorded at the end of the insect disturbance period performed best during the disturbance detection. This stage was found particularly important for differentiating between light, moderate and severe defoliation classes.

The presented findings provide a valuable knowledge base for further research in the domain of multi-source sensor fusion. Multi-source sensor fusion options include the integration between optical sensors, Synthetic Aperture Radar or LiDAR data. The two last mentioned are discussed in detail by Joshi et al. (2016); Treuhaft et al. (2004) and Dalponte et al. (2008). The fusion of optical multi-resolution data shall be the focus here and I follow up on the successful data fusion between RapidEye and Landsat 8 (Chapter 3). Considering the research carried out in my dissertation, I encourage relevant future actions such as:

- The enduring focus on the continuity of the Landsat legacy with Landsat 9[2] and the temporally backward fusion of RapidEye with Landsat OLI, ETM+, TM and MSS sensors. The created product may enhance historical forest disturbance analysis.

- The fusion of the next smaller scale combination between e.g. WV2 (0.5 m pan-sharpened) and RapidEye (5 m) with a spatial fusion ratio of 1:10. A special feature would be the creation of a synthetic *Red-Edge* band. The synthetically generated scenes will surely add value to the development of tree degradation research.

- The fusion of WV2 (0.5 m pan-sharpened) or even WV3 (0.31 m pan-sharpened) with open-access data of the Sentinel-2 sensor (10 m or 20 m) also offer the fusion of *Red-Edge* bands and hence the creation of a Red-Edge NDVI. The Red-Edge NDVI may provide key information on vegetation states, especially with regard to tree vitality loss due to water stress.

5.2.3 Sustainable water management and prospective forest monitoring

Tarim river discharge drives the region's ecology. This relation was repeatedly confirmed in the aftermath of the established EWCP (see Section 1.3) (e.g. Chen et al., 2003; Westermann et al., 2008; Chen et al., 2006b; Zhang et al., 2005; Chen et al., 2004; Feng et al., 2001; Chen et al., 2010; Xu et al., 2007; Aishan et al., 2015).

Knowing the importance of the Tarim river discharge on the regions ecology reinforces the significance of a sustainable water management. A sustainable water management requires effective feedback mechanisms between the strategic management level of the *Tarim Basin Water Resources Commission* (TBWRC) and the operational monitoring level of the Forestry Department of Xinjiang (FDX) province. The Forestry Department — or *Ting* in Chinese (Lei, 2008) – needs to provide concrete information on the state and response of the Tugay forest to recent restoration efforts made by the TBWRC. The feedback information has to be timely and spatially explicit in order to improve upcoming decisions such as e.g. duration, volume and timing of river discharge (Table 4.1) or river regulations via hydraulic engineering.

In that regard, multi-sensor remote sensing can contribute to give valuable feedback information at differing spatial scales to both administration bodies. My main conclusions for the use of multi-sensor remote sensing to assist prospective forest monitoring in semi-arid zones are:

Remote sensing with **very high spatial resolution imagery** can deliver detailed forest inventory information (e.g. number of individual trees) with low errors of omission and commission (Section 2.3.2). It can aid forest growth assessments with data regarding individual tree crown sizes (e.g. crown diameter) and their changes, with moderate accuracies (Section 2.3.4).

Remote sensing times series with **high spatial resolution imagery** can assist in forest health surveys by providing estimates on defoliation severity classes after e.g. insect infestation. With the aid of *sensor fusion*, leading to a higher temporal resolution, forest disturbance and recovery detection is feasible with moderate to high accuracies (Section 3.3.2).

Remote sensing with **medium spatial resolution imagery** allows tracing the extent and spatial distribution of land cover classes (e.g. Tugay forest, shrub- and grassland) with a high overall accuracy (Section 4.3.1). Time series analysis of **medium spatial resolution imagery** reveals positive trend shift dynamics in Tugay vegetation with the establishment of the EWCP (Section 4.3). Comprehensive descriptions of longitudinal & transverse Tugay vegetation response effects, to known water deliveries, allow for the creation of a knowledge base regarding their resilience (Section 4.3.4 & 4.3.5). Positive and negative effects of hydraulic engineering can be derived from resulting Tugay vegetation growth dynamics.

However, a operational multi-scale forest monitoring system requires more than a collection of individual scientific findings. It requires a smart integration of *in-situ* observations and remote sensing data. *A priori* monitoring objectives shall be set, including the definition and recognition of target classes, their respective monitoring intervals and mapping units. The collection of *in-situ* data, in this sparsely populated semi-arid region, could be realized in a *double sampling for stratification* strategy as proposed by Lam et al. (2011). This sampling strategy employs stratification without requiring a priori delineation of strata.

Having said that, the collection of calibration and validation data needs a centralised organisation in order to avoid duplicate field works. Furthermore, all *in-situ* data shall be made publically available to all individuals participating in the forest monitoring efforts. The ultimate task is the timely reporting to restoration decision makers, regarding recent vegetation disturbance or regrowth changes in order to adjust pending decisions on future water deliveries or hydraulic engineering tasks.

After listing potential requirements for prospective forest monitoring, I would like to give general recommendations for future work in the field of multi-sensor time series analysis in the area around the lower reaches of the Tarim river.

- From the spatial perspective, is further research on the explicit identification of individual trees and tree clusters needed (Chapter 2). A more detailed crown segmentation could refine estimates of biomass and carbon storage. With the destruction of QuickBird[3] shrunk the set of very high spatial resolution sensors suitable for a proper detection of tree crowns. Perhaps in the long run is the use of unmanned aerial vehicles a less expensive alternative to the purchase of commercial satellite imagery. The availability of very high spatial resolution imagery from unmanned aerial vehicles greatly increases the spatial scales over which e.g. tree degradation or tree morphology patterns and processes can be studied.

- The above mentioned efforts should go hand in hand with the establishment of consistent long-term medium spatial resolution satellite image time series. Recent developments towards temporally composited mosaics such as the Web Enabled Landsat Data (WELD) project (Roy et al., 2010) or the LandsatLinkr project (Braaten, 2015), a automated system to build spectrally consistent chronologies across Landsat MSS, TM, ETM+ and OLI sensors, stimulate regional to global disturbance-recovery analysis with high thematic detail. Ideally, standard products are hierarchically structured (weekly, fortnightly, monthly, yearly) so the end user is self-determining the temporal resolution of its analyzed processes.

- Based on the experience of this thesis, I am strongly in favor to relocate time-consuming and process-intensive time series analysis to cloud

---

[3] QuickBird burned up on Jan. 27, 2015 while re-entering the atmosphere.

processing services. A prominent example is the Google Earth Engine with its planetary-scale analysis capabilities. Surely, existing and future change detection, trend and breakpoint analysis tools need to be reimplemented but this may also give smaller, less equipped research labs the opportunity to work beyond local scales. In that sense, cloud computing truly begins a *second new era* in the field of remote sensing.

Appendix A
Appendix

Appendix regarding Chapter 3

Table A.1: Area changes between the defoliation and the recovery stage. Left side: only RapidEye, right side: RE with additional L8$_S$. Data unit: hectare.

	RE			RE & L8$_S$				
	$D_{RE.88/110}$	$R_{RE.110/136;253}$	$\triangle$ **RE**	$D_{RE.88/L8.S.105}$	$D_{RE.110/L8.S.114}$	$R_{RE.110/RE\_L8.S.136;253}$	$\triangle$ **A-C**	$\triangle$ **B-C**
c_0	237.93 (85.08%)	220.35 (78.79%)	-17.58	173.41 (62.01%)	162.81 (58.22%)	252.69 (90.36%)	79.28	89.88
c_1	29.84 (10.67%)	50.81 (18.17%)	20.96	70.67 (25.27%)	86.52 (30.94%)	26.71 (9.55%)	-43.96	-59.80
c_2	7.53 (2.69%)	6.41 (2.29%)	-1.12	24.54 (8.78%)	25.25 (9.03%)	0.20 (0.07%)	-24.34	-25.05
c_3	4.36 (1.56%)	2.09 (0.75%)	-2.27	11.03 (3.94%)	5.07 (1.81%)	0.05 (0.02%)	-10.98	-5.03

[*] $T_{post.defoliation}$: No Defoliation; $T_{recovery.summer}$: Recovery

Table A.2: Confusion matrices for forest disturbance and recovery detection with RE and added L8$_S$ imagery

| | RE | | | | | | | | RE & L8$_S$ | | | | | | | | | | | |
| | $D_{RE.88/110}$ | | | | $R_{RE.110/136:253}$ | | | | $D_{RE.88/L8.S.105}$ | | | | $D_{RE.110/L8.S.114}$ | | | | $R_{RE.110/RE\_L8.S.136:253}$ | | | |
Class	C_0	C_1	C_2	C_3	C_0	C_1	C_2	C_3	C_0	C_1	C_2	C_3	C_0	C_1	C_2	C_3	C_0	C_1	C_2	C_3
C_0	**17**	5	15	47	**68**	7	0	0	**17**	1	0	6	**14**	9	1	8	**105**	23	2	0
C_1	0	**17**	3	4	23	**10**	1	0	0	**13**	2	14	3	**13**	5	3	0	**1**	0	0
C_2	0	0	**3**	1	5	1	**0**	0	0	0	**11**	12	0	0	**13**	14	0	0	**0**	0
C_3	0	0	0	**19**	9	6	1	**0**	0	8	8	**39**	0	0	2	**46**	0	0	0	**0**

C_0: No Defoliation; C_1: Light Defoliation; C_2: Moderate Defoliation; C_3: Severe Defoliation
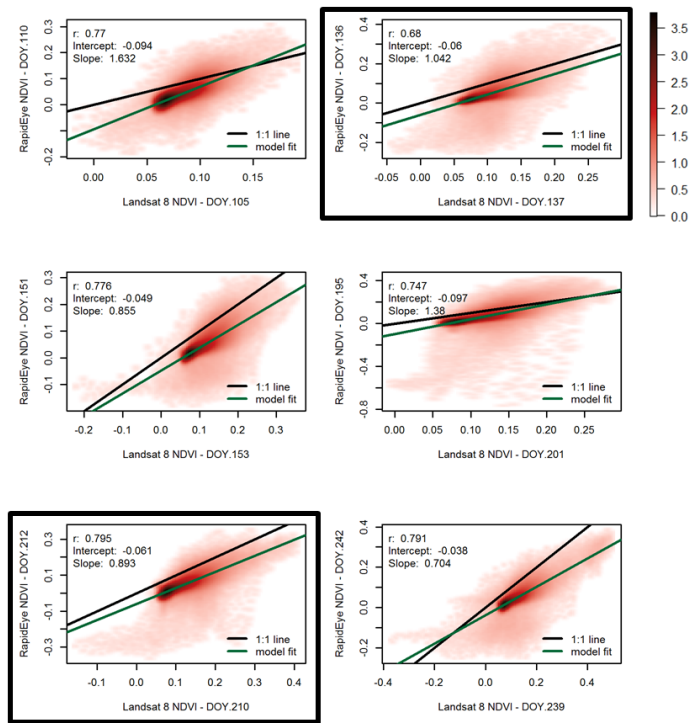
Fig. A.1: Per pixel comparison between base pair images of Landsat 8 (x-axis) and Rapid-Eye (y-axis).
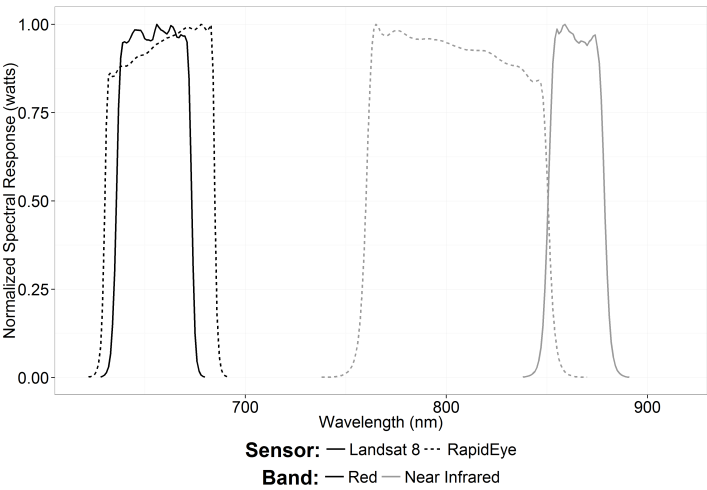
Fig. A.2: Relative spectral response functions of the red and near-infrared channels for the RapidEye and Landsat8 sensor systems used in this study.
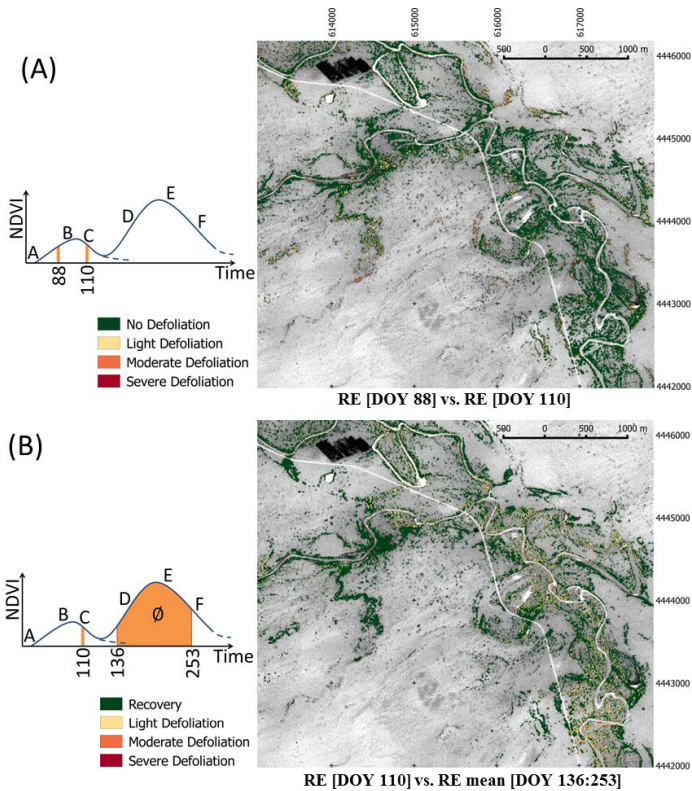
Fig. A.3: Forest Disturbance Maps classified into four classes derived from RapidEye images: No Defoliation, Nil to Light (0-30 %, Moderate (30-50 % and Severe (above 50 %) (Buxton and Maclauchlan, 2014).
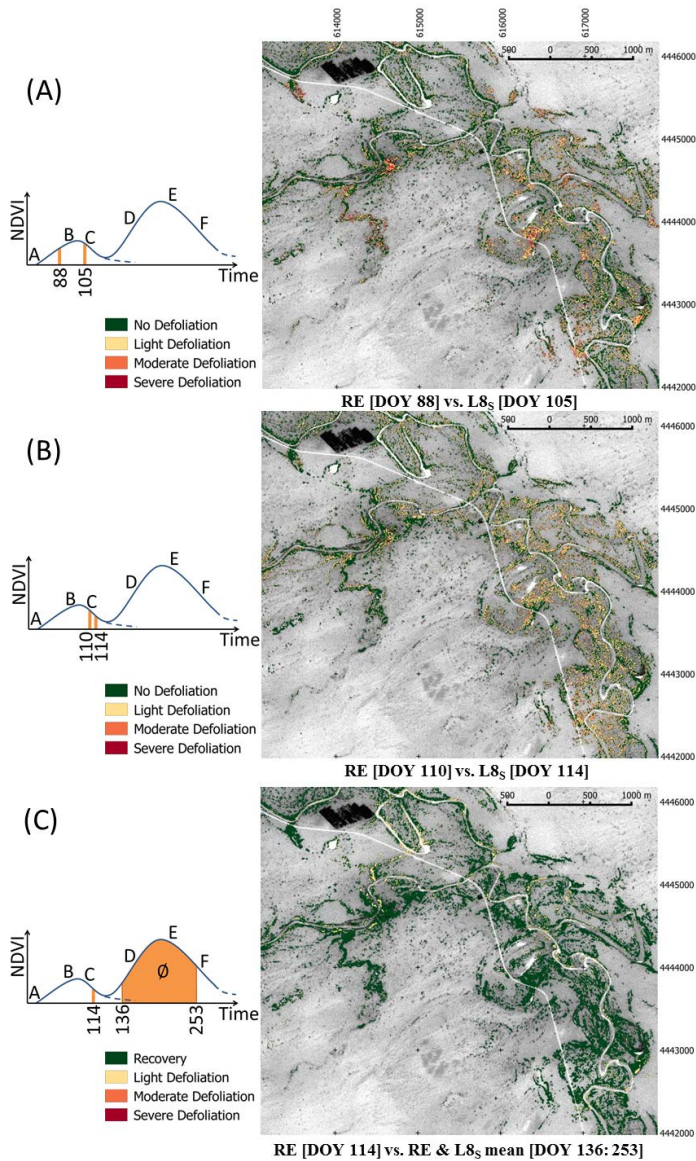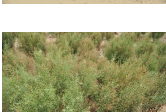
Fig. A.4: Forest Disturbance Maps classified into four classes derived from RapidEye and synthetic Landsat 8 images: No Defoliation, Nil to Light (0-30 %, Moderate (30-50 % and Severe (above 50 %) (Buxton and Maclauchlan, 2014).

Appendix regarding Chapter 4

Table A.3: Land cover class definitions are based on Anderson (1976) land-use and land-cover classification system. Plant community description was derived from (Zhang et al., 2004). There are few small urban areas and green spaces which were excluded in the classification process.

Class name	Definition in the classification procedure	
Water	Perennial reservoir and lakes, the river mainstream and side arms filled with water	
Desert, semi-desert	Desert, semi-desert, often sand dunes, vegetation coverage < 25%	
Agricultural Land	Agricultural fields mainly stocked with irrigated Cotton	
Tugay Forest	Land stocked with the predominant Euphrates poplars (*Populus euphratica*) which shows a tree-crown areal density (crown closure percentage) of 25% or more	
Tugay Shrubland	Dominated by bushes of the *Tamarix* genus together with sporadic *Lycium ruthenicum*, *Haloxylon ammodendron*, *Nitraria sibirica* and other halophyte shrubs	
Tugay Grassland	Land dominated by grasses & herbs with sparse to rich coverage. Species consist of e.g. *Phragmites australis*, *Karelina caspica* and *Alhagi sparsifolia*	

Table A.4: Validation matrix (pixel counts) of land cover classification

	Desert	Agri-culture	Shrub-land	Forest	Grass-land	Water	Sum	PA	UA
Desert	68	0	1	0	1	0	70	97.14	88.31
Agriculture	0	18	0	0	0	0	18	100.0	100.0
Shrubland	5	0	48	4	3	0	60	80.00	77.42
Forest	1	0	8	41	2	0	52	78.85	91.11
Grassland	2	0	5	0	24	0	31	77.42	80.00
Water	1	0	0	0	0	6	7	85.71	100.0
Sum	77	18	62	45	30	6	205	OA:	86.13

Table A.5: Resubstitution accuracy of land cover classification. PA: Producer Accuracy (%); UA: Users's Accuracy (%); OA: Overall Accuracy

	Desert	Agri-culture	Shrub-land	Forest	Grass-land	Water	Sum	PA	UA
Desert	130	0	1	1	0	0	132	98.48	95.59
Agriculture	0	24	1	0	1	0	26	92.31	92.31
Shrubland	3	0	61	9	3	0	76	80.26	63.54
Forest	1	0	20	37	2	0	60	61.67	72.55
Grassland	1	1	13	3	35	0	53	66.04	83.33
Water	1	1	0	1	1	10	14	71.43	100.0
Sum	136	26	96	51	42	10	297	OA:	82.27
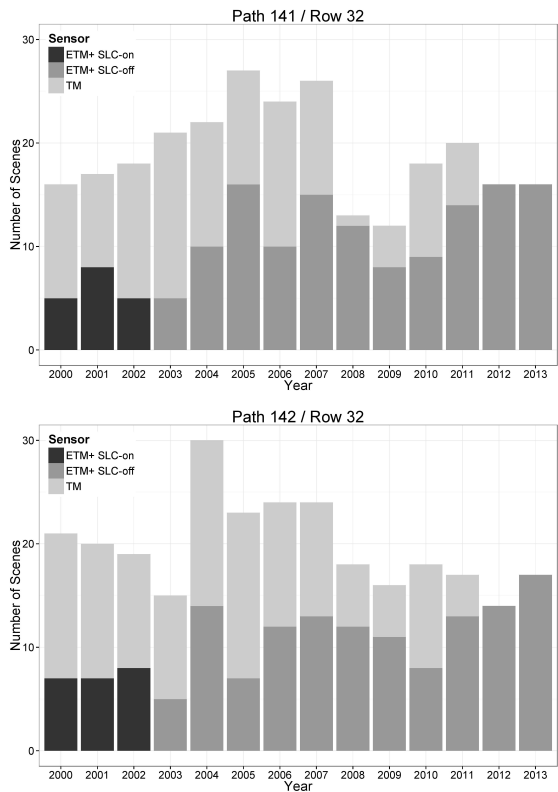
Fig. A.5: Number of available scenes for Landsat TM and ETM+ covering the study area at WRS-2 path: 141/142 and row: 32
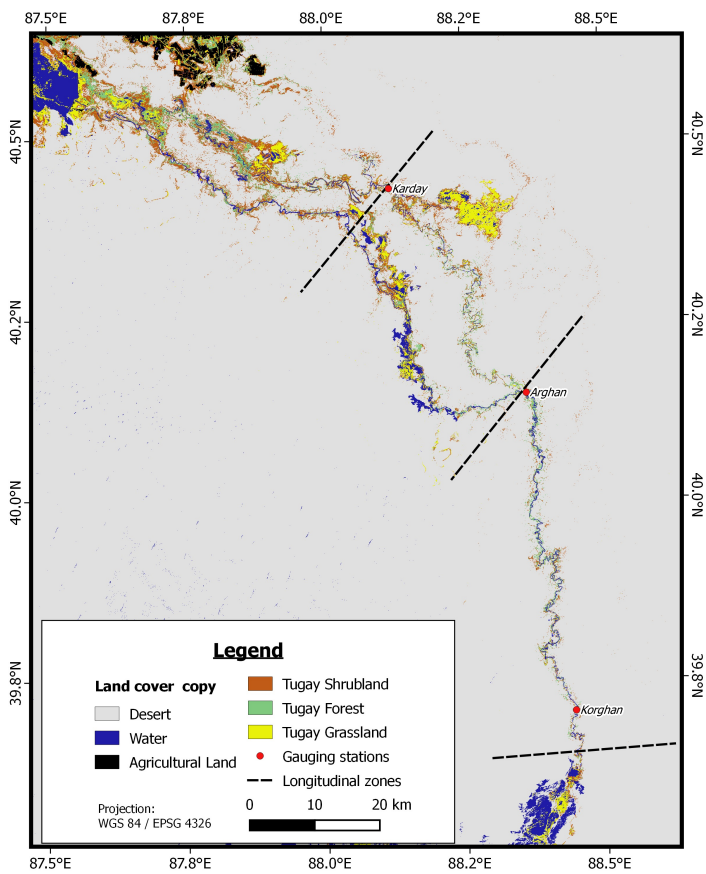
Fig. A.6: Land cover classification results showing the distribution of the predominant land cover types along the lower reaches of the Tarim river.
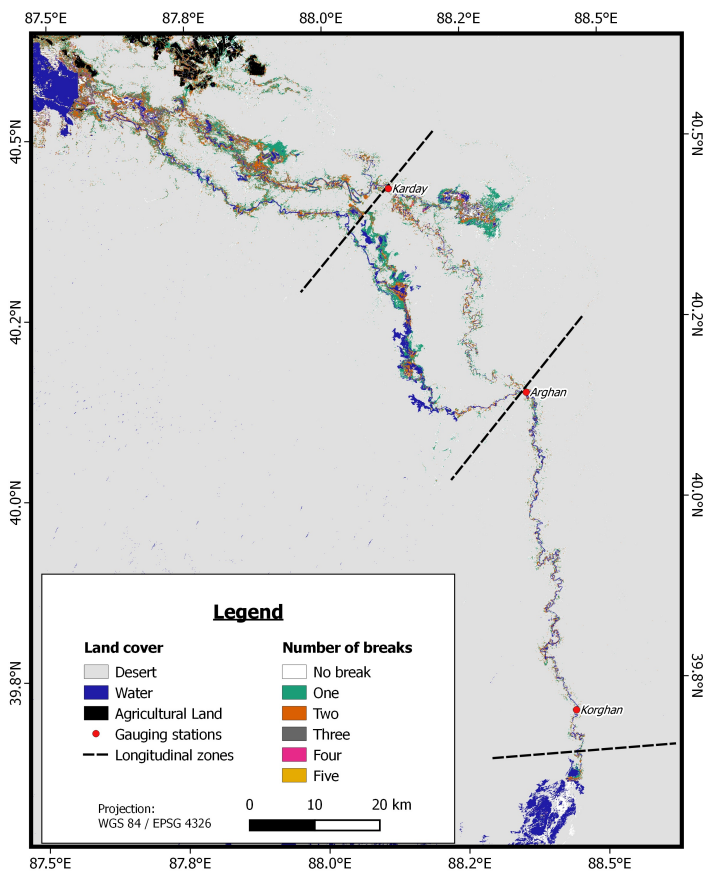
Fig. A.7: Number of detected breakpoints with BFAST algorithm for the lower reaches of the Tarim River.

Fig. A.8: Timing of trends shifts

Fig. A.9: Breakpoint trend pattern regarding the sequence between first and second breakpoint.

References

Abaydulla, A., Gui-lin, L., Kurban, A., Ablekim, A., 2012. Ecologic water transfusion in the lower reaches of the Tarim river based on CBERS/CCD image. Resources and Environment in the Yangtze Basin , S2.

Abdurahman, M., Kurban, A., Halik, U., Ablekim, A., Duan, H., 2013. Study on phenological characters of populus euphratica oliv. and its relation with the tree diameter. International Journal of Plant Research 26, 88–92.

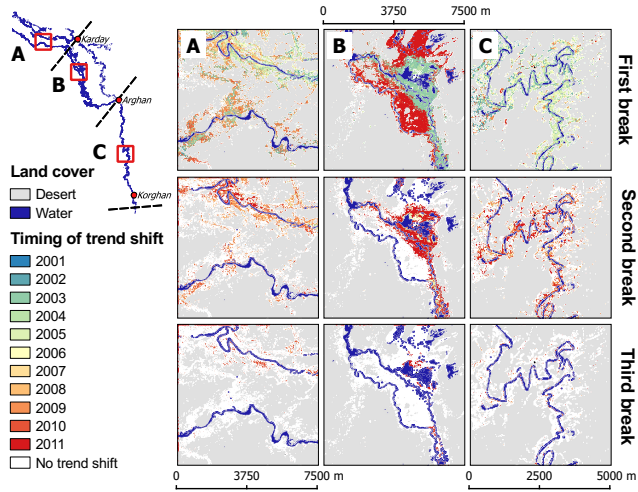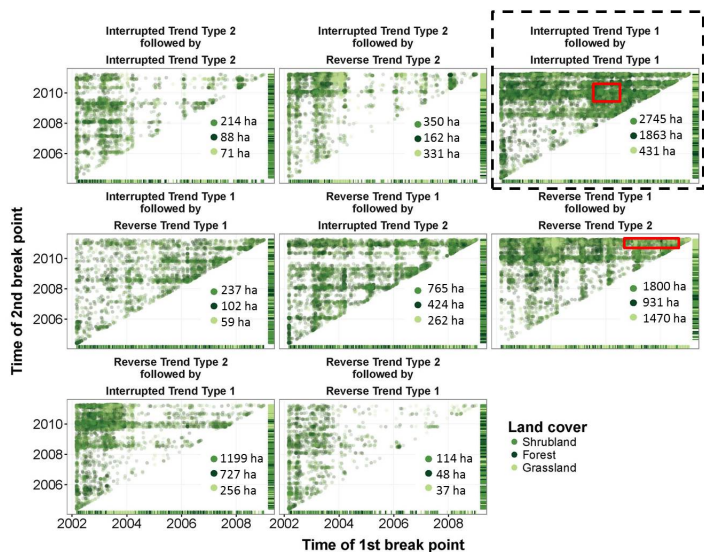Adamczyk, J., Osberger, A., 2014. Red-edge vegetation indices for detecting and assessing disturbances in norway spruce dominated mountain forests. International Journal of Applied Earth Observation and Geoinformation .

Adelabu, S., Mutanga, O., Adam, E., 2014. Evaluating the impact of red-edge band from rapideye image for classifying insect defoliation levels. ISPRS Journal of Photogrammetry and Remote Sensing 95, 34–41.

Ahlström, A., Raupach, M.R., Schurgers, G., Smith, B., Arneth, A., Jung, M., Reichstein, M., Canadell, J.G., Friedlingstein, P., Jain, A.K., et al., 2015. The dominant role of semi-arid ecosystems in the trend and variability of the land co2 sink. Science 348, 895–899.

Aishan, T., Halik, Ü., Betz, F., Gärtner, P., Cyffka, B., 2016. Modeling height–diameter relationship for populus euphratica in the tarim riparian forest ecosystem, northwest china. Journal of Forestry Research , 1–12.

Aishan, T., Halik, U., Kurban, A., Cyffka, B., Kuba, M., Betz, F., Keyimu, M., 2015. Eco-morphological response of floodplain forests (populus euphratica oliv.) to water diversion in the lower tarim river, northwest china. Environmental Earth Sciences 73, 533–545.

Al-Wassai, F.A., Kalyankar, N., 2013. Major limitations of satellite images. arXiv preprint arXiv:1307.2434 .

Allen, R.B., Bellingham, P.J., Wiser, S.K., 2003. Developing a forest biodiversity monitoring approach for new zealand. New Zealand Journal of Ecology , 207–220.

Andela, N., Liu, Y., Van Dijk, A., De Jeu, R., McVicar, T., 2013. Global changes in dryland vegetation dynamics (1988–2008) assessed by satellite remote sensing: comparing a new passive microwave vegetation density record with reflective greenness data. Biogeosciences 10, 6657–6676.

Anderson, J.R., 1976. A land use and land cover classification system for use with remote sensor data. volume 964. US Government Printing Office.

Ardila, J.P., Bijker, W., Tolpekin, V.A., Stein, A., 2012a. Context-sensitive extraction of tree crown objects in urban areas using VHR satellite images. International journal of applied earth observation and geoinformation 15, 57–69.

Ardila, J.P., Bijker, W., Tolpekin, V.A., Stein, A., 2012b. Quantification of crown changes and change uncertainty

of trees in an urban environment. ISPRS Journal of Photogrammetry and Remote Sensing 74, 41–55.

Arnett, J.T., Coops, N.C., Daniels, L.D., Falls, R.W., 2015. Detecting forest damage after a low-severity fire using remote sensing at multiple scales. International Journal of Applied Earth Observation and Geoinformation 35, 239–246.

Ashton, M.S., Tyrrell, M.L., Spalding, D., Gentry, B., 2012. Managing forest carbon in a changing climate. Springer Science & Business Media.

Assal, T.J., Anderson, P.J., Sibold, J., 2016. Spatial and temporal trends of drought effects in a heterogeneous semi-arid forest ecosystem. Forest Ecology and Management 365, 137–151.

Assessment, M.E., 2003. Ecosystems and human well-being. volume 200. Washington, DC: Island Press.

Banninger, C., 1990. Fluorescence line imager measured red edge shifts in a metal-stressed norway spruce forest and their relationship to canopy biochemical and morphological changes, in: Imaging spectroscopy of the terrestrial environment, International Society for Optics and Photonics. pp. 234–243.

Banskota, A., Kayastha, N., Falkowski, M.J., Wulder, M.A., Froese, R.E., White, J.C., 2014. Forest monitoring using landsat time series data: A review. Canadian Journal of Remote Sensing 40, 362–384.

Barbero, M., Bonin, G., Loisel, R., Quézel, P., 1990. Changes and disturbances of forest ecosystems caused by human activities in the western part of the mediterranean basin. Vegetatio 87, 151–173.

Behling, R., Roessner, S., Kaufmann, H., Kleinschmit, B., 2014. Automated spatiotemporal landslide mapping over large areas using rapideye time series data. Remote Sensing 6, 8026–8055.

Beljaev, E., Ponomarenko, M., 2005. New lepidopterological finds (lepidoptera: Gelechiidae, tortricidae, geometridae) in south of russian far east. Far Eastern Entomologist 155, 1–11.

Betz, F., Halik, Ü., Kuba, M., Tayierjiang, A., Cyffka, B., 2015. Controls on aeolian sediment dynamics by natural riparian vegetation in the eastern tarim basin, nw china. Aeolian Research 18, 23–34.

Blaschke, T., 2010. Object based image analysis for remote sensing. ISPRS Journal of Photogrammetry and Remote Sensing 65, 2–16.

Blaschke, T., Johansen, K., Tiede, D., 2011. Object-based image analysis for vegetation mapping and monitoring. Advances in Environmental Remote Sensing: Sensors, Algorithms, and Applications. Taylor & Francis, London , 241–271.

Bonan, G.B., 2008. Forests and climate change: forcings, feedbacks, and the climate benefits of forests. science 320, 1444–1449.

Braaten, J., 2015. Landsatlinkr 0.1. 6 user guide .

Brandt, M., Mbow, C., Diouf, A.A., Verger, A., Samimi, C., Fensholt, R., 2015. Ground-and satellite-based evidence of the biophysical mechanisms behind the greening sahel. Global change biology 21, 1610–1620.

Breiman, L., 2001. Random forests. Machine learning 45, 5–32.

Breiman, L., Friedman, J., Stone, C.J., Olshen, R.A., 1984. Classification and Regression Trees. ISBN 0412048418, CRC Press.

Bright, B.C., Hicke, J.A., Hudak, A.T., 2012. Estimating aboveground carbon stocks of a forest affected by mountain pine beetle in Idaho using lidar and mul-

tispectral imagery. Remote Sens. Environ. 124, 270–281.

Brokaw, N., Pickett, S., White, P., 1985. The ecology of natural disturbance and patch dynamics. The ecology of natural disturbance and patch dynamics .

Bunting, P., Lucas, R., 2006. The delineation of tree crowns in Australian mixed species forests using hyperspectral Compact Airborne Spectrographic Imager (CASI) data. Remote Sens. Environ. 101, 230–248.

Buxton, K., Maclauchlan, L., 2014. Overview of forest health conditions in southern british columbia. Report by the British Columbia Ministry of Forests, Lands, and Natural Resource Operations, Kamloops, BC .

Canty, M.J., Nielsen, A.A., 2008. Automatic radiometric normalization of multitemporal satellite imagery with the iteratively re-weighted mad transformation. Remote Sensing of Environment 112, 1025–1036.

Cao, S.K., Feng, Q., Su, Y.H., Chang, Z.Q., Xi, H.Y., 2011. Research on the water use efficiency and foliar nutrient status of populus euphratica and tamarix ramosissima in the extreme arid region of china. Environmental Earth Sciences 62, 1597–1607.

CCICCD, 1996. China National Committee for the Implementation of the UN Convention to Combat Desertification. Technical Report. China National Action Program to Combat Desertification. URL: http://www.unccd.int/ActionProgrammes/china-eng2000.pdf.

Chapin, F.S., Matson, P.A., Vitousek, P., 2011. Principles of terrestrial ecosystem ecology. Springer Science & Business Media.

Chen, Q., Baldocchi, D., Gong, P., Kelly, M., 2006a. Isolating Individual Trees in a Savanna Woodland Using Small Footprint Lidar Data. Photogrammetric Engineering & Remote Sensing 72, 923–932.

Chen, Y., Chen, Y., Xu, C., Ye, Z., Li, Z., Zhu, C., Ma, X., 2010. Effects of ecological water conveyance on groundwater dynamics and riparian vegetation in the lower reaches of tarim river, china. Hydrological Processes 24, 170–177.

Chen, Y., Li, W., Xu, C., Ye, Z., Chen, Y., 2015. Desert riparian vegetation and groundwater in the lower reaches of the tarim river basin. Environmental Earth Sciences 73, 547–558.

Chen, Y., Li, W., Xu, H., Liu, J.Z., Zhang, H., Chen, Y., 2003. The influence of groundwater on vegetation in the lower reaches of tarim river, china. Acta Geographica Sinica 58, 542–549.

Chen, Y., Pang, Z., Chen, Y., Li, W., Xu, C., Hao, X., Huang, X., Huang, T., Ye, Z., 2008. Response of riparian vegetation to water-table changes in the lower reaches of tarim river, xinjiang uygur, china. Hydrogeology Journal 16, 1371–1379.

Chen, Y., Wang, Q., Li, W., Ruan, X., Chen, Y., Zhang, L., 2006b. Rational groundwater table indicated by the ecophysiological parameters of the vegetation: a case study of ecological restoration in the lower reaches of the tarim river. Chinese Science Bulletin 51, 8–15.

Chen, Y., Zhang, X., Zhu, X., Li, W., Zhang, Y., Xu, H., Zhang, H., Chen, Y., 2004. Analysis on the ecological benefits of the stream water conveyance to the dried-up river of the lower reaches of tarim river, china. Science in China Series D: Earth Sciences 47, 1053–1064.

Chen, Y.N., Zilliacus, H., Li, W.H., Zhang, H.F., Chen, Y.P., 2006c. Groundwater level affects plant species diversity along the lower reaches of the tarim

river, western china. Journal of Arid Environments 66, 231–246.

Chubey, M.S., Franklin, S.E., Wulder, M.A., 2006. Object-based Analysis of Ikonos-2 Imagery for Extraction of Forest Inventory Parameters. Photogrammetric Engineering & Remote Sensing 72, 383.

Cleveland, R.B., Cleveland, W.S., McRae, J.E., Terpenning, I., 1990. Stl: A seasonal-trend decomposition procedure based on loess. Journal of Official Statistics 6, 3–73.

Cohen, W.B., Yang, Z., Kennedy, R., 2010. Detecting trends in forest disturbance and recovery using yearly landsat time series: 2. timesync - tools for calibration and validation. Remote Sensing of Environment 114, 2911–2924.

van Coillie, F.M.B., Devriendt, F., De Wulf, R.R., 2012. Directional Local Filtering Assisting Individual Tree Analysis in Closed Forest Canopies using VHR Optical and LiDAR Data, in: Proceedings of the 4th GEOBIA, Rio de Janeiro - Brazil. pp. 350–354.

Conradie, B., "Um"ut, H., Birgit, K., Johannes, K., 2007. EVASTar - Automatisierte Erfassung der Vitatli"at von Auw"aldern im vollariden Milieu mit h"ochstaufl"osendenen Satellitendaten. Final Report. Technische Universit"at Berlin.

Coops, N.C., Hilker, T., Bater, C.W., Wulder, M.A., Nielsen, S.E., McDermid, G., Stenhouse, G., 2012. Linking ground-based to satellite-derived phenological metrics in support of habitat assessment. Remote Sensing Letters 3, 191–200.

Coppin, P., Jonckheere, I., Nackaerts, K., Muys, B., Lambin, E., 2004. Review Article Digital change detection methods in ecosystem monitoring: a review. Int. J. Remote Sens. 25, 1565–1596.

Coppin, P.R., Bauer, M.E., 1995. The potential contribution of pixel-based canopy change information to stand-based forest management in the northern us. Journal of Environmental Management 44, 69–82.

Coppin, P.R., Bauer, M.E., 1996. Digital change detection in forest ecosystems with remote sensing imagery. Remote sensing reviews 13, 207–234.

Culvenor, D.S., 2002. TIDA: an algorithm for the delineation of tree crowns in high spatial resolution remotely sensed imagery. Computers & Geosciences 28, 33–44.

Curran, P.J., Dungan, J.L., Gholz, H.L., 1990. Exploring the relationship between reflectance red edge and chlorophyll content in slash pine. Tree physiology 7, 33–48.

Curran, P.J., Dungan, J.L., Macler, B.A., Plummer, S.E., 1991. The effect of a red leaf pigment on the relationship between red edge and chlorophyll concentration. Remote Sensing of Environment 35, 69–76.

Dale, V.H., Joyce, L.A., McNulty, S., Neilson, R.P., Ayres, M.P., Flannigan, M.D., Hanson, P.J., Irland, L.C., Lugo, A.E., Peterson, C.J., et al., 2001. Climate change and forest disturbances: climate change can affect forests by altering the frequency, intensity, duration, and timing of fire, drought, introduced species, insect and pathogen outbreaks, hurricanes, windstorms, ice storms, or landslides. BioScience 51, 723–734.

Dalponte, M., Bruzzone, L., Gianelle, D., 2008. Fusion of hyperspectral and lidar remote sensing data for classification of complex forest areas. IEEE Transactions on Geoscience and Remote Sensing 46, 1416–1427.

Darmawan, Y., Sofan, P., 2014. Comparison of the vegetation indices to detect

the tropical rain forest changes using breaks for additive seasonal and trend (bfast) model. International Journal of Remote Sensing and Earth Sciences (IJReSES) 9.

De Beurs, K., Townsend, P., 2008. Estimating the effect of gypsy moth defoliation using modis. Remote Sensing of Environment 112, 3983–3990.

Deng, X., Xu, H., Ye, M., Li, B., Fu, J., Yang, Z., 2015. Impact of long-term zero-flow and ecological water conveyance on the radial increment of populus euphratica in the lower reaches of the tarim river, xinjiang, china. Regional Environmental Change 15, 13–23.

Dennison, P.E., Nagler, P.L., Hultine, K.R., Glenn, E.P., Ehleringer, J.R., 2009. Remote monitoring of tamarisk defoliation and evapotranspiration following saltcedar leaf beetle attack. Remote Sensing of Environment 113, 1462–1472.

Desclée, B., Bogaert, P., Defourny, P., 2006. Forest change detection by statistical object-based method. Remote Sens. Environ. 102, 1–11.

DeVries, B., Decuyper, M., Verbesselt, J., Zeileis, A., Herold, M., Joseph, S., 2015a. Tracking disturbance-regrowth dynamics in tropical forests using structural change detection and landsat time series. Remote Sensing of Environment 169, 320–334.

DeVries, B., Pratihast, A.K., Verbesselt, J., Kooistra, L., Herold, M., 2016. Characterizing forest change using community-based monitoring data and landsat time series. PloS one 11, e0147121.

DeVries, B., Verbesselt, J., Kooistra, L., Herold, M., 2015b. Robust monitoring of small-scale forest disturbances in a tropical montane forest using landsat time series. Remote Sensing of Environment 161, 107–121.

Dobbertin, M., 2005. Tree growth as indicator of tree vitality and of tree reaction to environmental stress: a review. European Journal of Forest Research 124, 319–333.

Donohue, R.J., Roderick, M.L., McVicar, T.R., Farquhar, G.D., 2013. Impact of co2 fertilization on maximum foliage cover across the globe's warm, arid environments. Geophysical Research Letters 40, 3031–3035.

Dregne, H.E., 2002. Land degradation in the drylands. Arid land research and management 16, 99–132.

Dutrieux, L.P., Verbesselt, J., Kooistra, L., Herold, M., 2015. Monitoring forest cover loss using multiple data streams, a case study of a tropical dry forest in bolivia. ISPRS Journal of Photogrammetry and Remote Sensing 107, 112–125.

Eckert, S., 2012. Improved forest biomass and carbon estimations using texture measures from worldview-2 satellite data. Remote sensing 4, 810–829.

eCognition, 2010. Ruleset: Conditional Quad Tree segmentation.

eCognition, 2012. Trimble. "eCognition Developer 8.8. 1 User Guide." Trimble Germany GmbH, Munich, Germany.

Eitel, J.U., Vierling, L.A., Litvak, M.E., Long, D.S., Schulthess, U., Ager, A.A., Krofcheck, D.J., Stoscheck, L., 2011. Broadband, red-edge information from satellites improves early stress detection in a new mexico conifer woodland. Remote Sensing of Environment 115, 3640–3646.

Elatawneh, A., Wallner, A., Manakos, I., Schneider, T., Knoke, T., 2014. Forest cover database updates using multi-seasonal rapideye data-storm event assessment in the bavarian forest national park. Forests 5, 1284–1303.

Elmqvist, T., Folke, C., Nyström, M., Peterson, G., Bengtsson, J., Walker, B.,

Norberg, J., 2003. Response diversity, ecosystem change, and resilience. Frontiers in Ecology and the Environment 1, 488–494.

Emelyanova, I.V., McVicar, T.R., Van Niel, T.G., Li, L.T., van Dijk, A.I., 2013. Assessing the accuracy of blending landsat–modis surface reflectances in two landscapes with contrasting spatial and temporal dynamics: A framework for algorithm selection. Remote Sensing of Environment 133, 193–209.

Erschoff, N., 1874. Lepidoptera. Fedtshenko, AP: Journey to Turkestan II 2, 7.

Eusemann, P., Petzold, A., Thevs, N., Schnittler, M., 2013. Growth patterns and genetic structure of populus euphratica oliv.(salicaceae) forests in nw china–implications for conservation and management. Forest Ecology and Management 297, 27–36.

Falkowski, M.J., Wulder, M.A., White, J.C., Gillis, M.D., 2009. Supporting large-area, sample-based forest inventories with very high spatial resolution satellite imagery. Progress in Physical Geography 33, 403–423.

Fan, Z., 1996. Research on the impacts of land utilization to ecology and environment in xinjiang and the correspondent countermeasures. Qixiang Chubanshe, Beijing (in Chinese) .

FAO, 2015. Forest area (percent of land area). Technical Report. Food and Agriculture Organization.

Feng, Q., Endo, K., Cheng, G., 2001. Towards sustainable development of the environmentally degraded arid rivers of china - a case study from tarim river. Environmental Geology 41, 229–238.

Fensholt, R., Langanke, T., Rasmussen, K., Reenberg, A., Prince, S.D., Tucker, C., Scholes, R.J., Le, Q.B., Bondeau, A., Eastman, R., et al., 2012. Greenness in semi-arid areas across the globe 1981–2007. an earth observing satellite based analysis of trends and drivers. Remote Sensing of Environment 121, 144–158.

Food, U., Organization, A., et al., 2006. Global forest resources assessment 2005. FAO Forestry Paper 147.

Foody, G.M., 2010. Assessing the accuracy of land cover change with imperfect ground reference data. Remote Sens. Environ. 114, 2271–2285.

Franke, J., Keuck, V., Siegert, F., 2012. Assessment of grassland use intensity by remote sensing to support conservation schemes. Journal for Nature Conservation 20, 125–134.

Franklin, S.E., 2001. Remote sensing for sustainable forest management. CRC Press.

Frazier, R.J., Coops, N.C., Wulder, M.A., 2015. Boreal shield forest disturbance and recovery trends using landsat time series. Remote Sensing of Environment 170, 317–327.

Fu, D., Chen, B., Wang, J., Zhu, X., Hilker, T., 2013. An improved image fusion approach based on enhanced spatial and temporal the adaptive reflectance fusion model. Remote Sensing 5, 6346–6360.

Gao, F., Masek, J., Schwaller, M., Hall, F., 2006. On the blending of the landsat and modis surface reflectance: Predicting daily landsat surface reflectance. Geoscience and Remote Sensing, IEEE Transactions on 44, 2207–2218.

Gärtner, P., Förster, M., Kleinschmit, B., 2016. The benefit of synthetically generated rapideye and landsat 8 data fusion time series for riparian forest disturbance monitoring. Remote Sensing of Environment 177, 237–247.

Gärtner, P., Förster, M., Kurban, A., Kleinschmit, B., 2014. Object based change detection of central asian tugai vegetation with very high spatial resolution

satellite imagery. International Journal of Applied Earth Observation and Geoinformation 31, 110–121.

Gaulton, R., Hilker, T., Wulder, M.A., Coops, N.C., Stenhouse, G., 2011. Characterizing stand-replacing disturbance in western alberta grizzly bear habitat, using a satellite-derived high temporal and spatial resolution change sequence. Forest Ecology and Management 261, 865–877.

Gebreslasie, M., Ahmed, F., Van Aardt, J.A., Blakeway, F., 2011. Individual tree detection based on variable and fixed window size local maxima filtering applied to IKONOS imagery for even-aged Eucalyptus plantation forests. Int. J. Remote Sens. 32, 4141–4154.

Gibson, P., et al., 2013. Introductory remote sensing principles and concepts. Routledge.

Gitelson, A., Merzlyak, M.N., 1994. Spectral Reflectance Changes Associated with Autumn Senescence of *Aesculus hippocastanum L.* and *Acer platanoides L.* Leaves. Spectral Features and Relation to Chlorophyll Estimation. J. Plant Physiol. 143, 286–292.

Gitelson, A.A., Kaufman, Y.J., Merzlyak, M.N., 1996. Use of a green channel in remote sensing of global vegetation from EOS-MODIS. Remote Sens. Environ. 58, 289–298.

Gomes, M.F., Maillard, P., 2013. Identification of urban tree crown in a tropical environment using worldview-2 data: Problems and perspectives, in: SPIE Remote Sensing, International Society for Optics and Photonics. pp. 88930C–88930C.

Gómez, C., White, J.C., Wulder, M.A., Alejandro, P., 2014. Historical forest biomass dynamics modelled with landsat spectral trajectories. ISPRS Journal of Photogrammetry and Remote Sensing 93, 14–28.

Goodwin, N.R., Coops, N.C., Wulder, M.A., Gillanders, S., Schroeder, T.A., Nelson, T., 2008. Estimation of insect infestation dynamics using a temporal sequence of landsat data. Remote sensing of environment 112, 3680–3689.

Gougeon, F.A., Leckie, D.G., 2006. The Individual Tree Crown Approach Applied to Ikonos Images of a Coniferous Plantation Area. Photogrammetric Engineering & Remote Sensing 72, 1287–1297.

Gougeon, F.A., Moore, T., 1988. Individual tree classification using MEIS-II imagery, in: Geoscience and Remote Sensing Symposium. IGARSS'88. Remote Sensing: Moving Toward the 21st Century., International, IEEE. pp. 927–928.

Gries, D., Foetzki, A., Arndt, S.K., Bruelheide, H., Thomas, F.M., Zhang, X., Runge, M., 2005. Production of perennial vegetation in an oasis-desert transition zone in nw china-allometric estimation, and assessment of flooding and use effects. Plant Ecology 181, 23–43.

Gries, D., Zeng, F., Foetzki, A., Arndt, S.K., Bruelheide, H., Thomas, F.M., Zhang, X., Runge, M., 2003. Growth and water relations of tamarix ramosissima and populus euphratica on taklamakan desert dunes in relation to depth to a permanent water table. Plant, cell & environment 26, 725–736.

Grime, J.P., 1977. Evidence for the existence of three primary strategies in plants and its relevance to ecological and evolutionary theory. American naturalist , 1169–1194.

Grünzweig, J., Lin, T., Rotenberg, E., Schwartz, A., Yakir, D., 2003. Carbon sequestration in arid-land forest. Global Change Biology 9, 791–799.

Guardiola-Claramonte, M., Troch, P.A., Breshears, D.D., Huxman, T.E., Swi-

tanek, M.B., Durcik, M., Cobb, N.S., 2011. Decreased streamflow in semi-arid basins following drought-induced tree die-off: a counter-intuitive and indirect climate impact on hydrology. Journal of Hydrology 406, 225–233.

Halik, Ü., Kurban, A., Mijit, M., Schulz, J., Paproth, F., Coenradie, B., 2006. The potential influence of embankment engineering and ecological water transfers on the riparian vegetation along the middle and lower reaches of the tarim river. Watershed and Floodplain Management along the Tarim River in Chinas Arid Northwest , 221–236.

Hall, R.J., Skakun, R.S., Arsenault, E.J., 2006. Remotely sensed data in the mapping of insect defoliation. Understanding forest disturbance and spatial pattern: Remote sensing and GIS approaches , 85–111.

Hansen, M.C., Potapov, P.V., Moore, R., Hancher, M., Turubanova, S., Tyukavina, A., Thau, D., Stehman, S., Goetz, S., Loveland, T., et al., 2013. High-resolution global maps of 21st-century forest cover change. Science 342, 850–853.

Hansen, M.C., Roy, D.P., Lindquist, E., Adusei, B., Justice, C.O., Altstatt, A., 2008. A method for integrating modis and landsat data for systematic monitoring of forest cover and change in the congo basin. Remote Sensing of Environment 112, 2495–2513.

Hao, X., Li, W., 2014. Impacts of ecological water conveyance on groundwater dynamics and vegetation recovery in the lower reaches of the tarim river in northwest china. Environmental monitoring and assessment 186, 7605–7616.

Hao, X., Li, W., Huang, X., Zhu, C., Ma, J., 2010. Assessment of the groundwater threshold of desert riparian forest vegetation along the middle and lower

reaches of the tarim river, china. Hydrological Processes 24, 178–186.

Hartanto, H., Prabhu, R., Widayat, A.S., Asdak, C., 2003. Factors affecting runoff and soil erosion: plot-level soil loss monitoring for assessing sustainability of forest management. Forest Ecology and Management 180, 361–374.

Hilker, T., Wulder, M.A., Coops, N.C., Linke, J., McDermid, G., Masek, J.G., Gao, F., White, J.C., 2009a. A new data fusion model for high spatial- and temporal-resolution mapping of forest disturbance based on landsat and modis. Remote Sensing of Environment 113, 1613–1627.

Hilker, T., Wulder, M.A., Coops, N.C., Seitz, N., White, J.C., Gao, F., Masek, J.G., Stenhouse, G., 2009b. Generation of dense time series synthetic landsat data through data blending with modis using a spatial and temporal adaptive reflectance fusion model. Remote Sensing of Environment 113, 1988–1999.

Hirata, Y., 2008. Estimation of stand attributes in *Cryptomeria japonica* and *Chamaecyparis obtusa* stands using QuickBird panchromatic data. Journal of Forest Research 13, 147–154.

Horion, S., Prishchepov, A.V., Verbesselt, J., Beurs, K., Tagesson, T., Fensholt, R., 2016. Revealing turning points in ecosystem functioning over the northern eurasian agricultural frontier. Global Change Biology .

Huang, C., Goward, S.N., Masek, J.G., Thomas, N., Zhu, Z., Vogelmann, J.E., 2010. An automated approach for reconstructing recent forest disturbance history using dense landsat time series stacks. Remote Sensing of Environment 114, 183–198.

Huete, A., 1988. A soil-adjusted vegetation index (SAVI). Remote Sens. Envi-

ron. 25, 295–309.

Huete, A., Didan, K., Miura, T., Rodriguez, E.P., Gao, X., Ferreira, L.G., 2002. Overview of the radiometric and biophysical performance of the modis vegetation indices. Remote sensing of environment 83, 195–213.

Hüseyinova, R., Kilinc, M., Kutbay, H.G., Kilic, D.D., Bilgin, A., 2013. The comparison of grime's strategies of plant taxa in hacı osman forest and bafra fish lakes in the central black sea region of turkey. Turkish Journal of Botany 37, 725–734.

Jarihani, A.A., McVicar, T.R., Van Niel, T.G., Emelyanova, I.V., Callow, J.N., Johansen, K., 2014. Blending landsat and modis data to generate multispectral indices: A comparison of "index-then-blend" and "blend-then-index" approaches. Remote Sensing 6, 9213–9238.

Ji, L., Wang, Z., Wang, X., An, L., 2011. Forest insect pest management and forest management in china: An overview. Environmental management 48, 1107–1121.

Jones, H.G., Vaughan, R.A., 2010. Remote sensing of vegetation: principles, techniques, and applications. Oxford University Press.

de Jong, R., de Bruin, S., de Wit, A., Schaepman, M.E., Dent, D.L., 2011. Analysis of monotonic greening and browning trends from global ndvi timeseries. Remote Sensing of Environment 115, 692–702.

de Jong, R., Verbesselt, J., Zeileis, A., Schaepman, M.E., 2013. Shifts in global vegetation activity trends. Remote Sensing 5, 1117–1133.

Jordan, C.F., 1969. Derivation of leaf-area index from quality of light on the forest floor. Ecology , 663–666.

Joshi, N., Baumann, M., Ehammer, A., Fensholt, R., Grogan, K., Hostert, P., Jepsen, M.R., Kuemmerle, T., Meyfroidt, P., Mitchard, E.T., et al., 2016. A review of the application of optical and radar remote sensing data fusion to land use mapping and monitoring. Remote Sensing 8, 70.

Kalkhan, M.A., 2011. Spatial statistics: geospatial information modeling and thematic mapping. CRC Press.

Karlson, M., Reese, H., Ostwald, M., 2014. Tree crown mapping in managed woodlands (parklands) of semi-arid west africa using worldview-2 imagery and geographic object based image analysis. Sensors 14, 22643–22669.

Katoh, M., Gougeon, F.A., 2012. Improving the Precision of Tree Counting by Combining Tree Detection with Crown Delineation and Classification on Homogeneity Guided Smoothed High Resolution (50 cm) Multispectral Airborne Digital Data. Remote Sensing 4, 1411–1424.

Ke, Y., Quackenbush, L.J., 2011a. A comparison of three methods for automatic tree crown detection and delineation from high spatial resolution imagery. Int. J. Remote Sens. 32, 3625–3647.

Ke, Y., Quackenbush, L.J., 2011b. A review of methods for automatic individual tree-crown detection and delineation from passive remote sensing. Int. J. Remote Sens. 32, 4725–4747.

Kennedy, R.E., Cohen, W.B., Schroeder, T.A., 2007. Trajectory-based change detection for automated characterization of forest disturbance dynamics. Remote Sensing of Environment 110, 370–386.

Kennedy, R.E., Yang, Z., Cohen, W.B., 2010. Detecting trends in forest disturbance and recovery using yearly landsat time series: 1. landtrendr - temporal seg-

mentation algorithms. Remote Sensing of Environment 114, 2897–2910.

Kerdiles, H., Grondona, M.O., 1995. NOAA-AVHRR NDVI decomposition and subpixel classification using linear mixing in the argentinean pampa. International Journal of Remote Sensing 16, 1303–1325.

Kong, W., Sun, O., Xu, W., Chen, Y., 2009. Changes in vegetation and landscape patterns with altered river water-flow in arid west china. Journal of arid environments 73, 306–313.

Kotlyakov, V.M., 1991. The aral sea basin: a critical environmental zone. Environment: Science and Policy for Sustainable Development 33, 4–38.

Kozlowski, T., Pallardy, S., 2002. Acclimation and adaptive responses of woody plants to environmental stresses. The botanical review 68, 270–334.

Krause, K., 2005. Radiometric Use of QuickBird Imagery. Technical Note. DigitalGlobe. 1601 Dry Creek Drive Suite 260, Longmont, Colorado, USA, 80503.

Laliberte, A.S., Fredrickson, E.L., Rango, A., 2007. Combining Decision Trees with Hierarchical Object-oriented Image Analysis for Mapping Arid Rangelands. Photogrammetric Engineering & Remote Sensing 73, 197.

Lam, T.Y., Kleinn, C., Coenradie, B., 2011. Double sampling for stratification for the monitoring of sparse tree populations: the example of populus euphratica oliv. forests at the lower reaches of tarim river, southern Xinjiang, china. Environmental monitoring and assessment 175, 45–61.

Leckie, D.G., Gougeon, F.A., Hill, D., Quinn, R., Armstrong, L., Shreenan, R., 2003a. Combined high-density lidar and multispectral imagery for individual tree crown analysis. Canadian Journal of Remote Sensing 29, 633–649.

Leckie, D.G., Gougeon, F.A., Tinis, S., Nelson, T., Burnett, C.N., Paradine, D., 2005. Automated tree recognition in old growth conifer stands with high resolution digital imagery. Remote Sens. Environ. 94, 311–326.

Leckie, D.G., Gougeon, F.A., Walsworth, N., Paradine, D., 2003b. Stand delineation and composition estimation using semi-automated individual tree crown analysis. Remote Sens. Environ. 85, 355–369.

Leckie, D.G., Jay, C., Gougeon, F.A., Sturrock, R., Paradine, D., 2004. Detection and assessment of trees with *Phellinus weirii* (laminated root rot) using high resolution multi-spectral imagery. Int. J. Remote Sens. 25, 793–818.

Lefsky, M.A., Cohen, W.B., 2003. Selection of remotely sensed data, in: Remote sensing of forest environments. Springer, pp. 13–46.

Lehmann, E.A., Wallace, J.F., Caccetta, P.A., Furby, S.L., Zdunic, K., 2013. Forest cover trends from time series landsat data for the australian continent. International Journal of Applied Earth Observation and Geoinformation 21, 453–462.

Lei, Z., 2008. Reform of the forest sector in china. Re-inventing forestry agencies , 215.

Leprieur, C., Kerr, Y., Mastorchio, S., Meunier, J., 2000. Monitoring vegetation cover across semi-arid regions: comparison of remote observations from various scales. International Journal of Remote Sensing 21, 281–300.

Li, J., Yu, B., Zhao, C., Nowak, R.S., Zhao, Z., Sheng, Y., 2013a. Physiological and morphological responses of tamarix ramosissima and populus euphratica to

altered groundwater availability. Tree physiology 33, 57–68.

Li, W., Zhou, H., Fu, A., Chen, Y., 2013b. Ecological response and hydrological mechanism of desert riparian forest in inland river, northwest of china. Ecohydrology 6, 949–955.

Li, X., Hou, P., Yang, P., 2006. Analysis on the respond of the tree-rings of populus euphratica to the change of moisture conditions in the lower reaches of the tarim river. Arid Zone Research 23, 26–31.

Liang, E., Shao, X., Kong, Z., Lin, J., 2003. The extreme drought in the 1920s and its effect on tree growth deduced from tree ring analysis: a case study in north china. Annals of Forest Science 60, 145–152.

Ling, H., Zhang, P., Xu, H., Zhao, X., 2015. How to regenerate and protect desert riparian populus euphratica forest in arid areas. Scientific reports 5.

Liphschitz, N., Waisel, Y., 1970. Effects of environment on relations between extension and cambial growth of populus euphratica oliv. New Phytologist 69, 1059–1064.

Liu, Q.w., Hao, P., Li, J.w., Tan, Z.g., Luo, J.y., et al., 2011. Effect of stand age and individual growth on seed germination of populus euphratica in the ejina oasis, china. Forestry Studies in China 13, 183–188.

Liu, S., Xue, D., Cheng, R., Han, H., 2014. "the complete mitogenome of *Apocheima cinerarius* (lepidoptera: Geometridae: Ennominae) and comparison with that of other lepidopteran insects". Gene 547, 136–144.

Liu, Y., Chen, Y., 2006. Impact of population growth and land-use change on water resources and ecosystems of the arid tarim river basin in western china. The International Journal of Sustainable Development & World Ecology 13, 295–305.

Lyle, C., Gaofeng, M., 2011. Integrated management of the Tarim river basin, Xinjiang China 5.

Malagnoux, M., 2007. Arid land forests of the world: global environmental perspectives, in: International Conference on Afforestation and Sustainable Forests as a Means to Combat Desertification, Jerusalem, Israel, pp. 16–19.

Marx, A., 2010. Detection and classification of bark beetle infestation in pure norway spruce stands with multitemporal rapideye imagery and data mining techniques. Photogramm. Fernerk. Geoinf 4, 243–252.

Masek, J.G., Vermote, E.F., Saleous, N.E., Wolfe, R., Hall, F.G., Huemmrich, K.F., Gao, F., Kutler, J., Lim, T.K., 2006. A landsat surface reflectance dataset for north america, 1990-2000. Geoscience and Remote Sensing Letters, IEEE 3, 68–72.

McFeeters, S., 1996. The use of the Normalized Difference Water Index (NDWI) in the delineation of open water features. Int. J. Remote Sens. 17, 1425–1432.

Metcalfe, D.B., 2014. Climate science: A sink down under. Nature 509, 566–567.

Monda, Y., Miki, N., Yoshikawa, K., 2008. Stand structure and regeneration of populus euphratica forest in the lower reaches of the heihe river, nw china. Landscape and Ecological Engineering 4, 115–124.

Mora, B., Wulder, M.A., White, J.C., Hobart, G., 2013. Modeling Stand Height, Volume, and Biomass from Very High Spatial Resolution Satellite Imagery and Samples of Airborne LiDAR. Remote Sensing 5, 2308–2326.

Ni, J., Zhang, X.s., Scurlock, J.M., 2001. Synthesis and analysis of biomass and

net primary productivity in chinese forests. Annals of Forest Science 58, 351–384.

Niccolai, A., Hohl, A., Niccolai, M., Oliver, C.D., 2010. Integration of varying spatial, spectral and temporal high-resolution optical images for individual tree crown isolation. Int. J. Remote Sens. 31, 5061–5088.

Nilsson, C., Berggren, K., 2000. Alterations of riparian ecosystems caused by river regulation dam operations have caused global-scale ecological changes in riparian ecosystems. how to protect river environments and human needs of rivers remains one of the most important questions of our time. BioScience 50, 783–792.

Niu, R., Liu, J., Zhao, X., Qin, Y., 2015. Ecological benefit of different revegetated covers in the middle of hexi corridor, northwestern china. Environmental Earth Sciences 74, 5699–5710.

Novikova, N., Kust, G., Kuzmina, J., Trofimova, G., Dikariova, T., Avetian, S., Rozov, S., Deruzhinskaya, V., Safonicheva, L., Lubeznov, U., 1998. Contemporary plant and soil cover changes in the amu-darya and syr-darya river deltas. Ecological Research and Monitoring of the Aral Sea Deltas–A basis for restoration .

Olsson, H., Egberth, M., Engberg, J., Fransson, J.E., Pahlén, T.G., Hagner, O., Holmgren, J., Joyce, S., Magnusson, M., Nilsson, B., et al., 2005. Current and Emerging Operational Uses of Remote Sensing in Swedish Forestry, in: Proceedings of the Seventh Annual Forest Inventory and Analysis Symposium. USDA Forest Serv. Gen Tech Rep WO-69, pp. 39–46.

Ortiz, S.M., Breidenbach, J., Kändler, G., 2013. Early detection of bark beetle green attack using terrasar-x and rapid-

eye data. Remote Sensing 5, 1912–1931.

Osberger, A., Tiede, D., Lang, S., 2013. Forest disturbance monitoring system based on high spatial resolution satellite images in the kalkalpen national park, in: 5th Symposium for Research in Protected Areas, pp. 545–550.

Ozdemir, I., 2008. Estimating stem volume by tree crown area and tree shadow area extracted from pan-sharpened Quickbird imagery in open Crimean juniper forests. Int. J. Remote Sens. 29, 5643–5655.

Ozdemir, I., Karnieli, A., 2011. Predicting forest structural parameters using the image texture derived from worldview-2 multispectral imagery in a dryland forest, israel. International Journal of Applied Earth Observation and Geoinformation 13, 701–710.

Padarian, J., Minasny, B., McBratney, A., 2015. Using google's cloud-based platform for digital soil mapping. Computers & Geosciences 83, 80–88.

Padwick, C., Deskevich, M., Pacifici, F., Smallwood, S., 2010. WorldView-2 Pan-Sharpening, in: American Society for Photogrammetry and Remote Sensing, San Diego, California. pp. 1–14.

Paproth, 2004. Map of the Tarim Basin: Modified by (Pietsch 2011).

Peerbhay, K.Y., Mutanga, O., Ismail, R., 2014. Investigating the capability of few strategically placed worldview-2 multispectral bands to discriminate forest species in kwazulu-natal, south africa. IEEE Journal of Selected Topics in Applied Earth Observations and Remote Sensing 7, 307–316.

Perry, D.A., Oren, R., Hart, S.C., 2008. Forest ecosystems. JHU Press.

Pettorelli, N., Vik, J.O., Mysterud, A., Gaillard, J.M., Tucker, C.J., Stenseth, N.C., 2005. Using the satellite-derived ndvi

to assess ecological responses to environmental change. Trends in ecology & evolution 20, 503–510.

Pflugmacher, D., Cohen, W.B., Kennedy, R.E., Yang, Z., 2014. Using landsat-derived disturbance and recovery history and lidar to map forest biomass dynamics. Remote Sensing of Environment 151, 124–137.

Piao, S., Ciais, P., Huang, Y., Shen, Z., Peng, S., Li, J., Zhou, L., Liu, H., Ma, Y., Ding, Y., et al., 2010. The impacts of climate change on water resources and agriculture in china. Nature 467, 43–51.

Pietsch, C., 2013. Lower reaches of tarim river −project area [map, scale not given]., in: In T. Aishan and Ü. Halik and A. Kurban and B. Cyffka and M. Kuba and F. Betz and M. Keyimu (Eds.), Ecomorphological response of floodplain forests (Populus euphratica Oliv.) to water diversion in the lower Tarim River, northwest China (p. p. 3):. Environenmal Earth Science.

Postel, S.L., Thompson, B.H., 2005. Watershed protection: Capturing the benefits of nature's water supply services, in: Natural Resources Forum, Wiley Online Library. pp. 98–108.

Pouliot, D.A., King, D.J., Bell, F.W., Pitt, D.G., 2002. Automated tree crown detection and delineation in high-resolution digital camera imagery of coniferous forest regeneration. Remote Sens. Environ. 82, 322–334.

Pouliot, D.A., King, D.J., Pitt, D.G., 2005. Development and evaluation of an automated tree detection delineation algorithm for monitoring regenerating coniferous forests. Canadian Journal of Forest Research 35, 2332–2345.

Powell, S.L., Cohen, W.B., Healey, S.P., Kennedy, R.E., Moisen, G.G., Pierce, K.B., Ohmann, J.L., 2010. Quantification of live aboveground forest biomass dynamics with landsat time-series and field inventory data: A comparison of empirical modeling approaches. Remote Sensing of Environment 114, 1053–1068.

Qi, J., Chehbouni, A., Huete, A., Kerr, Y., Sorooshian, S., 1994. A modified soil adjusted vegetation index. Remote Sens. Environ. 48, 119–126.

Qisen, L., Qi, F., Luxin, Z., 2010. Study of the height growth dynamic based on tree-ring data in populus euphratica from the lower reach of the heihe river, china. Dendrochronologia 28, 49–64.

R Core Team, 2015. R: A Language and Environment for Statistical Computing. R Foundation for Statistical Computing. Vienna, Austria. URL: http://www.R-project.org/.

RapidEye, A., 2011. Satellite imagery product specifications.

Ravi, S., Breshears, D.D., Huxman, T.E., D'Odorico, P., 2010. Land degradation in drylands: Interactions among hydrologic–aeolian erosion and vegetation dynamics. Geomorphology 116, 236–245.

Röhle, H., 1986. Vergleichende Untersuchungen zur Ermittlung der Genauigkeit bei der Ablotung von Kronenradien. Forstarchiv 57, 67–71.

Richter, B., Baumgartner, J., Wigington, R., Braun, D., 1997. How much water does a river need? Freshwater biology 37, 231–249.

Richter, K., Hank, T.B., Atzberger, C., Mauser, W., 2011. Goodness-of-fit measures: what do they tell about vegetation variable retrieval performance from earth observation data, in: SPIE Remote Sensing, International Society for Optics and Photonics. pp. 81740R–81740R.

Rocchini, D., Foody, G.M., Nagendra, H., Ricotta, C., Anand, M., He, K.S., Am-

ici, V., Kleinschmit, B., Förster, M., Schmidtlein, S., et al., 2013. Uncertainty in ecosystem mapping by remote sensing. Computers & Geosciences 50, 128–135.

Rondeaux, G., Steven, M., Baret, F., 1996. Optimization of soil-adjusted vegetation indices. Remote Sens. Environ. 55, 95–107.

Rouse Jr, J., Haas, R., Schell, J., Deering, D., 1974. Monitoring vegetation systems in the great plains with erts. NASA special publication 351, 309.

Roy, D., Wulder, M., Loveland, T., CE, W., Allen, R., Anderson, M., Helder, D., Irons, J., Johnson, D., Kennedy, R., et al., 2014. Landsat-8: Science and product vision for terrestrial global change research. Remote Sensing of Environment 145, 154–172.

Roy, D.P., Ju, J., Kline, K., Scaramuzza, P.L., Kovalskyy, V., Hansen, M., Loveland, T.R., Vermote, E., Zhang, C., 2010. Web-enabled landsat data (weld): Landsat etm+ composited mosaics of the conterminous united states. Remote Sensing of Environment 114, 35–49.

Roy, D.P., Ju, J., Lewis, P., Schaaf, C., Gao, F., Hansen, M., Lindquist, E., 2008. Multi-temporal modis-landsat data fusion for relative radiometric normalization, gap filling, and prediction of landsat data. Remote Sensing of Environment 112, 3112–3130.

Rumbaur, C., Thevs, N., Disse, M., Ahlheim, M., Brieden, A., Cyffka, B., Duethmann, D., Feike, T., Fr"or, O., G"artner, P., Halik, U., Hill, J., Hinnenthal, M., Keilholz, P., Kleinschmit, B., Krysanova, V., Kuba, M., Mader, S., Menz, C., Othmanli, H., Pelz, S., Schroeder, M., Siew, T.F., Stender, V., Stahr, K., Thomas, F.M., Welp, M., Wortmann, M., X. Zhao, X.C., Jiang, T., Luo, J., Yimit, H., Yu, R., Zhang, X., Zhao, C., 2015. Sustainable management of river oases along the tarim river (sumario) in northwest china under conditions of climate change. Earth System Dynamics 6, 83–107.

Sader, S.A., Bertrand, M., Wilson, E.H., 2003. Satellite Change Detection of Forest Harvest Patterns on an Industrial Forest Landscape. Forest Science 49, 341–353.

Sahu, K.C., 2007. Textbook of remote sensing and geographical information systems. Atlantic Publishers & Dist.

van der Sande, C.J., 2010. AUTOMATIC OBJECT RECOGNITION AND CHANGE DETECTION OF URBAN TREES. The International Archives of the Photogrammetry, Remote Sensing and Spatial Information Sciences Vol. XXXVIII-4/C7.

Säumel, I., Ziche, D., Yu, R., Kowarik, I., Overdieck, D., 2011. Grazing as a driver for populus euphratica woodland degradation in the semi-arid aibi hu region, northwestern china. Journal of arid environments 75, 265–269.

Scaramuzza, P., Micijevic, E., Chander, G., 2004. Slc gap-filled products phase one methodology. Landsat Technical Notes .

Schmidt, M., Lucas, R., Bunting, P., Verbesselt, J., Armston, J., 2015. Multi-resolution time series imagery for forest disturbance and regrowth monitoring in queensland, australia. Remote Sensing of Environment 158, 156–168.

Schmidt, M., Udelhoven, T., Gill, T., Röder, A., 2012. Long term data fusion for a dense time series analysis with modis and landsat imagery in an australian savanna. Journal of Applied Remote Sensing 6, 063512–1.

Schomaker, M.E., Zarnoch, S.J., Bechtold, W.A., Latelle, D.J., Burkman, W.G., Cox, S.M., 2007. Crown-condition clas-

sification: a guide to data collection and analysis. Gen. Tech. Rep. SRS-102. Asheville, NC: US Department of Agriculture, Forest Service, Southern Research Station .

Schroeder, T.A., Wulder, M.A., Healey, S.P., Moisen, G.G., 2011. Mapping wildfire and clearcut harvest disturbances in boreal forests with landsat time series data. Remote Sensing of Environment 115, 1421–1433.

Schucknecht, A., Erasmi, S., Niemeyer, I., Matschullat, J., 2013. Assessing vegetation variability and trends in northeastern brazil using avhrr and modis ndvi time series. Eur. J. Remote Sens 46, 40–59.

Schuster, C., Schmidt, T., Conrad, C., Kleinschmit, B., Förster, M., 2015. Grassland habitat mapping by intraannual time series analysis - comparison of rapideye and terrasar-x satellite data. International Journal of Applied Earth Observation and Geoinformation 34, 25–34.

Senf, C., Leitão, P.J., Pflugmacher, D., van der Linden, S., Hostert, P., 2015. Mapping land cover in complex mediterranean landscapes using landsat: Improved classification accuracies from integrating multi-seasonal and synthetic imagery. Remote Sensing of Environment 156, 527–536.

Sims, D.A., Gamon, J.A., 2002. Relationships between leaf pigment content and spectral reflectance across a wide range of species, leaf structures and developmental stages. Remote Sens. Environ. 81, 337–354.

Skidmore, A., 2003. Environmental modelling with GIS and remote sensing. CRC Press.

Song, C., Dickinson, M.B., Su, L., Zhang, S., Yaussey, D., 2010. Estimating average tree crown size using spatial in-

formation from Ikonos and QuickBird images: Across-sensor and across-site comparisons. Remote Sens. Environ. 114, 1099–1107.

Spurr, S.H., et al., 1960. Photogrammetry and photo-interpretation. with a section on applications to forestry. Photogrammetry and photo-interpretation. With a section on applications to forestry. .

Stehman, S.V., 1997. Selecting and interpreting measures of thematic classification accuracy. Remote sensing of Environment 62, 77–89.

Stoll, E., Konstanski, H., Anderson, C., Douglass, K., Oxfort, M., 2012. The RapidEye constellation and its data products, in: 2012 IEEE Aerospace Conference, IEEE. Institute of Electrical & Electronics Engineers (IEEE). pp. 1–9.

Sun, Z., Chang, N.B., Opp, C., Hennig, T., 2011. Evaluation of ecological restoration through vegetation patterns in the lower tarim river, china with modis ndvi data. Ecological Informatics 6, 156–163.

Tao, H., Gemmer, M., Song, Y., Jiang, T., 2008. Ecohydrological responses on water diversion in the lower reaches of the tarim river, china. Water resources research 44.

Tewes, A., Thonfeld, F., Schmidt, M., Oomen, R.J., Zhu, X., Dubovyk, O., Menz, G., Schellberg, J., 2015. Using rapideye and modis data fusion to monitor vegetation dynamics in semiarid rangelands in south africa. Remote Sensing 7, 6510–6534.

Thevs, N., 2005. Tugay vegetation in the middle reaches of the tarim river-vegetation types and their ecology. Archives of Nature Conservation and Landscape Research 44, 63–84.

Thevs, N., 2007. Ecology, spatial distribution, and utilization of the Tugai Vegeta-

tion at the middle reaches of the Tarim river, Xinjiang, China. Cuvillier Verlag.

Thevs, N., Buras, A., Zerbe, S., Kühnel, E., Abdusalih, N., Ovezberdiyeva, A., 2012. Structure and wood biomass of near-natural floodplain forests along the Central Asian rivers Tarim and Amu Darya. Forestry 85, 193–202.

Thevs, N., Zerbe, S., Schnittler, M., Abdusalih, N., Succow, M., 2008. Structure, reproduction and flood-induced dynamics of riparian tugai forests at the tarim river in xinjiang, nw china. Forestry 81, 45–57.

Thomas, F.M., Foetzki, A., Arndt, S.K., Bruelheide, H., Gries, D., Li, X., Zeng, F., Zhang, X., Runge, M., 2006. Water use by perennial plants in the transition zone between river oasis and desert in nw china. Basic and Applied Ecology 7, 253–267.

Thomas, F.M., Jeschke, M., Zhang, X., Lang, P., 2016. Stand structure and productivity of populus euphratica along a gradient of groundwater distances at the tarim river (nw china). Journal of Plant Ecology , rtw078.

Thomas, S.J., Deschamps, A., Landry, R., van der Sanden, J.J., Hall, R.J., 2007. Mapping insect defoliation using multi-temporal landsat data, in: Proc CRSS/ASPRS 2007 In Conf. on "Our Common Borders-Safety, Security, and the Environment through Remote Sensing", Ottawa (Canada). October.

Tian, F., Wang, Y., Fensholt, R., Wang, K., Zhang, L., Huang, Y., 2013. Mapping and evaluation of NDVI trends from synthetic time series obtained by blending landsat and MODIS data around a coalfield on the loess plateau. Remote Sensing 5, 4255–4279.

Tiede, D., Lang, S., Hoffmann, C., 2008. Domain-specific class modelling for one-level representation of single trees, in: Object-Based Image Analysis. Springer, pp. 133–151.

Tillack, A., Clasen, A., Kleinschmit, B., Förster, M., 2014. Estimation of the seasonal leaf area index in an alluvial forest using high-resolution satellite-based vegetation indices. Remote Sensing of Environment 141, 52–63.

Townsend, P.A., Eshleman, K.N., Welcker, C., 2004. Remote sensing of gypsy moth defoliation to assess variations in stream nitrogen concentrations. Ecological Applications 14, 504–516.

Townshend, J.R., Justice, C.O., 1988. Selecting the spatial resolution of satellite sensors required for global monitoring of land transformations. International Journal of Remote Sensing 9, 187–236.

Treuhaft, R.N., Law, B.E., Asner, G.P., 2004. Forest attributes from radar interferometric structure and its fusion with optical remote sensing. BioScience 54, 561–571.

Tropek, R., Sedláček, O., Beck, J., Keil, P., Musilová, Z., Šímová, I., Storch, D., 2014. Comment on 'high-resolution global maps of 21st-century forest cover change'. Science 344, 981–981.

Tucker, C.J., 1979. Red and photographic infrared linear combinations for monitoring vegetation. Remote sensing of Environment 8, 127–150.

Turner, M.G., 2010. Disturbance and landscape dynamics in a changing world. Ecology 91, 2833–2849.

UNCED, 1992. Agenda 21. united nations conference on environment and development., United Nations, New York.

Updike, T., Comp, C., 2010. Radiometric Use of WorldView-2 Imagery. Technical Note 1.0. DigitalGlobe.

Vanclay, J.K., 1995. Synthesis: Growth models for tropical forests: A synthesis of models and methods. Forest Science 41, 7–42.

Verbesselt, J., Hyndman, R., Newnham, G., Culvenor, D., 2010a. Detecting trend and seasonal changes in satellite image time series. Remote sensing of Environment 114, 106–115.

Verbesselt, J., Hyndman, R., Zeileis, A., Culvenor, D., 2010b. Phenological change detection while accounting for abrupt and gradual trends in satellite image time series. Remote Sensing of Environment 114, 2970–2980.

Verbesselt, J., Zeileis, A., Herold, M., 2012. Near real-time disturbance detection using satellite image time series: Drought detection in somalia. Remote Sens. Environ 123.

Walker, J., de Beurs, K., Wynne, R., 2014. Dryland vegetation phenology across an elevation gradient in arizona, usa, investigated with fused modis and landsat data. Remote Sensing of Environment 144, 85–97.

Walker, J., De Beurs, K., Wynne, R., Gao, F., 2012. Evaluation of landsat and modis data fusion products for analysis of dryland forest phenology. Remote Sensing of Environment 117, 381–393.

Wallner, A., Elatawneh, A., Schneider, T., Knoke, T., 2015. Estimation of forest structural information using rapideye satellite data. Forestry 88, 96–107.

Wang, L., Gong, P., Biging, G.S., 2004. Individual Tree-Crown Delineation and Treetop Detection in High-Spatial-Resolution Aerial Imagery. Photogrammetric Engineering & Remote Sensing 70, 351–358.

Wang, Q., Ruan, X., Chen, Y., Li, W., 2007. Eco-physiological response of populus euphratica oliv. to water release of the lower reaches of the tarim river, china. Environmental geology 53, 349–357.

Wang, T., Yan, C., Song, X., Xie, J., 2012. Monitoring recent trends in the area of aeolian desertified land using Landsat images in China Xinjiang region. ISPRS journal of photogrammetry and remote sensing 68, 184–190.

Watts, L., Laffan, S., 2013. Sensitivity of the bfast algorithm to modis satellite and vegetation index, in: 20th International congress on modelling and simulation. Modelling and Simulation Society of Australia and New Zealand Inc., Adelaide, pp. 1638–1644.

Watts, L.M., Laffan, S.W., 2014. Effectiveness of the bfast algorithm for detecting vegetation response patterns in a semi-arid region. Remote Sensing of Environment 154, 234–245.

Weichelt, H., Rosso, P., Marx, A., Reigber, S., Douglass, K., Heynen, M., 2012. The rapideye red edge band. Technical Report. Technical report, BlackBridge.

Weisgerber, H., 1994. Populus euphratica. Enzyklopädie der Holzgewächse: Handbuch und Atlas der Dendrologie. Ecomed, Landsberg am Lech 22, 39–41.

Wen, L., Saintilan, N., 2015. Climate phase drives canopy condition in a large semi-arid floodplain forest. Journal of Environmental Management .

Westermann, J., Zerbe, S., Eckstein, D., 2008. Age structure and growth of degraded populus euphratica floodplain forests in north-west china and perspectives for their recovery. Journal of Integrative Plant Biology 50, 536–546.

Whiteside, T., Ahmadb, W., 2008. Estimating canopy cover from eucalypt dominant tropical savanna using the extraction of tree crowns from very high resolution imagery. Proceedings of GEO-BIA 2008–Pixels, Objects, Intelligence: GEOgraphic Object-Based Image Analysis for the 21st Century .

Wiehle, M., Eusemann, P., Thevs, N., Schnittler, M., 2009. Root suckering patterns in populus euphratica (eu-

phrates poplar, salicaceae). Trees 23, 991–1001.

Williams, A.P., Allen, C.D., Millar, C.I., Swetnam, T.W., Michaelsen, J., Still, C.J., Leavitt, S.W., 2010. Forest responses to increasing aridity and warmth in the southwestern united states. Proceedings of the National Academy of Sciences 107, 21289–21294.

Wilson, A.M., Jetz, W., 2016. Remotely sensed high-resolution global cloud dynamics for predicting ecosystem and biodiversity distributions. PLoS Biol 14, e1002415.

Woodcock, C.E., Allen, R., Anderson, M., Belward, A., Bindschadler, R., Cohen, W., Gao, F., Goward, S.N., Helder, D., Helmer, E., et al., 2008. Free access to landsat imagery. Science (New York, NY) 320, 1011.

Woodcock, C.E., Strahler, A.H., 1987. The factor of scale in remote sensing. Remote sensing of Environment 21, 311–332.

World Resources Institute, 2016. Global Forest Watch. URL: http://www.globalforestwatch.org.

Wu, X.q., Cai, Y.l., 2004. Land cover changes and landscape dynamics assessment in lower reaches of tarim river in china. Chinese Geographical Science 14, 28–33.

Wulder, M., Niemann, K.O., Goodenough, D.G., 2000. Local Maximum Filtering for the Extraction of Tree Locations and Basal Area from High Spatial Resolution Imagery. Remote Sens. Environ. 73, 103–114.

Wulder, M.A., Coops, N.C., 2014. Satellites: Make earth observations open access. Nature 513, 30–31.

Wulder, M.A., Masek, J.G., Cohen, W.B., Loveland, T.R., Woodcock, C.E., 2012. Opening the archive: How free data has enabled the science and monitoring promise of landsat. Remote Sensing of Environment 122, 2–10.

Wulder, M.A., White, J.C., Goward, S.N., Masek, J.G., Irons, J.R., Herold, M., Cohen, W.B., Loveland, T.R., Woodcock, C.E., 2008. Landsat continuity: Issues and opportunities for land cover monitoring. Remote Sensing of Environment 112, 955–969.

Wulder, M.A., White, J.C., Niemann, K.O., Nelson, T., 2004. Comparison of airborne and satellite high spatial resolution data for the identification of individual trees with local maxima filtering. Int. J. Remote Sens. 25, 2225–2232.

Xin, Q., Olofsson, P., Zhu, Z., Tan, B., Woodcock, C.E., 2013. Toward near real-time monitoring of forest disturbance by fusion of modis and landsat data. Remote Sensing of Environment 135, 234–247.

Xu, H., Li, Y., 2006. Water-use strategy of three central asian desert shrubs and their responses to rain pulse events. Plant and Soil 285, 5–17.

Xu, H., Ye, M., Song, Y., Chen, Y., 2007. The natural vegetation responses to the groundwater change resulting from ecological water conveyances to the lower tarim river. Environmental Monitoring and Assessment 131, 37–48.

Xu, Z., Chen, Y., Li, J., 2004. Impact of climate change on water resources in the tarim river basin. Water Resources Management 18, 439–458.

Yan, H., Zhan, J., Zhang, T., 2011. Resilience of forest ecosystems and its influencing factors. Procedia Environmental Sciences 10, 2201–2206.

Yang, X., Zhang, K., Jia, B., Ci, L., 2005. Desertification assessment in china: An overview. Journal of Arid Environments 63, 517–531.

Yaning, C., Changchun, X., Xingming, H., Weihong, L., Yapeng, C., Chenggang, Z., Zhaoxia, Y., 2009. Fifty-year climate change and its effect on annual runoff in the tarim river basin, china. Quaternary International 208, 53–61.

Yu, P., Xu, H., Ye, M., Liu, S., Gong, J., An, H., Fu, J., 2012. Effects of ecological water conveyance on the ring increments of populus euphratica in the lower reaches of tarim river. Journal of forest research 17, 413–420.

Zeleke, G., Hurni, H., 2001. Implications of land use and land cover dynamics for mountain resource degradation in the northwestern ethiopian highlands. Mountain research and development 21, 184–191.

Zerbe, S., Thevs, N., 2011. Restoring central asian floodplain ecosystems as natural capital and cultural heritage in a continental desert environment, in: Landscape Ecology in Asian Cultures. Springer, pp. 277–297.

Zhandong, S., Opp, C., Run, W., 2009. Vegetation response to Ecological Water Diversion in the lower Tarim River, Xinjiang, China. Basic and Applied Dryland Research 3, 1–16. ISSN 1864-3191.

Zhang, J., Wu, G., Wang, Q., Li, X., 2010. Restoring environmental flows and improving riparian ecosystem of tarim river. Journal of Arid Land 2, 43–50.

Zhang, Y., Chen, Y., Pan, B., 2005. Distribution and floristics of desert plant communities in the lower reaches of tarim river, southern xinjiang, people's republic of china. Journal of Arid Environments 63, 772–784.

Zhang, Y., Chen, Y., Zhang, X., 2004. Plant communities and their interrelations with environmental factors in the lower reaches of tarim river [j]. Acta Geographica Sinica 6, 012.

Zhao, R., Chen, Y., Shi, P., Zhang, L., Pan, J., Zhao, H., 2013. Land use and land cover change and driving mechanism in the arid inland river basin: a case study of tarim river, xinjiang, china. Environmental Earth Sciences 68, 591–604.

Zhao, Z., Wang, R., Sun, H., Zhang, H., 2006. Assessment of water-recharging based on ecological features of riparian forest in the lower reaches of tarim river. Chinese Science Bulletin 51, 37–42.

Zheng, D., Li, W.h., Dong, T.z., Zhang, H.f., 2004. Impact of embankment on groundwater depth in middle reaches of tarim river. Journal of Desert Research 24, 745–750.

Zhou, J., Proisy, C., Descombes, X., Le Maire, G., Nouvellon, Y., Stape, J.L., Viennois, G., Zerubia, J., Couteron, P., 2012. Mapping local density of young *Eucalyptus* plantations by individual tree detection in high spatial resolution satellite images. Forest Ecology and Management .

Zhou, W., Yang, X., Hao, P., Liu, Q., Cao, D., Baribault, T., Li, J., 2010. Plant diversity and its maintenance in *Populus euphratica* riparian forests in the Ejina Oasis, China. Forestry Studies in China 12, 55–61.

Zhu, X., Chen, J., Gao, F., Chen, X., Masek, J.G., 2010. An enhanced spatial and temporal adaptive reflectance fusion model for complex heterogeneous regions. Remote Sensing of Environment 114, 2610–2623.

Zhu, X., Wu, L., Obul, O., Habibulla, Ä., 2006. The regulation of the tarim river system. Watershed and floodplain management along the Tarim River in China's arid northwest. Shaker, Aachen .

Zhu, Z., Woodcock, C.E., 2012. Object-based cloud and cloud shadow detection in landsat imagery. Remote Sensing of Environment 118, 83–94.

Zhu, Z., Woodcock, C.E., 2014. Continuous change detection and classification of land cover using all available landsat data. Remote sensing of Environment 144, 152–171.

Index

Publications related to the doctoral thesis

Peer reviewed articles

1. Niu, T., Kurban, A., Halik, U., **Gärtner, P.**, Kleinschmit, B., Ablekim, A., ... & LIU, G. L. (2012). Characteristics of Populus euphratica leaf water and chlorophyll contents in an arid area of Xinjiang, Northwest China. Chinese Journal of Ecology, 6, 006. (in chinese)

2. Liu, G. L., Kurban, A., Halik, U., Duan, H. M., **Gärtner, P.**, Kleinschmit, B., ... & Niu, T. (2012). Analysis of vegetation landscape pattern dynamics based on trajectory change detection. Journal of Desert Research, 32, 1472-1478.

3. **Gärtner, P.**, Förster, M., Halik, Ü., Kurban, A. , Kleinschmit, B. (2014). How can form, textural and spectral parameters determine the degradation status of *Populus euphratica* trees? South Eastern European Journal of Earth Observation and Geomatics, 3, 99-102.

4. **Gärtner, P.**, Förster, M., Kurban, A., & Kleinschmit, B. (2014). Object based change detection of Central Asian Tugai vegetation with very high spatial resolution satellite imagery. International Journal of Applied Earth Observation and Geoinformation, 31, 110-121.

5. Rumbaur, C., Thevs, N., Disse, M., Ahlheim, M., Brieden, A., Cyffka, B., Duethmann, D., Feike, T., Frör, O., **Gärtner, P.** & Halik, Ü. et.al (2015). Sustainable management of river oases along the Tarim River (SuMaRiO) in Northwest China under conditions of climate change. Earth System Dynamics, 6(1), 83.

6. **Gärtner, P.**, Förster, M., & Kleinschmit, B. (2016). The benefit of synthetically generated RapidEye and Landsat 8 data fusion time series for riparian forest disturbance monitoring. Remote Sensing of Environment, 177, 237-247.

International conference presentations (oral & poster)

1. **Gärtner, P.**, Suchenwirth, L., Kurban, A., Kleinschmit, B., (2012, May). Object based change detection of degraded Populus euphratica floodplain forest at the lower reaches of the Tarim river, China. GeoBia 2012, Rio de Janeiro, Brazil.

2. **Gärtner, P.**, Förster, M., Halik, Ü., Kurban, A. , Kleinschmit, B. (2014, March). How can form, textural and spectral parameters determine the degradation status of *Populus euphratica* trees? 5th workshop of the EARSeL Special Interest Group on Land Use and Land Cover. Berlin, Germany.

3. **Gärtner, P.**, Förster, M.,, Schmidt, T., Kurban, A., Kleinschmit, B., (2014, Nov.). Monitoring dynamics of semi-arid riparian Tugai forests at the Tarim River with RapidEye and Landsat data fusion products. ForestSAT2014, Riva del Garda, Italy.

4. **Gärtner, P.**, & Kleinschmit, B. (2015, July). Monitoring forest recovery with change metrics derived from Landsat time series stacks. In Analysis of Multitemporal Remote Sensing Images (Multi-Temp), IEEE. Annecy, France.

5. **Gärtner, P.**, Förster, M., & Kleinschmit, B. (2016, May). After the Browning: Assessment of Long Term Greening Trends in a Dryland Area

of Central Asia Landsat Time Series Analysis with Google Earth Engine. ESA Living Planet Symposium 2016, Prague, Czech Republic

6. Förster, M. and **Gärtner, P.** (2016, June). Methods for bridging spatial & temporal limitations of satellite data to monitor forest disturbances. GEO BON Open Science Conference 2016, Leipzig, Germany.

Map of Acknowledgements